DANIELA RODRIGUES SILVA

CONFORMATION AND BONDING:

THEORETICAL STUDIES ON CONFORMATIONAL EFFECTS AND LEWIS PAIR STABILITY

LAVRAS – MG | AMSTERDAM – NL

2021

DANIELA RODRIGUES SILVA

CONFORMATION AND BONDING: THEORETICAL STUDIES ON CONFORMATIONAL EFFECTS AND LEWIS PAIR STABILITY

Tese apresentada à Universidade Federal de Lavras, como parte das exigências do Programa de Pós-Graduação em Agroquímica, área de concentração em Química/Bioquímica, para a obtenção do título de Doutor, e em conformidade com o acordo acadêmico internacional para diploma duplo de doutorado firmado com a Vrije Universiteit Amsterdam.

Prof. Dr. Matheus Puggina de Freitas
Prof. Dr. Célia Fonseca Guerra
Orientadores

Dr. Trevor A. Hamlin
Coorientador

LAVRAS – MG | AMSTERDAM – NL

2021

Ficha catalográfica elaborada pelo Sistema de Geração de Ficha Catalográfica da Biblioteca Universitária da UFLA, com dados informados pelo(a) próprio(a) autor(a).

Rodrigues Silva, Daniela.
Conformation and Bonding: Theoretical Studies on Conformational Effects and Lewis Pair Stability / Daniela Rodrigues Silva. - 2021.
139 p.

Orientador(a): Matheus Puggina de Freitas.
Coorientador(a): Célia Fonseca Guerra, Trevor Alexander Hamlin.
Tese (doutorado) - Universidade Federal de Lavras, 2021.
Bibliografia.

1. Análise conformacional. 2. Pares de Lewis. 3. Teoria do funcional de densidade. I. de Freitas, Matheus Puggina. II. Fonseca Guerra, Célia. III. Hamlin, Trevor Alexander.

DANIELA RODRIGUES SILVA

CONFORMATION AND BONDING: THEORETICAL STUDIES ON CONFORMATIONAL EFFECTS AND LEWIS PAIR STABILITY

CONFORMAÇÃO E LIGAÇÃO: ESTUDOS TEÓRICOS SOBRE EFEITOS CONFORMACIONAIS E ESTABILIDADE DE PARES DE LEWIS

Tese apresentada à Universidade Federal de Lavras, como parte das exigências do Programa de Pós-Graduação em Agroquímica, área de concentração em Química/Bioquímica, para a obtenção do título de Doutor, e em conformidade com o acordo acadêmico internacional para diploma duplo de doutorado firmado com a Vrije Universiteit Amsterdam.

APROVADA em 22 de novembro de 2021

Prof. Dr.	Tom N. Grossmann	VUA
Dr.	Daan P. Geerke	VUA
Prof. Dr.	Jordi Poater	UB
Prof. Dr.	Halina Szatylowicz	WUT
Prof. Dr.	Teodorico de Castro Ramalho	UFLA

Prof. Dr. Matheus Puggina de Freitas
Prof. Dr. Célia Fonseca Guerra
Orientadores

Dr. Trevor A. Hamlin
Coorientador

LAVRAS – MG | AMSTERDAM – NL

2021

This work has been financially supported by the Conselho Nacional de Desenvolvimento Científico e Tecnológico (CNPq, grant number 140955/2017-8), the Coordenação de Aperfeiçoamento de Pessoal de Nível Superior (CAPES, grant number 88881.190436/2018-01), the Fundação de Amparo à Pesquisa do Estado de Minas Gerais (FAPEMIG), and the Netherlands Organization for Scientific Research (NWO).

Conformation and Bonding
Theoretical Studies on Conformational Effects and Lewis Pair Stability
Daniela Rodrigues Silva
2021

VRIJE UNIVERSITEIT

Conformation and Bonding

Theoretical Studies on Conformational Effects and Lewis Pair Stability

ACADEMISCH PROEFSCHRIFT

ter verkrijging van de graad Doctor of Philosophy
aan de Vrije Universiteit Amsterdam en
Universidade Federal de Lavras,
op gezag van de rectores magnifici
prof.dr. C.M. van Praag
en prof.dr. J.C. Resende Júnior,
in het openbaar te verdedigen
ten overstaan van de promotiecommissie
van de Faculteit der Bètawetenschappen
op maandag 22 november 2021 om 15.45 uur
in een bijeenkomst van de universiteit,
De Boelelaan 1105

door

Daniela Rodrigues Silva

geboren te Lavras, Brazilië

promotoren:	prof.dr. C. Fonseca Guerra
	prof.dr. M.P. Freitas
copromotor:	dr. T.A. Hamlin
promotiecommissie:	prof.dr. T.N. Grossmann
	dr. D.P. Geerke
	prof.dr. J. Poater
	prof.dr. H. Szatylowicz
	prof.dr. T.C. Ramalho

à minha família

RESUMO

Esta tese consiste em uma coleção de estudos usando a teoria do funcional de densidade em efeitos conformacionais e mecanismo de ligação de sistemas modelo halogenados. Em primeiro lugar, análises detalhadas das forças físicas subjacentes ao efeito *gauche* e a barreira rotacional de etanos 1,2-dissubstituídos são realizadas. Em seguida, as tendências de força de ligação de pares doadores–aceptores de Lewis arquetípicos são sistematicamente avaliadas. O principal objetivo é obter fundamentação física relevante para explicar os fenômenos químicos estudados. As análises detalhadas apresentadas apontam efeitos quânticos frequentemente negligenciados por trás das preferências conformacionais e forças de ligação observadas. Espera-se que os conhecimentos fundamentais obtidos nesta tese constituam um passo importante para o melhor entendimento do efeito de átomos de halogênio na estrutura e ligação de compostos orgânicos e inorgânicos, o qual poderia ser estendido para racionalizar, predizer e aperfeiçoar as propriedades de sistemas moleculares mais complexos.

Palavras-chave: Teoria de ligação. Análise conformacional. Teoria do funcional de densidade. Halogênios. Pares de Lewis.

ABSTRACT

This thesis consists of a collection of density functional theory investigations on conformational effects and bonding mechanism in halogenated model systems. First, thorough analyses of the physical forces underlying the *gauche* effect and the rotational barriers of 1,2-disubstituted ethanes have been performed. Then, the trends in bond strength of archetypal donor–acceptor Lewis pairs have been systematically evaluated. The main purpose is to obtain physically meaningful rationales to explain the studied chemical phenomena. The detailed analyses presented herein shed light on often overlooked quantum chemical effects behind the observed conformational preferences and bonding strengths. It is expected that the fundamental insights provided in this thesis will be a step towards a more comprehensive understanding of the effect of halogen atoms on the structure and bonding of organic and inorganic compounds, which could be extended to rationalize, predict, and tune the properties of more complex molecular systems.

Keywords: Bond theory. Conformational analysis. Density Functional Theory. Halogens. Lewis pairs.

TABLE OF CONTENTS

FIRST SECTION

1 GENERAL INTRODUCTION

Chemistry is all about molecules. The pursuit for a robust understanding of how molecules orient themselves in space and combine to form larger aggregates is a quintessential aspect of the chemical sciences. Chemists often make use of archetypal molecular systems to investigate a given phenomenon of interest. The model system is judiciously selected to perfectly address one specific question at a time. It is envisaged that the knowledge obtained from these simple systems can form a valuable toolbox useful for a more efficient design of new chemistries towards specific molecular properties. Theoretical chemistry has significantly assisted in this regard. As computational methods have continuously evolved over the years, one can now interrogate the electronic structure of increasingly larger systems with good accuracy and quantitatively explain complex concepts, once described only based on chemical intuition. This thesis represents a key step, embedded in the broader context of theoretical investigations, towards truly understanding and rationalizing the structure and bonding of (in)organic compounds. It is expected that the findings disclosed herein will furnish a unique perspective and shed light on novel physical factors, which combined with other rationalizations in the literature, will be a step forward to a better understanding of conformational effects and chemical bonding.

The primary goal of this thesis is to contribute to (and hopefully end) the ongoing debate about the factors governing the structure and bonding of (in)organic compounds using state-of-the-art density functional theory. The monovalent and unique electronic characteristics of group 17 in the periodic table render halogenated compounds an appealing model system for the task. Thus, we explore the effect of halogen atoms on the conformational preferences of standard organic scaffolds as well as on the bonding mechanism of archetypal Lewis pairs. The insights gained from these investigations enabled us to unravel a set of causal relationships, which are, at the same time, rooted in accurate quantum mechanics and chemically intuitive. The thesis has been, therefore, divided into two main sections: i) Section A, which describes the main goals (Chapter 1) and important concepts (Chapter 2) that lay the foundation for the scientific works developed in the following chapters, and ii) Section B, which contains the density

functional theory investigations into conformational isomerism (Chapters 3–5) and bonding mechanism (Chapter 6).

2 THEORETICAL BACKGROUND

This chapter describes the theoretical background of the thesis, which has been organized as follows. First, key definitions and important aspects of conformational analysis studies (Sections 2.1 and 2.2) and Lewis acid/base chemistry (Section 2.3) are introduced. This is followed by a basic introduction on the fundamentals of the density functional theory and related electronic structure analyses (Sections 2.4 and 2.5), which form the core methodology employed throughout this thesis. The purpose is to provide the reader with a brief overview of prominent literature and general conceptual background. Finally, the research idea underlying the thesis is presented (Section 2.6).

2.1 Conformational Isomerism

Molecules are dynamic entities. An organic compound can acquire several structural arrangements with the same constitution (*i.e.*, the same atoms and the same connectivity between them) but different three-dimensional orientation in space simply through rotation around single bonds. These are called conformations. Although the number of prospective conformations exponentially increases with the number of rotatable bonds, only a few of them are energetically favored. At room temperature, these low-energy conformers are usually in constant equilibrium (*i.e.*, conformational isomerism), they can easily interconvert from one to another. Thus, the overall three-dimensional structure of an organic molecule is an average over its conformers (CAREY; SUNDBERG, 2007; ELIEL; WILEN, 1994).

The preferential conformation adopted by a given molecule directly correlates to its observed properties (BARTON, 1972; HOFFMANN, 2000). It can, for example, affect the binding of a drug or agrochemical to its biological target (YANG et al., 2020) as well as the stereoselectivity towards a specific reaction mechanism (PATTISON, 2017). Strategies aiming at controlling conformational preferences have been used to rationally tune desirable properties in the design of new chemistries, such as, to preorganize the structure of a lead compound to resemble its bioactive conformation (APPAVOO et al., 2019; ZHENG; TICE; SINGH, 2017), to increase the rates of a reaction (BLANKENSTEIN; ZHU, 2005; CHEN et al., 2020), or to

design more selective catalysts (AUFIERO; GILMOUR, 2018). However, to more efficiently control the molecular structure and, therefore, the associated physical, chemical, or biological properties, it is essential to understand why a given conformer is more stable than another in the first place.

The quest to better understand and rationalize the driving forces behind conformational preferences has been intriguing organic chemists for decades. As an example, let us take ethane, the simplest molecule that exhibits conformational isomerism (ELIEL; WILEN, 1994). The rotation around the C–C bond of ethane, that is, the variation of one $\varphi_{H–C–C–H}$ dihedral angle from 0° to 180°, leads to the energy profile illustrated in Figure 2.1a. It shows two equivalent, staggered energy minima connected via two equivalent, eclipsed energy maxima. The energy barrier for rotation around the C–C bond of ethane is small, *ca* 3.0 kcal mol^{-1}, as a result, the interconversion of one conformer into the other proceeds quite fast at room temperature (CAREY; SUNDBERG, 2007; PITZER, 1983). Although experimental evidence on the rotational barrier of ethane dates from almost a century ago (KEMP; PITZER, 1936), only several years later considerable progress was made on elucidating the physical factors underlying its conformational stability (BICKELHAUPT; BAEREND, 2003; MO et al., 2004a; MO; GAO, 2007; POPHRISTIC; GOODMAN, 2001; SCHREINER, 2002; SONG et al., 2005; WEINHOLD, 2001, 2003). This can be ascribed to the notable development of the field of theoretical chemistry during this period. The continual advancement of computational power combined with the refinement of mathematical descriptions has enabled chemists to interrogate the electronic structure of increasingly larger systems in great detail and satisfactory accuracy. Modern theoretical chemistry, also referred to as computational chemistry, has provided chemists with the tools, rooted in quantum mechanical principles, necessary to obtain insight into chemical problems (SCHWARZ; SCHMIDBAUR, 2012). In the case of the rotation barrier of ethane, quantum chemical investigations have supported the classical explanation based on the repulsion between vicinal C–H bonds (*i.e.*, steric repulsion) in destabilizing the eclipsed form (BICKELHAUPT; BAEREND, 2003; MO et al., 2004a; MO; GAO, 2007), as well as have introduced the idea of occupied–unoccupied orbital interactions between antiperiplanar C–H bonds (*i.e.*, hyperconjugation) in stabilizing the staggered form (POPHRISTIC; GOODMAN, 2001; SCHREINER, 2002; SONG et al., 2005; WEINHOLD, 2001, 2003), see Figure 2.1b.

Figure 2.1 – a) Stationary points in the energy profile for rotation around the C–C bond of ethane, and b) the main interactions giving rise to the rotational barriers; c) stationary points in the energy profile for rotation around the C–C bond of 1,2-dihaloethanes, and b) the main interactions affecting the *gauche-anti* equilibrium.

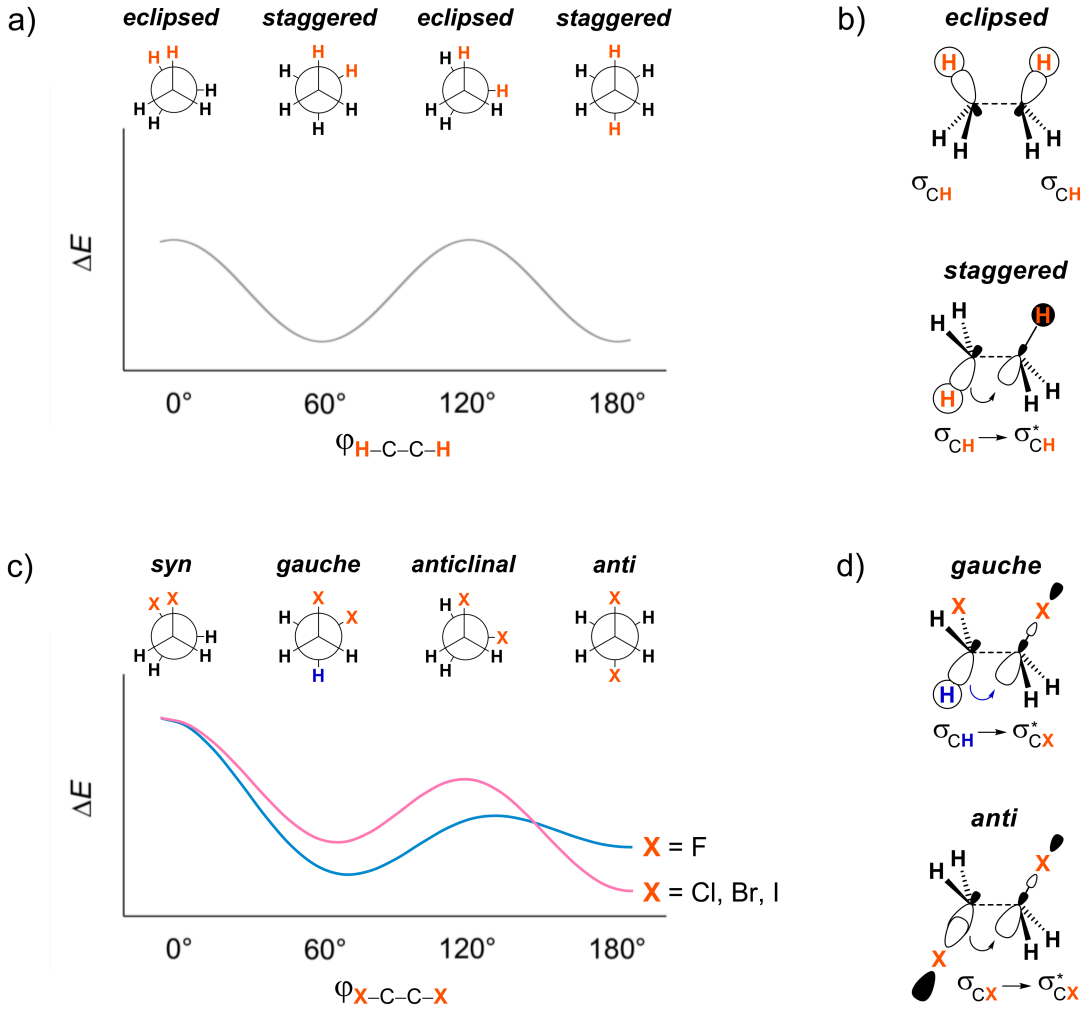

Source: From the author

To obtain quantum chemical insights into the forces governing conformational preferences, the interaction between fragments (*e.g.*, atoms, bonds, or groups) is usually decomposed into different energy components, such as steric repulsion and hyperconjugation mentioned above. This energy decomposition can be performed in many ways, which have been extensively described elsewhere (ANDRÉS et al., 2019; PASTORCZAK; CORMINBOEUF, 2017; PHIPPS et al., 2015). Herein, only the methods applied in this thesis are discussed in Sections 2.4 and 2.5.

2.2 The *Gauche* Effect

If one hydrogen atom on each carbon of ethane is replaced by a halogen atom, thus yielding the X–C–C–X motif (where X = F, Cl, Br, and I), the rotational energy profile changes as depicted in Figure 2.1c. The two staggered conformers (*i.e.*, *gauche* and *anti*) are no longer equivalent, their relative stability depends on the mutual orientation between the two halogen atoms. A similar effect is observed for the eclipsed forms (*i.e.*, *syn* and *anticlinal*). Chemical intuition would expect the *anti*-conformer to be the lowest in energy because it orientates the larger, electron-richer atoms farther removed from each other. That is, indeed, the case for X = Cl, Br, and I; but not for X = F (AKKERMAN et al., 2003; BUTCHER; COHEN; ROUNDS, 1971; TAKEO; MATSUMURA, 1986; VAN SCHAICK et al., 1973). 1,2-Difluoroethane is the classical example of the so-called *gauche* effect (THIEHOFF; REY; GILMOUR, 2017), a term coined by Wolfe (1972), which describes the counterintuitive preference of the *gauche* over the *anti*-conformer in cases X is an electron-withdrawing group (BUISSONNEAUD; VAN MOURIK; O'HAGAN, 2010).

The currently accepted model used to explain the *gauche* effect is based on hyperconjugative interactions between antiperiplanar σ bonds (BRUNCK; WEINHOLD, 1979; GOODMAN; GU; POPHRISTIC, 2005). It is argued that the C–F bond is a poor electron-donor and a good electron-acceptor because both filled σ_{CF} and empty σ^*_{CF} orbitals lie low in energy. The *gauche* conformer of 1,2-difluoroethane is, therefore, stabilized by the charge-transfer from the filled σ_{CH} orbital to the empty σ^*_{CF} orbital, which is stronger than the corresponding charge-transfer from the filled σ_{CF} orbital to the empty σ^*_{CF} orbital in the *anti*-conformer (ALABUGIN; GILMORE; PETERSON, 2011). Both electron-acceptor and electron-donor capabilities improve as the halogen atom is varied from F to I, favoring then the hyperconjugation $\sigma_{CX} \rightarrow \sigma^*_{CX}$ in the *anti*-orientation for heavier 1,2-dihaloethanes XCH_2CH_2X (where X = Cl, Br, and I) (NORI-SHARGH; BOGGS, 2011; SOUZA; FREITAS; RITTNER, 2008), see Figure 2.1d.

Due to the ubiquity of halogens, especially the fluorine atom, in modern agrochemicals (FUJIWARA; O'HAGAN, 2014; JESCHKE, 2010), pharmaceuticals (HERNANDES et al., 2010; MEI et al., 2019; MÜLLER; FAEH; DIEDERICH, 2007), and materials (BERGER et al., 2011; KARLICKÝ et al., 2013), the *gauche* effect has been widely applied as a conformational control tool to modulate desirable properties (THIEHOFF; REY; GILMOUR, 2017). The number of prospective applications includes but are not limited to drug design (GILLIS et al., 2015; MEANWELL, 2018), molecular recognition (BENTLER et al., 2019), and catalysis (MOLNÁR et al., 2013). The *gauche* effect is not restricted only to systems with

vicinal C–F bonds, it is also observed in a variety of 1,2-disubstituted ethane fragments. Along the X–C–C–Y motif, if X = F, the choice of Y that leads to a *gauche* preference is quite broad: Y = F, OH, OAc, NH_2, NHAc, SH, SOR, and SO_2R (ALABUGIN, 2016; ALEKSIĆ; STOJANOVIĆ; BARANAC-STOJANOVIĆ, 2015; HUNTER, 2010; THIEHOFF et al., 2016).

Although the hyperconjugation model has been widely used to rationalize the *gauche* preference, the origin of the *gauche* effect is still a subject of ongoing debate. Various alternative explanations have been proposed in the literature over the years, which advocate the role of other forces in either stabilizing the *gauche* conformer or destabilizing the *anti*-orientation (SENDEROWITZ; FUCHS, 1997; THIEHOFF; REY; GILMOUR, 2017). Wiberg and coworkers (1990) have attributed the *gauche* effect to a destabilization of the *anti*-conformer due to a poorer C–C bond orbital overlap caused by the bending of the H–C–F angle, the so-called bent bond model (WIBERG, 1996). However, Goodman, Gu, and Pophristic (2005), proponents of the hyperconjugation model, have shown that the change in orbital overlap along the C–C bond from *gauche* to *anti* is actually too small to account for their relative energy differences. More recently, Baranac-Stojanović (2014) has pointed out that the *gauche* conformer is stabilized by both hyperconjugation and attractive electrostatic interactions. Thacker and Popelier (2018), on the other hand, have explained the *gauche* preference solely based on electrostatics, more specifically the attractive 1,3 C•••F electrostatic polarization interaction. This rationalization has been further elaborated in the work of Díaz et al. (2019), in which they have shown that the C•••F attraction is counterbalanced by F•••F and C•••C repulsions and that the greater stability of the *gauche* conformer stems from exchange-correlation interactions. As the *gauche* effect (and other stereoelectronic effects) can be used to modulate the molecular structure towards specific properties, a thorough understanding of its underlying physical mechanism is therefore essential.

2.3 Lewis Acid–Base Chemistry

The same physical forces mentioned in the previous sections (*e.g.*, charge transfer, polarization, and electrostatic interactions) that affect the conformational preferences of organic compounds also underlie the bonding mechanism in Lewis acid–base pairs (MO; GAO, 2001). Lewis' (1923) definition of acids as electron-pair acceptors and bases as electron-pair donors pervades different areas of chemistry, ranging from metal complexes to archetypal organic reactions, to name a few (LEWIS, 1938; PEARSON, 2005). It comes as no surprise that Lewis acidity and

basicity concept is a mandatory teaching material in any introductory chemistry course and textbook (ATKINS; JONES; LAVERMAN, 2016; BROWN et al., 2003). Furthermore, the recent advent of frustrated Lewis pair (FLP) chemistry (STEPHAN; ERKER, 2010, 2015; STEPHAN, 2016) and further development of Lewis acid and base-catalyzed reactions (HAMLIN; FERNANDEZ; BICKELHAUPT, 2019; SVATUNEK et al., 2021; VERMEEREN et al., 2021) renewed the interest of the chemical community on main group chemistry and opened a new avenue for molecular and material synthesis (STAUBITZ et al., 2010; STEPHAN, 2015).

Lewis acids and Lewis bases combine to form adducts whose bond strength and length lie in between a chemical bond and a weak intermolecular interaction (LEOPOLD; CANAGARATNA; PHILLIPS, 1997). As the formation of these adducts involves the donation of an electron pair from the base to the acid (see Figure 2.2 for the formation of archetypal borane–ammonia adduct), they are often referred to as donor–acceptor complexes (MÉNDEZ; CEDILLO, 2013; MO et al., 2004b). Extensive research performed over the years has revealed, however, the more complex interplay of effects underpinning their bonding mechanism. The ability to engage in electrostatic (FRENKING et al., 2003; JONAS; FRENKING; REETZ, 1994) or polarization (MO; GAO, 2001) interactions, as well as the amount of energy required to deform the acid or base equilibrium geometries to the final adduct (*e.g.*, see the deformation of borane from a planar to a pyramidal geometry upon adduct formation in Figure 2.2) (ROWSELL; GILLESPIE; HEARD, 1999) are few examples of other factors that can affect the nature and/or the strength of the bonding in these systems. As the number of prospective applications in the field of Lewis acid–base chemistry has considerably expanded since its conception, an in-depth understanding of the factors governing the stability of Lewis pairs is crucial to more efficiently tune their properties.

Figure 2.2 – Formation of the donor–acceptor complex between borane and ammonia, $H_3B–NH_3$.

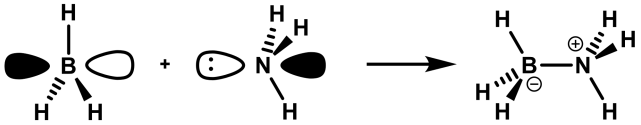

Source: From the author

2.4 Understanding Chemistry with DFT

Computational chemistry can provide insight into chemical reactions and transformations that are impossible to obtain through laboratory-based experiments alone (FORESMAN; FRISCH, 1996; JENSEN, 2006). Density functional theory (DFT) is the prevailing quantum mechanical method used to tackle problems in various branches of chemistry and physics (BECKE, 2014; BURKE, 2012). The remarkable gain in popularity of DFT since its formal foundation by the seminal works of Hohenberg and Kohn (1964) and Kohn and Sham (1965) is mainly due to its efficient computational cost/accuracy ratio. Different from wave-function methods, the fundamental premise of DFT states the energy E of a many-electron system is a functional of the electron density ρ: $E = E[\rho]$ (COHEN-TANNOUDJI; DIU; LALOË, 2005; KOCH; HOLTHAUSEN, 2001). This elegantly reduces the computational cost, as the N-electron wave-function Ψ has $4N$ degrees of freedom (*i.e.*, one spin coordinate and three spatial coordinates for *each* electron) while the electron (spin) density ρ has only four (JENSEN, 2006). However, the predictive power of DFT methods heavily relies on its exchange-correlation functional, which exact form is not known and needs to be approximated (COHEN; MORI-SÁNCHEZ; YANG, 2008; MEDVEDEV et al., 2017), leading to the different DFT approaches available (BECKE, 2014; KOCH; HOLTHAUSEN, 2001). The choice of the appropriate density functional depends on the chemical system under investigation and is usually selected by comparison with experimental data or with high-level quantum chemical calculations (MARDIROSSIAN; HEAD-GORDON, 2017).

DFT not only provides an accurate description of realistic systems but also enables one to understand and interpret the underlying physical mechanism in terms of molecular orbital (MO) theory (BICKELHAUPT; BAERENDS, 2000; HAMLIN et al., 2021). In this thesis, the DFT investigations are mainly performed in conjunction with the activation strain model (ASM) and the matching, canonical energy decomposition analysis (EDA), whose theoretical overview is provided in the following section.

2.5 Activation Strain and Energy Decomposition Analyses

The activation strain model (ASM) is a fragment-based approach to understand the energy profile of a chemical process in terms of interacting subunits (BICKELHAUPT; HOUK, 2017; VERMEEREN et al., 2020; WOLTERS; BICKELHAUPT, 2015). That comprises, for example, the formation of a transition state from the original reactants or of the ethane molecule

from two open-shell $CH_3^{\bullet}$ fragments. The fragmentation of the system depends on the research question and is critical to obtain meaningful results (BICKELHAUPT; BAERENDS, 2000). Thus, the bond energy ΔE is defined as follows:

$$\Delta E = E^{AB} - E^{A} - E^{B} \tag{2.1}$$

wherein E^{A}, E^{B}, and E^{AB} are, respectively, the energies of the fragments A and B and the molecular complex AB.

As A and B combine to form AB, the bonding mechanism can be divided into two steps: (i) the deformation of the fragments from their equilibrium structure to the geometry they acquire in the complex, and (ii) the actual chemical interactions that occur between the deformed fragments. The bond energy ΔE can, therefore, be decomposed into two major components, namely, the respective total strain and interaction energies, ΔE_{strain} and ΔE_{int}:

$$\Delta E = \Delta E_{strain} + \Delta E_{int} \tag{2.2}$$

The total strain ΔE_{strain} is an energy penalty related to the geometrical rigidity of the fragments. The ΔE_{strain} term can be further decomposed into the strain energies corresponding to the deformation of each fragment, $\Delta E_{strain,A}$ and $\Delta E_{strain,B}$:

$$\Delta E_{strain} = (E^{A \text{ in } AB} - E^{A}) + (E^{B \text{ in } AB} - E^{B}) \tag{2.3a}$$

$$\Delta E_{strain} = \Delta E_{strain,A} + \Delta E_{strain,B} \tag{2.3b}$$

wherein $E^{A \text{ in } AB}$ and $E^{B \text{ in } AB}$ correspond to the energy of A and B in the geometry adopted in AB, respectively.

On the other hand, the interaction energy ΔE_{int} is the actual energy change when the prepared fragments are combined to form the complex [Eq. (2.4a)]. The ΔE_{int} term can be further decomposed into physically meaningful energy components by applying an energy decomposition analysis (EDA) scheme. Herein, we combine the ASM with the matching, canonical EDA (BICKELHAUPT; BAERENDS, 2000; HAMLIN et al., 2021), which is based on the scheme of Morokuma (KITAURA; MOROKUMA, 1976; MOROKUMA, 1971) and the related extended transition state (ETS) method of Ziegler and Rauk (ZIEGLER; RAUK, 1977, 1979a, 1979b). The EDA decomposes the ΔE_{int} into four energy terms, namely, electrostatic

interactions ΔV_{elstat}, Pauli repulsion ΔE_{Pauli}, orbital interactions ΔE_{oi}, and dispersion energy ΔE_{disp}:

$$\Delta E_{\text{int}} = E^{\text{AB}} - E^{\text{A in AB}} - E^{\text{B in AB}} \tag{2.4a}$$

$$\Delta E_{\text{int}} = \Delta V_{\text{elstat}} + \Delta E_{\text{Pauli}} + \Delta E_{\text{oi}} + \Delta E_{\text{disp}} \tag{2.4b}$$

First, the ΔV_{elstat} term is obtained by bringing the unperturbed charge distributions of A and B from infinity to their positions in AB, resulting in a superposition of densities ρ_A and ρ_B. The associated energy change, ΔV_{elstat}, is the classical electrostatic interaction between the fragment charge distributions:

$$\Delta V_{\text{elstat}} = \sum_{\substack{\alpha \in A \\ \beta \in B}} \frac{Z_\alpha Z_\beta}{R_{\alpha\beta}} - \int \sum_{\alpha \in A} \frac{Z_\alpha \rho_B(r)}{|r - R_\alpha|} dr - \int \sum_{\beta \in B} \frac{Z_\beta \rho_A(r)}{|r - R_\beta|} dr + \int\int \frac{\rho_A(r_1)\rho_B(r_2)}{r_{12}} dr_1 dr_2 \tag{2.5}$$

The first and last terms in Eq. (2.5) correspond to the electrostatic repulsion between the nuclei and between electron densities of fragments A and B, respectively. The second and third terms are the electrostatic attraction between the nuclei of fragment A and the electron density of fragment B, and *vice versa*. The magnitude of the ΔV_{elstat} components in Eq. (2.5) increases as the fragment separation decrease and ρ_A and ρ_B start to overlap. The effect is, however, more pronounced for the attractive terms, resulting in a net stabilizing ΔV_{elstat} energy for neutral systems at equilibrium distances. In these cases, ΔV_{elstat} becomes repulsive only at very short distances due to the nuclear repulsion (FRENKING; BICKELHAUPT, 2014; KRAPP; BICKELHAUPT; FRENKING, 2006).

Then, the Pauli principle is enforced by the antisymmetrization ($\hat{A}$) and renormalization (N) of the product wave-function $\Psi^A\Psi^B$: $\Psi^0 = N\hat{A}[\Psi^A\Psi^B]$. The associated energy change going from $\Psi^A\Psi^B$ to Ψ^0 is the Pauli repulsion ΔE_{Pauli}, which comprises the two-center four-electron destabilizing interactions and is responsible for any steric repulsion. The magnitude of the ΔE_{Pauli} term is directly proportional to the overlap between closed-shell orbitals S on both fragments, that is, $\Delta E_{\text{Pauli}} \propto S^2$ (BICKELHAUPT et al., 1992; BICKELHAUPT; BAERENDS, 2000).

The system is finally allowed to relax to the final ground state energy of the interacting system Ψ^{AB}. The associated energy change, ΔE_{oi}, accounts for all empty-occupied orbital

interactions, namely, polarization (*i.e.*, empty-occupied orbital mixing on one fragment due to the presence of the other fragment), charge transfer (*i.e.*, donor−acceptor interactions between occupied orbitals on one fragment with empty orbitals on the other fragment), and, for open-shell fragments, electron-pair bonding (BICKELHAUPT; BAERENDS, 2000; HAMLIN et al., 2021). The magnitude of ΔE_{oi} depends on the energy difference between filled and empty orbitals $\Delta\varepsilon$ and the corresponding orbital overlap S, that is, $\Delta E_{oi} \propto S^2/\Delta\varepsilon$ (ALBRIGHT; BURDETT; WANGBO, 2013). Furthermore, the ΔE_{oi} term can be decomposed into the contributions from each irreducible representation Γ of the interacting system:

$$\Delta E_{oi} = \sum_{\Gamma} \Delta E_{\Gamma} \tag{2.6}$$

Finally, the dispersion energy ΔE_{disp} can also be analyzed if long-range dispersion corrections, such as Grimme's dispersion corrections (GRIMME et al., 2010; GRIMME; EHRLICH; GOERIGK, 2011), are explicitly added in the computations.

All the above-mentioned energy terms are highly dependent on the geometry and distance between the fragments. Thus, the ASM/EDA is usually performed by projecting the energy values into a relevant reaction coordinate ξ related to a critical geometrical change that occurs over the course of the chemical process of interest (VAN ZEIST et al., 2008) and the molecular orbital analysis is carried out at a consistent point in this energy profile (VERMEEREN et al., 2020).

2.6 Research Idea

In this thesis, the physical factors that govern the conformational preferences of small organic compounds (Chapter 3–5) and the stability of archetypal Lewis pairs (Chapter 6) are unraveled using DFT. The manifestation of the *gauche* effect in alicyclic systems is first explored in Chapter 3. As an alicyclic system, we select the 2-fluorocyclohexanone, a standard scaffold in organic chemistry and model system used in conformational analysis studies to explore intramolecular interactions. For comparison purposes, the heavier 2-chloro and 2-bromocyclohexanones are also investigated. The 2-halocyclohexanones undergo a well-defined conformational equilibrium in which the halogen atom can adopt either an axial or equatorial orientation. Selective introduction of endocyclic nitrogen groups, yielding the F–CH_2–CH_2–NR motif (where NR = *N*-Boc, $NCOOCH_3$, NCHO, NH, and NH_2^+), known to induce the *gauche*

effect in acyclic fragments, enable us to elucidate how these groups affect the axial-equatorial equilibrium of their alicyclic counterparts.

In Chapter 4, we delve deeper into the *gauche* effect, wherein we investigate its origin by comprehensive analysis of several rigid and flexible rotational energy profiles of the series of 1,2-dihaloethanes $XH_2C–CH_2X$ (where X = F, Cl, Br, and I). In contrast to the currently accepted rationale (Section 2.2), our analyses reveal that hyperconjugation favors the *gauche* conformer for all 1,2-dihaloethanes, not only for X = F. It is the interplay of more stabilizing hyperconjugation and reduced steric Pauli repulsion that gives rise to the *gauche* effect observed in the 1,2-difluoroethane.

Our analysis of rotational energy profiles is extended in Chapter 5 to investigate the conformational behavior of haloacetaldehydes $OHC–CH_2X$ (where X = F, Cl, Br, and I). In this case, we aim at investigating the ability of the widespread idea of dipolar repulsion between point charges to rationalize conformational energies. We show that the point charge picture breaks down as the halogen atom increases in size and becomes more diffuse because of a larger electrostatic attraction between electron densities and nuclei. Only for X = F, electrostatic interactions shift the conformational preference to *anti*. For heavier $OHC–CH_2X$ (where X = Cl, Br, and I), the overall rotational energy profile is again mainly set by a combined effect of steric Pauli repulsion and hyperconjugation.

In Chapter 6, we study the formation of the $X_3B–NY_3$ Lewis pairs (where X, Y = H, F, Cl, Br, and I) to untangle the nature and strength of Lewis acid/base interactions. First, we explore the archetypal borane–ammonia and, then, we evaluate the effect of halogen substituents on the Lewis acid and Lewis base to the strength of the forming B–N bond by separately varying X, Y from H to F, Cl, Br, and I. Detailed analysis of the electronic structure reveals the role of different energy components, such as the strain energy, besides the well-known electrostatics and charge transfer, in the stability of the Lewis pairs.

Finally, Chapter 7 summarizes the main findings and perspectives disclosed in the preceding chapters and is followed by the acknowledgments and the list of publications.

REFERENCES

AKKERMAN, F. et al. Crystal and molecular structure of 1,2-difluoroethane and 1,2-diiodoethane. **Journal of Chemical Crystallography**, New, York, v. 33, n. 12, p. 969–975, 2003.

ALABUGIN, I. V. **Stereoelectronic Effects: the Bridge between Structure and Reactivity**. Hoboken: John Wiley & Sons Ltd, 2016.

ALABUGIN, I. V.; GILMORE, K. M.; PETERSON, P. W. Hyperconjugation. **Wiley Interdisciplinary Reviews – Computational Molecular Science**, Hoboken, v. 1, n. 1, p. 109–141, 2011.

ALBRIGHT, T. A.; BURDETT, J. K.; WANGBO, W. H. **Orbital Interactions in Chemistry.** 2. ed. New York: Wiley, 2013.

ALEKSIĆ, J.; STOJANOVIĆ, M.; BARANAC-STOJANOVIĆ, M. Origin of Fluorine/Sulfur Gauche Effect of β-Fluorinated Thiol, Sulfoxide, Sulfone, and Thionium Ion. **The Journal of Organic Chemistry**, Washington, v. 80, n. 20, p. 10197–10207, 2015.

ANDRÉS, J. et al. Nine Questions on Energy Decomposition Analysis. **Journal of Computational Chemistry**, Hoboken, v. 40, n. 26, p. 2248–2283, 2019.

APPAVOO, S. D. et al. Conformational Control of Macrocycles by Remote Structural Modification. **Chemical Reviews**, Washington, v. 119, n. 17, p. 9724−9752, 2019.

ATKINS, P.; JONES, L.; LAVERMAN, L. **Chemical Principles: The Quest for Insight**. 7. ed. New York: W. H. Freeman and Company, 2016.

AUFIERO, M.; GILMOUR, R. Informing Molecular Design by Stereoelectronic Theory: The Fluorine Gauche Effect in Catalysis. **Accounts of Chemical Research**, Washington, v. 51, n. 7, p. 1701–1710, 2018.

BARANAC-STOJANOVIĆ, M. *Gauche* preference in 1,2-difluoroethane originates from both orbital and electrostatic stabilization interactions. **RSC Advances**, Cambridge, v. 4, n. 83, p. 43834–43838, 2014.

BARTON, D. H. R. The Principles of Conformational Analysis. **Nobel Lectures, Chemistry 1963–1970. Amsterdam: Elsevier Publishing Company**, 1972.

BECKE, A. D. Perspective: Fifty years of density-functional theory in chemical physics. **The Journal of Chemical Physics**, Melville, v. 140, n. 18, p. 18A301-1–18, 2014.

BENTLER, P. et al. Inverting Small Molecule–Protein Recognition by the Fluorine Gauche Effect: Selectivity Regulated by Multiple H→F Bioisosterism. **Angewandte Chemie - International Edition**, Weinheim, v. 58, n. 32, p. 10990–10994, 2019; **Angewandte Chemie**, Weinheim, v. 131, n. 32, p. 11106–11110, 2019.

BERGER, R. et al. Organic fluorine compounds: a great opportunity for enhanced materials properties. **Chemical Society Reviews**, Cambridge, v. 40, n. 7, p. 3496–3508, 2011.

BICKELHAUPT, F. M. et al. Central Bond in the Three $CN^{\bullet}$ Dimers NC–CN, CN–CN and CN–NC: Electron Pair Bonding and Pauli Repulsion Effects. **Journal of Physical Chemistry**, Washington, v. 96, n. 12, p. 4864–4873, 1992.

BICKELHAUPT, F. M.; BAERENDS, E. J. Kohn-Sham Density Functional Theory: Predicting and Understanding Chemistry. In: LIPKOWITZ, K. B.; BOYD, D. B. **Reviews in Computational Chemistry**, New York: John Wiley and Sons Inc., v. 15, p. 1–86, 2000.

BICKELHAUPT, F. M.; BAEREND, E. J. The case for steric repulsion causing the staggered conformation of ethane. **Angewandte Chemie - International Edition**, Weinheim, v. 42, n. 35, p. 4183–4188, 2003; **Angewandte Chemie**, Weinheim, v. 115, n. 35, p. 4315–4320, 2003.

BICKELHAUPT, F. M.; HOUK, K. N. Analyzing Reaction Rates with the Distortion/Interaction-Activation Strain Model. **Angewandte Chemie - International Edition**, Weinheim, v. 56, n. 34, p. 10070–10086, 2017; **Angewandte Chemie**, Weinheim, v. 129, n. 34, p. 10204–10221, 2017.

BLANKENSTEIN, J.; ZHU, J. Conformation-Directed Macrocyclization Reactions. **European Journal of Organic Chemistry**, Weinheim, v. 2005, n. 10, p. 1949–1964, 2005.

BROWN, T. L. et al. **Chemistry: The Central Science**. 9. ed. [s.l.] Pearson Prentice Hall, 2003.

BRUNCK, T.K.; WEINHOLD, F. Quantum-Mechanical Studies on the Origin of Barriers to Internal Rotation about Single Bonds. **Journal of the American Chemical Society**, Washington, v. 101, n. 7, p. 1700–1709, 1979.

BUISSONNEAUD, D. Y.; VAN MOURIK, T.; O'HAGAN, D. A DFT study on the origin of the fluorine gauche effect in substituted fluoroethanes. **Tetrahedron**, Oxford, v. 66, n. 12, p. 2196–2202, 2010.

BURKE, K. Perspective on density functional theory. **The Journal of Chemical Physics**, Melville, v. 136, n. 15, p. 150901-1–9, 2012.

BUTCHER, S. S.; COHEN, R. A.; ROUNDS, T. C. Microwave Spectrum of 1,2-Difluoroethane. **The Journal of Chemical Physics**, Woodbury, v. 54, n. 9, p. 4123–4124, 1971.

CAREY, F. A.; SUNDBERG, R. J. **Advanced organic chemistry**. 5. ed. Charlottesville: Springer-Verlag, 2007.
CHEN, R. et al. Conformational Design Principles in Total Synthesis. **Angewandte Chemie - International Edition**, Weinheim, v. 59, n. 34, p. 14198–14210, 2020; **Angewandte Chemie**, Weinheim, v. 132, n. 34, p. 14302–14314, 2020.

COHEN, A. J.; MORI-SÁNCHEZ, P.; YANG, W. Insights into current limitations of density functional theory, **Science**, Washington, v. 321, n. 5890, p. 792–794, 2008.

COHEN-TANNOUDJI, C.; DIU, B.; LALOË, F. **Quantum mechanics**. 1. ed. [s.l.] John Wiley & Sons. Inc., 2005.

DÍAZ, N. et al. Fluorine conformational effects characterized by energy decomposition analysis. **Physical Chemistry Chemical Physics**, Cambridge, v. 21, n. 45, p. 25258–25275, 2019.

ELIEL, E. L.; WILEN, S. H. **Stereochemistry of organic compounds**. [s.l.] John Wiley & Sons Inc., 1994.

FORESMAN, J. B.; FRISCH, E. **Exploring Chemistry with Electronic Structure Methods**. 2. ed. Pittsburgh: Gaussian Inc., 1996.

FRENKING, G. et al. Towards a rigorously defined quantum chemical analysis of the chemical bond in donor–acceptor complexes. **Coordination Chemistry Reviews**, Lausanne, v. 238, p. 55–82, 2003.

FRENKING, G.; BICKELHAUPT, F. M. The EDA Perspective of Chemical Bonding. In: FRENKING, G.; SHAIK, S. **The Chemical Bond: Fundamental Aspects of Chemical Bonding**; Weinheim: Wiley-VCH, p. 121–158, 2014.

FUJIWARA, T.; O'HAGAN, D. Successful fluorine-containing herbicide agrochemicals. **Journal of Fluorine Chemistry**, Lausanne, v. 167, p. 16–29, 2014.

GILLIS, E. P. et al. Applications of Fluorine in Medicinal Chemistry. **Journal of Medicinal Chemistry**, Washington, v. 58, n. 21, p. 8315–8359, 2015.

GOODMAN, L.; GU, H.; POPHRISTIC, V. Gauche Effect in 1,2-Difluoroethane. Hyperconjugation, Bent Bonds, Steric Repulsion. **Journal of Physical Chemistry A**, Washington, v. 109, n. 6, p. 1223–1229, 2005.

GRIMME, S. et al. A consistent and accurate ab initio parametrization of density functional dispersion correction (DFT-D) for the 94 elements H-Pu. **Journal of Chemical Physics**, Woodbury, v. 132, p. 154104, 2010.

GRIMME, S.; EHRLICH, S.; GOERIGK, L. Effect of the Damping Function in Dispersion Corrected Density Functional Theory. **Journal of Computational Chemistry**, Hoboken, v. 32, n. 7, p. 1456–1465, 2011.

HAMLIN, T. A.; FERNANDEZ, I.; BICKELHAUPT, F. M. How Dihalogens Catalyze Michael Addition Reactions. **Angewandte Chemie - International Edition**, Weinheim, v. 58, n. 26, p. 8922–8926, 2019; **Angewandte Chemie**, Weinheim, v. 131, n. 26, p. 9015–9020, 2019.

HAMLIN, T. A. et al. Energy decomposition analysis in the context of quantitative molecular orbital theory. In: GRABOWSKY, S. **Complementary Bonding Analysis**, Berlin: De Gruyter, p. 199–212, 2021.

HERNANDES, M. Z. et al. Halogen Atoms in the Modern Medicinal Chemistry: Hints for the Drug Design. **Current Drug Targets**, Sharjah, v. 11, n. 3, p. 303–314, 2010.

HOFFMANN, R. W. Conformation Design of Open-Chain Compounds. **Angewandte Chemie - International Edition**, Weinheim, v. 39, n. 12, p. 2054–2070, 2000; **Angewandte Chemie**, Weinheim, v. 112, n. 12, p. 2134–2150, 2000.

HOHENBERG, P.; KOHN, W. Inhomogeneous Electron Gas. **Physical Review**, College Park, v. 136, n. 3B, p. B864–B871, 1964.

HUNTER, L. The C-F bond as a conformational tool in organic and biological chemistry. **Beilstein Journal of Organic Chemistry**, Frankfurt, v. 6, n. 38, p. 1–14, 2010.

JENSEN, F. **Introduction to Computational Chemistry**. 2. ed. Chichester: John Wiley & Sons, Ltd, 2006.

JESCHKE, P. The unique role of halogen substituents in the design of modern agrochemicals. **Pest Management Science**, Sussex, v. 66, n. 1, p. 10–27, 2010.

JONAS, V.; FRENKING, G.; REETZ, M. T. Comparative Theoretical Study of Lewis Acid-Base Complexes of BH_3, BF_3, BCl_3, $AlCl_3$, and SO_2. **Journal of the American Chemical Society**, Washington, v. 116, n. 19, p. 8791–8753, 1994.

KARLICKÝ, F. et al. Halogenated Graphenes: Rapidly Growing Family of Graphene Derivatives. **ACS Nano**, Washington, v.7, n. 8, p. 6434–6464, 2013.

KEMP, J. D.; PITZER, K. S. Hindered Rotation of the Methyl Groups in Ethane. **The Journal of Chemical Physics**, Melville, v. 4, n. 11, p. 749–749, 1936.

KITAURA, K.; MOROKUMA, K. A new energy decomposition scheme for molecular interactions within the Hartree-Fock approximation. **International Journal of Quantum Chemistry**, Hoboken, v. 10, n. 2, p. 325–340, 1976.

KOCH, W.; HOLTHAUSEN, M. C. **A Chemist's Guide to Density Functional Theory**. 2. ed. Weinheim: Wiley-VCH, 2001.

KOHN, W.; SHAM, L. J. Self-Consistent Equations Including Exchange and Correlation Effects. **Physical Review**, College Park, v. 140, n. 4A, p. A1133–A1138, 1965.

KRAPP, A.; BICKELHAUPT, F. M.; FRENKING, G. Orbital Overlap and Chemical Bonding. **Chemistry - A European Journal**, Weinheim, v. 12, n. 36, p. 9196–9216, 2006.

LEOPOLD, K. R.; CANAGARATNA, M.; PHILLIPS, J. A. Partially Bonded Molecules from the Solid State to the Stratosphere. **Accounts of Chemical Research**, Washington, v. 30, n. 2, p. 57–64, 1997.

LEWIS, G. N. **Valence and the Structure of Atoms and Molecules**, New York: The Chemical Catalog Company, 1923.

LEWIS, G. N. Acids and bases. **Journal of the Franklin Institute**, Philadelphia, v. 226, n. 3, p. 293–313, 1938.

MARDIROSSIAN, N.; HEAD-GORDON, M. Thirty years of density functional theory in computational chemistry: an overview and extensive assessment of 200 density functionals. **Molecular Physics**, Oxon, v. 115, n. 19, p. 2315–2372, 2017.

MEANWELL, N. A. Fluorine and Fluorinated Motifs in the Design and Application of Bioisosteres for Drug Design. **Journal of Medicinal Chemistry**, Washington, v. 61, n. 14, p. 5822–5880, 2018.

MEDVEDEV, M. G. et al. Density functional theory is straying from the path toward the exact functional. **Science**, Washington, v. 355, n. 6320, p. 49–52, 2017.

MEI, H. et al. Fluorine-Containing Drugs Approved by the FDA in 2018. **Chemistry - A European Journal**, Weinheim, v. 25, n. 51, p. 11797–11819, 2019.

MÉNDEZ, M.; CEDILLO, A. Gas phase Lewis acidity and basicity scales for boranes, phosphines and amines based on the formation of donor–acceptor complexes. **Computational and Theoretical Chemistry**, Amsterdam, v. 1011, p. 44–56, 2013.

MO, Y.; GAO, J. Polarization and Charge-Transfer Effects in Lewis Acid-Base Complexes. **Journal of Physical Chemistry A**, Washington, v. 105, n. 26, p. 6530–6536, 2001.

MO, Y. et al. The magnitude of hyperconjugation in ethane: A perspective from Ab initio valence bond theory. **Angewandte Chemie - International Edition**, Weinheim, v. 43, n. 15, p. 1986–1990, 2004; **Angewandte Chemie**, Weinheim, v. 116, n. 15, p. 2020–2024, 2004a.

MO. Y. et al. Charge Transfer in the Electron Donor−Acceptor Complex BH_3NH_3. **Journal of the American Chemical Society**, Washington, v. 126, n. 12, p. 3974–3982, 2004b.

MO, Y.; GAO, J. Theoretical analysis of the rotational barrier in ethane. **Accounts of Chemical Research**, Washington, v. 40, n. 2, p. 113–119, 2007.
MOLNÁR, I. G. et al. Enantioselective Aziridination of Cyclic Enals Facilitated by the Fluorine-Iminium Ion *Gauche* Effect. **Chemistry - A European Journal**, Weinheim, v. 20, n. 3, p. 794–800, 2013.

MOROKUMA, K. Molecular orbital studies of hydrogen bonds. III. C=O···H-O hydrogen bond in $H_2CO···H_2O$ and $H_2CO···2H_2O$. **Journal of Chemical Physics**, Woodbury, v. 55, n. 3, p. 1236–1244, 1971.

MÜLLER, K.; FAEH, C.; DIEDERICH, F. Fluorine in Pharmaceuticals: Looking Beyond Intuition. **Science**, Washington, v. 317, n. 5846, p. 1881–1886, 2007.

NORI-SHARGH, D.; BOGGS, J. E. Complete basis set, hybrid-DFT study, and NBO interpretations of the conformational behavior of 1,2-dihaloethanes. **Structural Chemistry**, New York, v. 22, n. 2, p. 253–262, 2011.

PASTORCZAK, E.; CORMINBOEUF, C. Perspective: Found in translation: Quantum chemical tools for grasping noncovalent interactions. **The Journal of Chemical Physics**, Melville, v. 146, n. 12, p. 120901-1–13, 2017.

PATTISON, G. Conformational preferences of α-fluoroketones may influence their reactivity. **Beilstein Journal of Organic Chemistry**, Frankfurt, v. 13, p. 2915–2921, 2017.

PEARSON, R. G. Chemical hardness and density functional theory. **Journal of Chemical Sciences**, Bangalore, v. 117, n. 5, 369–377, 2005.

PHIPPS, M. J. S. et al. Energy decomposition analysis approaches and their evaluation on prototypical protein–drug interaction patterns. **Chemical Society Reviews**, Cambridge, v. 44, n. 10, p. 3177–3211, 2015.

PITZER, R. M. The Barrier to Internal Rotation in Ethane. **Accounts of Chemical Research**, Washington, v. 16, n. 6, p. 207–210, 1983.

POPHRISTIC, V.; GOODMAN, L. Hyperconjugation not steric repulsion leads to the staggered structure of ethane. **Nature**, London, v. 411, p. 565–568, 2001.

ROWSELL, B. D.; GILLESPIE, F. J.; HEARD, G. L. Ligand Close-Packing and the Lewis Acidity of BF_3 and BCl_3. **Inorganic Chemistry**, Washington, v. 38, n. 21, p. 4659–4662, 1999.

SCHREINER, P. R. Teaching the Right Reasons: Lessons from the Mistaken Origin of the Rotational Barrier in Ethane. **Angewandte Chemie - International Edition**, Weinheim, v. 41, n. 19, p. 3579–3581, 2002; **Angewandte Chemie**, Weinheim, v. 114, n. 19, p. 3729–3732, 2002.

SCHWARZ, W. H. E.; SCHMIDBAUR, H. Observations and Descriptions versus Explanations—An Example: Does Nature, Does Theory Know About Steric Hindrance? **Chemistry - A European Journal**, Weinheim, v. 18, n. 15, p. 4470–4479, 2012.
SENDEROWITZ, H.; FUCHS, B. Steric and stereoelectronic effects in saturated heterocycles I. Small molecular fragment constituents. Theory vs. experiment. **Journal of Molecular Structure – THEOCHEM**, Amsterdam, v. 395–396, p. 123–155, 1997.

SONG, L. et al. Steric strain versus hyperconjugative stabilization in ethane congeners. **Journal of Physical Chemistry A**, Washington, v. 109, n. 10, p. 2310–2316, 2005.

SOUZA, F. R.; FREITAS, M. P.; RITTNER, R. On the stereoelectronic effects governing the rotational isomerism of 1,2-dihaloethanes. **Journal of Molecular Structure – THEOCHEM**, Amsterdam, v. 863, n. 1–3, p. 137–140, 2008.

STAUBITZ, A. et al. Amine- and Phosphine-Borane Adducts: New Interest in Old Molecules. **Chemical Reviews**, Washington, v. 110, n. 7, p. 4023−4078, 2010.

STEPHAN, D. W.; ERKER, G. Frustrated Lewis Pairs: Metal-free Hydrogen Activation and More. **Angewandte Chemie - International Edition**, Weinheim, v. 49, n. 1, p. 46–76, 2010; **Angewandte Chemie**, Weinheim, v. 122, n. 1, p. 50–81, 2010.

STEPHAN, D. W. Frustrated Lewis Pairs. **Journal of the American Chemical Society**, Washington, v. 137, n. 32, p. 10018–10032, 2015.

STEPHAN, D. W.; ERKER, G. Frustrated Lewis Pair Chemistry: Development and Perspectives. **Angewandte Chemie - International Edition**, Weinheim, v. 54, n. 22, p. 6400–6441, 2015; **Angewandte Chemie**, Weinheim, v. 127, n. 22, p. 6498–6541, 2015.

STEPHAN, D. W. The broadening reach of frustrated Lewis pair chemistry. **Science**, Washington, v. 354, n. 6317, p. aaf7229-1–8, 2016.

SVATUNEK, D. et al. How the Lewis Base F– Catalyzes the 1,3-Dipolar Cycloaddition Between Carbon Dioxide and Nitrilimines. **Journal of Organic Chemistry**, Washington, v. 86, n. 5, p. 4320–4325, 2021.

TAKEO, H.; MATSUMURA, C. Microwave spectrum and molecular structure of gauche-1,2-difluoroethane. **The Journal of Chemical Physics**, Woodbury, v. 84, n. 8, p. 4205–4210, 1986.

THACKER, J. C. R.; POPELIER, P. L. A. Fluorine Gauche Effect Explained by Electrostatic Polarization Instead of Hyperconjugation: An Interacting Quantum Atoms (IQA) and Relative Energy Gradient (REG) Study. **Journal of Physical Chemistry A**, Washington, v. 122, n. 5, p. 1439–1450, 2018.

THIEHOFF, C. et al. The influence of electronic perturbations on the Sulfur–Fluorine Gauche Effect. **Journal of Fluorine Chemistry**, Lausanne, v. 182, p. 121–126, 2016.

THIEHOFF, C.; REY, Y. P.; GILMOUR, R. The Fluorine Gauche Effect: A Brief History. **Israel Journal of Chemistry**, Weinheim, v. 57, n. 1–2, p. 92–100, 2017.

VAN SCHAICK, E. J. M. et al. An electron diffraction study of the molecular structure of 1,2-difluoroethane. **Journal of Molecular Structure**, Amsterdam, v. 16, n. 1, p. 23–27, 1973.

VAN ZEIST, W. -J. et al. Reaction Coordinates and the Transition-Vector Approximation to the IRC. **Journal of Chemical Theory and Computation**, Washington, v. 4, n. 6, p. 920–928, 2008.

VERMEEREN, P. et al. Understanding chemical reactivity using the activation strain model. **Nature Protocols**, London, v. 15, n. 2, p. 649–667, 2020.

VERMEEREN, P. et al. Lewis Acid-Catalyzed Diels-Alder Reactions: Reactivity Trends Across the Periodic Table. **Chemistry - A European Journal**, Weinheim, 2021. No prelo.

WEINHOLD, F. A new twist on molecular shape. **Nature**, London, v. 411, p. 539–541, 2001.

WEINHOLD, F. Rebuttal to the Bickelhaupt–Baerends Case for Steric Repulsion Causing the Staggered Conformation of Ethane. **Angewandte Chemie - International Edition**, Weinheim, v. 42, n. 35, p. 4188–4194, 2003; **Angewandte Chemie**, Weinheim, v. 115, n. 35, p. 4320–4326, 2003.

WIBERG, K. B. et al. Origin of the Gauche Effect in Substituted Ethanes and Ethenes. **Journal of Physical Chemistry**, Washington, v. 94, n. 18, p. 6956–6959, 1990.

WIBERG, K. B. Bent Bonds in Organic Compounds. **Accounts of Chemical Research**, Washington, v. 29, n. 5, p. 229–234, 1996.

WOLFE, S. The Gauche Effect. Some Stereochemical Consequences of Adjacent Electron Pairs and Polar Bonds. **Accounts of Chemical Research**, Washington, v. 5, n. 3, p. 102–111, 1972.

WOLTERS, L. P.; BICKELHAUPT, F. M. The activation strain model and molecular orbital theory. **Wiley Interdisciplinary Reviews – Computational Molecular Science**, Hoboken, v. 5, n. 4, p. 324–343, 2015.

YANG, L.-P. et al. A supramolecular system that strictly follows the binding mechanism of conformational selection. **Nature Communications**, London, v. 11, 2740, 2020.

ZHENG, Y.; TICE, C. M.; SINGH, S. B. Conformational control in structure-based drug design. **Bioorganic & Medicinal Chemistry Letters**, Oxford, v. 27, n. 13, p. 2825–2837, 2017.

ZIEGLER, T.; RAUK, A. On the calculation of bonding energies by the Hartree Fock Slater method. I. The transition state method. **Theoretica chimica acta**, New York, v. 46, n. 1, p. 1–10, 1977.

ZIEGLER, T.; RAUK, A. A Theoretical Study of the Ethylene-Metal Bond in Complexes between Cu^{+}, Ag^{+}, Au^{+}, Pt^{0}, or Pt^{2+} and Ethylene, Based on the Hartree-Fock-Slater Transition-State Method. **Inorganic Chemistry**, Washington, v. 18, n. 6, p. 1558–1565, 1979a.

ZIEGLER, T.; RAUK, A. CO, CS, N_2, PF_3, and $CNCH_3$ as σ Donors and π Acceptors. A Theoretical Study by the Hartree-Fock-Slater Transition-State Method. **Inorganic Chemistry**, Washington, v. 18, n. 7, p. 1755–1759, 1979b.

SECOND SECTION – PAPERS

3 PAPER 1 – CONFORMERS OF 2-HALOCYCLOHEXANONE ANALOGS

Part of this chapter previously appeared as

Evaluation of the Alicyclic Gauche Effect in 2-Fluorocyclohexanone Analogs: a Combined NMR and DFT Study

D. Rodrigues Silva, L. A. Zeoly, R. A. Cormanich, C. Fonseca Guerra, M. P. Freitas

Eur. J. Org. Chem. **2020**, *2020*, 884–890

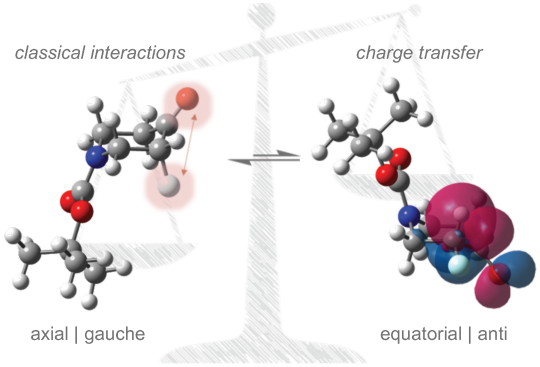

Abstract: Herein, we have investigated the effect of an endocyclic group (forming the N–C–C–F fragment) on the conformational preferences of 2-fluorocyclohexanone analogs. A combined approach of nuclear magnetic resonance and density functional theory calculations was employed to assess the conformational equilibrium in several media. In turn, natural bond orbital analysis and the conformational behavior of other 2-halocyclohexanone analogs were used to get more insights about the intramolecular interactions governing the conformer stabilities. Our results reveal that any stabilization from interactions featured in the *gauche* effect is overcome by a short-range interaction of the fluorine substituent with the carbonyl group. Consequently, the *gauche* effect in heterocyclic compounds is not as stabilizing as in their acyclic counterparts. Only the electrostatic *gauche* effect takes place even in polar solvents owing to an attraction between the axial fluorine and an endocyclic quaternary ammonium group.

Keywords: Axial-equatorial equilibrium, Conformation analysis, Fluorine *gauche* effect, Heterocycles, Stereoelectronic effects

3.1 Introduction

The 2-fluorocyclohexanone moiety is a molecular building block of organic compounds with application in several research fields. It has a well-defined conformational equilibrium, in which the six membered ring undergoes chair inversion resulting in energy minimum conformations with either axial or equatorial fluorine atom (Figure 3.1) with a significant solvent dependence.[1] The axial fluorine is the most stable conformer in the gas phase, but the equilibrium gradually shifts towards the equatorial conformer with the increase of the solvent polarity. The equatorial conformer has a higher dipole moment and is naturally more stabilized by polar solvents. Nevertheless, this conformational preference has usually been attributed to an interplay of intramolecular interactions involving the carbonyl group.[2] In the gas phase, there is a repulsion between the equatorial fluorine and the carbonyl group (the C–F and C=O bonds are almost parallel to each other in the same plane), forcing the fluorine to adopt an axial orientation. Insofar as the polarity of the solvent increases, the repulsion is attenuated and a charge transfer from the σ_{CHax} bond to the antibonding π^*_{CO} orbital overrides other interactions to favor the equatorial conformer (Figure 3.1).[2]

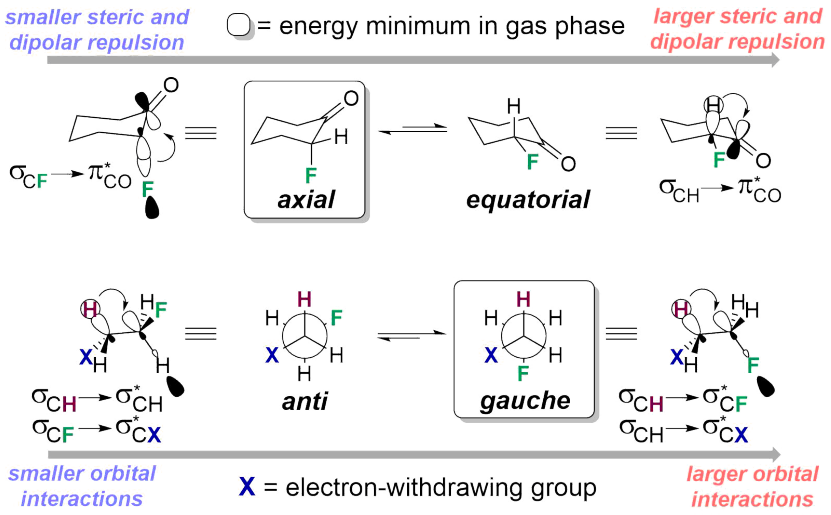

Figure 3.1: Schematic representation of the axial-equatorial equilibrium in the 2-fluorocyclohexanone (on the top) along with the *anti-gauche* equilibrium in the 1,2-disubstituted ethane (on the bottom).

The introduction of a fluorine atom in an organic molecule is known to impart predictable stereoelectronic effects that can change its conformational behavior; a compelling example is the *gauche* effect.[3] The *gauche* effect is observed in structures containing two bonded carbon atoms attached to vicinal electron withdrawing groups (in the F–C–C–X form for organofluorine compounds), in which the F and X preferentially adopt the *gauche*

orientation (*i.e.*, $\varphi_{F–C–C–X} \approx 60°$) instead of the *anti*-orientation (*i.e.*, $\varphi_{F–C–C–X} \approx 180°$), Figure 3.1. The *gauche* preference has been commonly explained in terms of hyperconjugative interactions.[4] That is, the destabilizing effect of bringing two electron rich groups close together is overcome by a greater stabilization from antiperiplanar orbital interactions. The best electron donor (*i.e.*, σ_{CH} bond) and acceptor (*i.e.*, σ^*_{CF} antibonding) orbitals are aligned in the *gauche* arrangement for the $\sigma_{CH} \rightarrow \sigma^*_{CF/CX}$ charge transfer, in contrast to the $\sigma_{CH} \rightarrow \sigma^*_{CH}$ and $\sigma_{CF} \rightarrow \sigma^*_{CX}$ in the *anti*-orientation (Figure 3.1).[5]

If compared with other intramolecular interactions (such as hydrogen bonds and electrostatic interactions), the *gauche* effect may have only a subtle effect on the conformational preferences of organic compounds.[3a] Nonetheless, its strength depends on the groups involved;[6] the *gauche-anti* energy difference in some fluoroethylamides, for example, can be of 1.8 kcal mol^{-1} in favor of the *gauche* conformer.[7] In fact, the *gauche* effect has been exploited as a conformational control strategy in the design of performance organic compounds in catalysis,[8] biological systems,[9] and organometallic complexes.[10] With this in mind, we wonder if the introduction of an endocyclic group, such as a carbamate group, in the structure of the 2-fluorocyclohexanone could induce a conformational shift to further stabilize the axial fluorine due to the *gauche* effect. A recent report has suggested that the reactivity of some α-fluoroketones may be related to their conformational preferences.[11] Therefore, a conformational induction in the 2-fluorocyclohexanone backbone could be used to modulate a desired molecular property, such as reactivity towards a specific reaction mechanism.[12]

In an initiative to induce a *gauche* effect in the backbone of the 2-fluorocyclohexanone, Silva et al.[13] introduced an oxygen atom in the six-membered ring in order to attain a *gauche* arrangement along the $O_{endo}–C–C–F_{ax}$ fragment. However, it actually caused an incremental repulsion between oxygen and axial fluorine, which favored the equatorial conformer even in the gas phase. In the case of the endocyclic carbamate group envisaged here, it is expected a smaller repulsion because the endocyclic nitrogen atom is engaged in a resonance with the carbonyl group. Therefore, the stabilizing orbital interactions in the *gauche* arrangement would overcome other intramolecular interactions to favor the axial fluorine.

Thus, the conformational analysis of the 1-Boc-3-fluoro-4-oxopiperidine (**1**, Figure 3.2) is performed herein. Compound **1** has an endocyclic *N*-Boc group in the six membered ring that could result in a *gauche* orientation with the axial fluorine atom, instead of an *anti*-orientation with equatorial fluorine. The Boc group acts as a protective group and **1** has been commonly employed as an intermediate in organic synthesis.[14] Therefore, this work aims at investigating whether the *N*-Boc group introduces intramolecular interactions (especially orbital interactions

due to the *gauche* effect) that could cooperatively act with the carbonyl group to increase the fluorine axial preference, even in solution. For this, the energy minimum conformations of **1** and their population in different media were investigated by a combined approach using nuclear magnetic resonance (NMR) and density functional theory (DFT) calculations, and then the prospective intramolecular interactions responsible for their relative stability were theoretically evaluated. In addition, the *N*-Boc group in **1** was successively replaced with other groups, as well as the fluorine at position 2 (see atom numbering in Figure 3.2), to theoretically find an optimal substituent activating the alicyclic *gauche* effect.

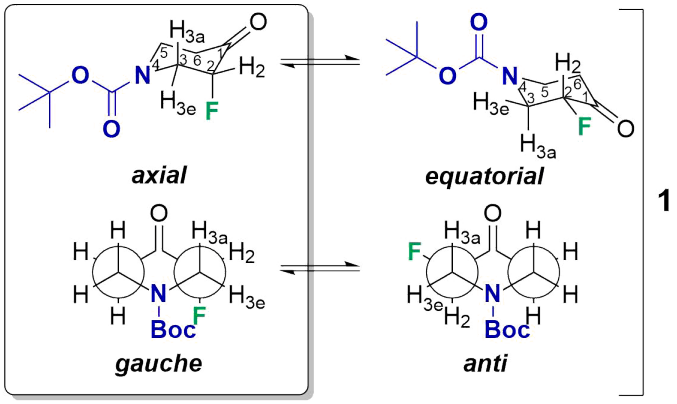

Figure 3.2: Conformational equilibrium of the 1-Boc-3-fluoro-4-oxopiperidine (**1**). The antiperiplanar interactions (*i.e.*, $\sigma_{CH} \rightarrow \sigma^*_{CF}$ and $\sigma_{CH} \rightarrow \sigma^*_{CN}$) present in the *gauche* orientation of the endocyclic nitrogen with fluorine atom are expected to stabilize the axial conformer of **1**.

3.2 Results and discussion

The first step towards investigating the conformational landscape of **1** consisted in evaluating the orientation of the *N*-Boc group through rotation around the N–C(=O) bond. Due to the resonance in the carbamate group, it is expected a planar geometry along the N–C(=O)–O atoms and then two orientations for the Boc's carbonyl group with $\varphi_{C-N-C=O}$ dihedral angle of about 0° and 180°. Thus, the energy profile at the MP2/6-311++G(d,p)[15] level for the axial and equatorial conformers of **1** as a function of the $\varphi_{C-N-C=O}$ dihedral angle is shown in Figure 3.3. Two energy minima (named $\mathbf{1}^{syn}$ and $\mathbf{1}^{anti}$) were found for both conformers, as expected, in which the second one ($\varphi_{C-N-C=O} \approx 180°$) is somewhat more stable. The energy difference between them is small and more significant for the axial (ΔE = 0.96 kcal mol^{-1}) than for the equatorial (ΔE = 0.63 kcal mol^{-1}) conformation. Likewise, Figure 3.3 shows two energy maxima, with the $\varphi_{C-N-C=O}$ dihedral angle of 120° and 300° for both conformers. The interconversion barrier is higher for the axial form (*ca.* 18 kcal mol^{-1} compared to 13 kcal mol^{-}

[1] in the equatorial form), probably because of the closer proximity between the axial fluorine and both oxygen atoms of the Boc group in the energy maximum structures.

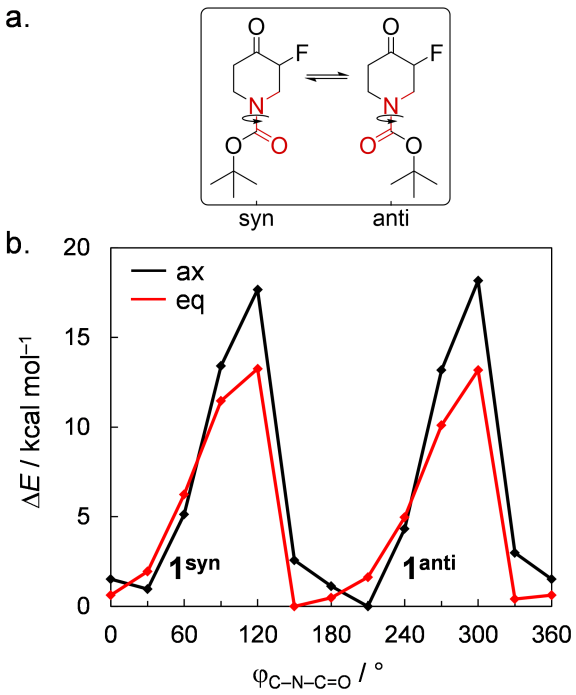

Figure 3.3: a) Schematic representation for the interconversion between conformers $\mathbf{1}^{\mathbf{syn}}$ and $\mathbf{1}^{\mathbf{anti}}$ through rotation of the N–C(=O) bond; b) energy profile for the rotation around the $\varphi_{C-N-C=O}$ torsion angle with a step size of 30° at MP2/6-311++G(d,p) level for the axial (black curve) and equatorial (red curve) conformers of **1**.

The geometries of the four energy minima located in Figure 3.3 were then fully optimized using dispersion-corrected B3LYP,[16] according to the DFT-D3(BJ) method developed by Grimme and coworkers,[17] with the 6-311++G(d,p) basis set.[15b] This level of theory was selected based on a benchmark study with MP2, see Experimental section and Appendix 3.1 for details. Interconversion between these four structures through sequential steps of N–C(=O) bond rotation and ring flipping forms the conformational cycle depicted in the Figure 3.4. The conformers have been labelled in the Figure 3.4 to distinguish the two orientations of the *N*-Boc group (**syn** and **anti**) and axial or equatorial fluorine (**ax** and **eq**, respectively), and the conformational equilibrium between these four structures (namely $\mathbf{1}^{\mathbf{syn}}_{\mathbf{ax}}$, $\mathbf{1}^{\mathbf{anti}}_{\mathbf{ax}}$, $\mathbf{1}^{\mathbf{syn}}_{\mathbf{eq}}$, and $\mathbf{1}^{\mathbf{anti}}_{\mathbf{eq}}$) has been investigated herein.

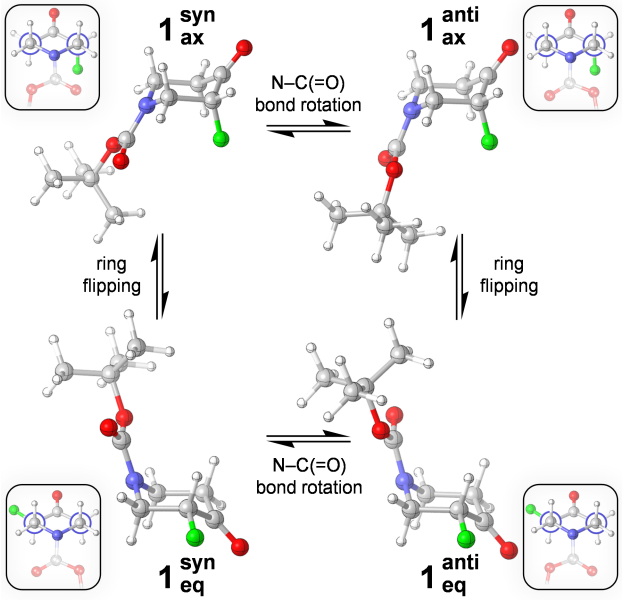

Figure 3.4: Conformational equilibrium among the four conformers of **1** studied at the B3LYP-D3(BJ)/6-311++G(d,p) level.

Conformational populations according to the Gibbs free energy in the gas phase and in implicit media, using solvents with increasing polarity (namely cyclohexane, chloroform, acetonitrile, and DMSO), were calculated to evaluate the influence of the solvent on this conformational equilibrium. The results are shown in the Figure 3.5. Conformer $\mathbf{1}_{\mathbf{ax}}^{\mathbf{anti}}$ is the global energy minimum (*i.e.*, it has the highest population) in the gas phase, in which the conformational energy increases in the order: $\mathbf{1}_{\mathbf{ax}}^{\mathbf{anti}} < \mathbf{1}_{\mathbf{eq}}^{\mathbf{anti}} < \mathbf{1}_{\mathbf{ax}}^{\mathbf{syn}} < \mathbf{1}_{\mathbf{eq}}^{\mathbf{syn}}$. Thus, there is a preference for the axial fluorine and the orientation *anti* of the Boc group in the gas phase. It is worth mentioning that the energy difference between conformations is small, less than a 1 kcal mol^{-1} (the electronic and Gibbs free energies of conformers in all tested media are given in Appendix 3.2). The conformational trends change with the inclusion of the solvent. The total axial population (*i.e.*, conformers $\mathbf{1}_{\mathbf{ax}}^{\mathbf{syn}}$ and $\mathbf{1}_{\mathbf{ax}}^{\mathbf{anti}}$ together) goes from 60% in the gas phase, 41% in cyclohexane, 30% in chloroform, to 16% in acetonitrile and in DMSO. Therefore, when the effect of the solvent is taken into account, the conformational equilibrium gradually shifts towards equatorial conformers. These results can be directly compared to the molecular dipole of the structures (μ = 3.27, 2.63, 3.74, and 5.42 D for the $\mathbf{1}_{\mathbf{ax}}^{\mathbf{syn}}$, $\mathbf{1}_{\mathbf{ax}}^{\mathbf{anti}}$, $\mathbf{1}_{\mathbf{eq}}^{\mathbf{anti}}$, and $\mathbf{1}_{\mathbf{eq}}^{\mathbf{syn}}$ conformers, respectively), since equatorial conformers have higher molecular dipole moments (therefore, they are more stabilized by polar solvents) than axial conformers.

To experimentally corroborate these findings, the conformational equilibrium of **1** was evaluated through ^{1}H NMR studies. The interconversion of one conformation into another

usually proceeds quite fast at room temperature, so in the NMR experiments an average signal over all conformers is measured instead of the individual conformers. However, due to the angular dependence of the three-bond hydrogen coupling constant ($^3J_{HH}$) expressed by the Karplus equation,[18] the conformational population of cyclic compounds can be easily estimated by the difference in the $^3J_{HH}$ between axial and equatorial conformers. The spin–spin coupling constants (J) in the same solvents tested in the theoretical calculations (*i.e.*, cyclohexane, chloroform, acetonitrile, and DMSO) are given in the Table 3.1. Because **1** has low solubility in cyclohexane and chloroform, it was not possible to accurately determine J in these solvents. Nevertheless, an increase in the $^3J_{HH}$ can be observed in more polar solvents, which indicates the equatorial preference in solution (because of the greater coupling between axial–axial hydrogens in the equatorial conformer, $\varphi_{H2–C–C–H3a} \approx 180°$, see numbering in the Figure 3.2), in line with theoretical calculations in implicit solvent.

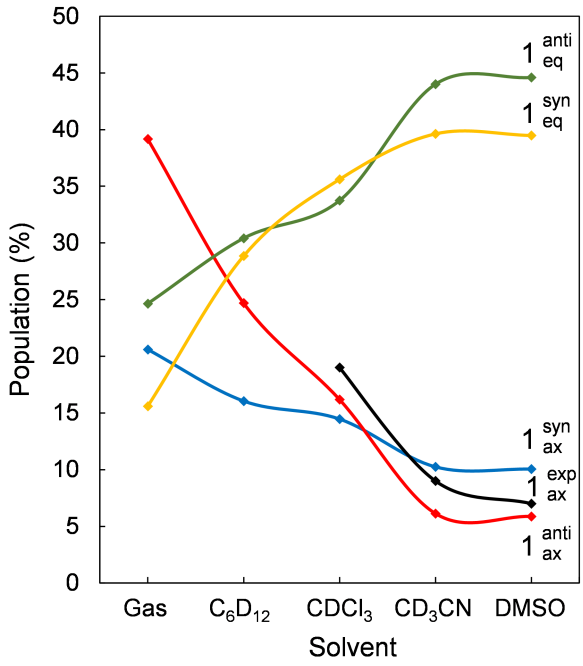

Figure 3.5: Conformational population according to the Boltzmann distribution of the Gibbs free energies in B3LYP-D3(BJ)/6-311++G(d,p) as a function of the polarity of the solvent (dipole moment of the solvents increases from the left to the right). Axial population estimated experimentally by NMR ($\mathbf{1}_{\mathbf{ax}}^{\mathbf{exp}}$, black curve) is shown for comparison purposes. (**ax**: axial, **eq**: equatorial, **syn**: $\varphi_{C–N–C=O} \approx 0°$, **anti**: $\varphi_{C–N–C=O} \approx 180°$).

The J for the individual conformers ($\mathbf{1}_{\mathbf{ax}}^{\mathbf{syn}}$, $\mathbf{1}_{\mathbf{ax}}^{\mathbf{anti}}$, $\mathbf{1}_{\mathbf{eq}}^{\mathbf{anti}}$, and $\mathbf{1}_{\mathbf{eq}}^{\mathbf{syn}}$) was calculated using B3LYP–D3(BJ)/EPR–III (a basis set specifically optimized for coupling constant calculations

by DFT[19]) and compared with experimental coupling constant (J_{obs}) to estimate the conformational populations using the following Eq. (3.1) and Eq. (3.2):

$$J_{obs} = n_{ax}J_{ax} + n_{eq}J_{eq} \quad (3.1)$$

$$n_{ax} + n_{eq} = 1 \quad (3.2)$$

wherein J_{ax} and J_{eq} are the individual coupling constants obtained theoretically and n_{ax} and n_{eq} are the mole ratios of the axial and equatorial conformers, respectively. The results are also shown in the Table 3.1. The calculated $^2J_{H_2F}$ and $^4J_{H_2H_6}$ (see numbering in the Figure 3.2) agree satisfactorily well with experimental measures ($^2J_{HF} \approx 50$ Hz and $^4J_{HH} \approx 1.1$ Hz). The $^3J_{H_2H_{3a}}$ shows the angular dependence in which equatorial and axial conformers have the $^3J_{H_2H_{3a}}$ of *ca.* 11 Hz and 1 Hz, respectively. The population in each medium was estimated [using Eqs. (3.1) and (3.2)] based on an average of the calculated $^3J_{H_2H_{3a}}$ to give the following axial mole ratios (regarding the two axial conformers $\mathbf{1}_{ax}^{syn}$ and $\mathbf{1}_{ax}^{anti}$): 0.20 (chloroform), 0.10 (acetonitrile), and 0.08 (DMSO), black curve in the Figure 3.5. Therefore, there is a decrease in the axial population on going to more polar media as predicted by the theoretical calculations.

Table 3.1: NMR coupling constants (J, in Hz) obtained experimentally and theoretically for the individual conformers of **1** in implicit solvents at the B3LYP-D3(BJ)/EPR–III//B3LYP-D3(BJ)/6-311++G(d,p) level. Estimated axial mole ratios in each media are given in parenthesis.

	Cyclohexane[a]				**Chloroform** (n_{ax} = 0.20)			
Conf.	$^2J_{H2,F}$	$^3J_{H2,H3a}$	$^3J_{H2,H3e}$	$^4J_{H2,H6}$	$^2J_{H2,F}$	$^3J_{H2,H3a}$	$^3J_{H2,H3e}$	$^4J_{H2,H6}$
$\mathbf{1}_{ax}^{syn}$	55.8	1.3	3.6	1.1	55.6	1.3	3.6	1.1
$\mathbf{1}_{ax}^{anti}$	56.1	1.2	3.6	1.1	55.9	1.2	3.6	1.1
$\mathbf{1}_{eq}^{anti}$	53.7	11.2	8.1	1.6	53.7	11.2	8.2	1.7
$\mathbf{1}_{eq}^{syn}$	53.3	11.0	8.4	1.6	53.4	11.0	8.5	1.7
Exp.	≈50.0	n.d.[a]	n.d.[a]	n.d.[a]	48.2	≈9.1	n.d.[a]	n.d.[a]
	Acetonitrile (n_{ax} = 0.10)				**DMSO** (n_{ax} = 0.08)			
Conf.	$^2J_{H2,F}$	$^3J_{H2,H3a}$	$^3J_{H2,H3e}$	$^4J_{H2,H6}$	$^2J_{H2,F}$	$^3J_{H2,H3a}$	$^3J_{H2,H3e}$	$^4J_{H2,H6}$
$\mathbf{1}_{ax}^{syn}$	55.5	1.3	3.5	1.1	55.5	1.3	3.5	1.1
$\mathbf{1}_{ax}^{anti}$	55.7	1.2	3.6	1.2	55.6	1.2	3.6	1.2
$\mathbf{1}_{eq}^{anti}$	53.7	11.2	8.3	1.8	53.7	11.2	8.3	1.8
$\mathbf{1}_{eq}^{syn}$	53.5	11.0	8.5	1.8	53.5	11.0	8.5	1.8
Exp.	47.5	10.1	6.6	1.1	47.2	10.3	6.7	1.1

[a] Not determined (n.d.) because of the signal broadening attributed to the low solubility in the given media.

By analyzing the conformational populations of **1**, it seems that the introduction of an endocyclic *N*-Boc group does not significantly change the conformational preferences in the 2-fluorocyclohexanone backbone. The axial population of **1** in the gas phase is similar to the one reported for the 2-fluorocyclohexanone itself[1b] (60% and 64%, respectively) and the equatorial conformer is preferred in solution. A similar behavior is observed if the fluorine atom in **1** is replaced by chlorine and bromine (to form **1′** and **1″**, respectively, see Appendices 3.3 and 3.4). These halogens are larger than fluorine and, therefore, conformational changes would be more affected by long-range interactions, if any, in these cases. However, the total axial population of **1′** and **1″** in the gas phase is 88% and 85%, respectively, which is quite similar to their 2-halocyclohexanone counterparts (86% and 92%,[1b] respectively), also highlighting the small effect of the *N*-Boc group on the conformational energies.

Therefore, at a first sight, it was not possible to observe the effect of the orbital interactions expected to be introduced with the *N*-Boc group to further stabilize the axial fluorine conformer. To get more insights on how the *N*-Boc group influences the relative stability of the isolated conformers of **1**, the total electronic energy in the gas phase (ΔE) of each conformer was decomposed within the framework of the Natural Bond Orbital (NBO) analysis[20] into three terms: non-Lewis (ΔE_{NL}, which accounts for charge transfer or delocalization energy), Lewis (ΔE_{L}, classical interactions) and dispersion (ΔE_{DISP}, since the electronic energy was calculated using dispersion corrections[17]). The NBO results are graphically represented in the Figure 3.6 (see Appendix 3.3 for details), wherein all energy terms are represented relative to the global energy minimum (*i.e.*, conformer $\mathbf{1}_{\mathbf{ax}}^{\mathbf{anti}}$). The ΔE_{DISP} term (yellow curve in Figure 3.6) has the smallest contribution to the ΔE (blue curve) and it is somehow uniform between conformers. The axial conformers ($\mathbf{1}_{\mathbf{ax}}^{\mathbf{syn}}$ and $\mathbf{1}_{\mathbf{ax}}^{\mathbf{anti}}$) are in general more stabilized by the ΔE_{L} term (green curve) while equatorial conformers ($\mathbf{1}_{\mathbf{eq}}^{\mathbf{anti}}$ and $\mathbf{1}_{\mathbf{eq}}^{\mathbf{syn}}$) are more stabilized by the ΔE_{NL} term (red curve). This trend can be associated with the intramolecular interactions used to explain the conformational energies in 2-fluorocyclohexanone.[2a,13] In equatorial conformers, there is a repulsion of the fluorine atom with the carbonyl group, as expressed by the less stabilizing ΔE_{L} energy of $\mathbf{1}_{\mathbf{eq}}^{\mathbf{anti}}$ and $\mathbf{1}_{\mathbf{eq}}^{\mathbf{syn}}$ (6.33 and 6.87 kcal mol^{-1}, respectively), and a greater stabilization from the $\sigma_{CHax} \rightarrow \pi^*_{CO}$ charge transfer, as expressed by the more stabilizing ΔE_{NL} energy (–6.18 and –6.52 kcal mol^{-1} for $\mathbf{1}_{\mathbf{eq}}^{\mathbf{anti}}$ and $\mathbf{1}_{\mathbf{eq}}^{\mathbf{syn}}$, respectively).

To estimate the contribution of the hyperconjugation interactions featured in the *gauche* effect to the conformational energies, we looked at the second order perturbation energy [$E^{(2)}_{i\rightarrow j} = 2F(i,j)^2/(\varepsilon_j - \varepsilon_i)$; $F(i,j)$ is the off-diagonal matrix element, ε_j and ε_i are the orbital energies[21]]

in the NBO analysis that estimates delocalization energies from orbital interactions (see Appendix 3.5). The $\sigma_{CH} \rightarrow \sigma^*_{CF}$ and $\sigma_{CH} \rightarrow \sigma^*_{CN}$ antiperiplanar interactions (4.6 and 2.9 kcal mol^{-1}, respectively) in the *gauche* orientation (*i.e.*, in the axial conformers) are indeed more stabilizing than the corresponding $\sigma_{CH} \rightarrow \sigma^*_{CH}$ and $\sigma_{CF/CN} \rightarrow \sigma^*_{CN/CF}$ interactions (2.3, 1.1, and 1.8 kcal mol^{-1}, respectively) in the *anti*-orientation (*i.e.*, in the equatorial conformers). However, equatorial conformers are still more stabilized by the ΔE_{NL} term, so it seems that these orbital interactions are not stabilizing enough to change the equilibria towards axial conformers as first expected. The $\sigma_{CHax} \rightarrow \pi^*_{CO}$ charge transfer in equatorial conformers, on the other hand, accounts for 6.7 kcal mol^{-1} (see Appendix 3.5), which is more stabilizing than the abovementioned interactions in the axial conformers and explains the trends in ΔE_{NL}. The main orbital interactions are schematically represented in the Appendix 3.6.

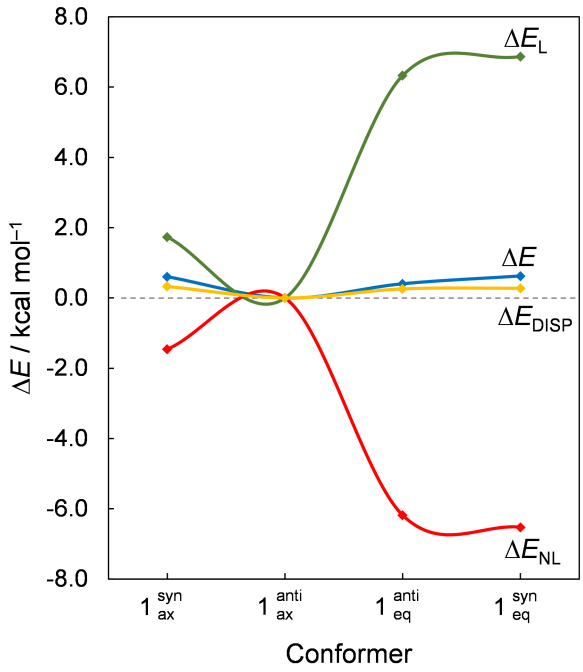

Figure 3.6: Energy decomposition scheme of the NBO analysis calculated using B3LYP-D3(BJ)/6-311++G(d,p) for the four conformers of **1** (**ax**: axial, **eq**: equatorial, **syn**: $\varphi_{C-N-C=O} \approx 0°$, **anti**: $\varphi_{C-N-C=O} \approx 180°$).

The *N*-Boc is a bulky group though, so it might introduce factors other than the *gauche* effect that influence the fluorine axial-equatorial preference. Thus, to simplify the system and get more insight on the role of specific structural parts, the relative energies of **1** were also compared with other 2-fluorocyclohexanone analogs (see Figure 3.7). **2** and **3** were chosen as to gradually reduce the *N*-Boc group and to evaluate the role of specific structural parts on the

conformational energies. The conformers of all analogs were named in the same manner as for **1**, to distinguish the two orientations of the N–C=O group (**syn** and **anti**, $\varphi_{C-N-C=O} \approx 0°$ and 180°, respectively) and axial or equatorial fluorine (**ax** and **eq**, respectively). Schematic representation of the conformers of analogs **2** and **3** is given in Appendix 3.4.

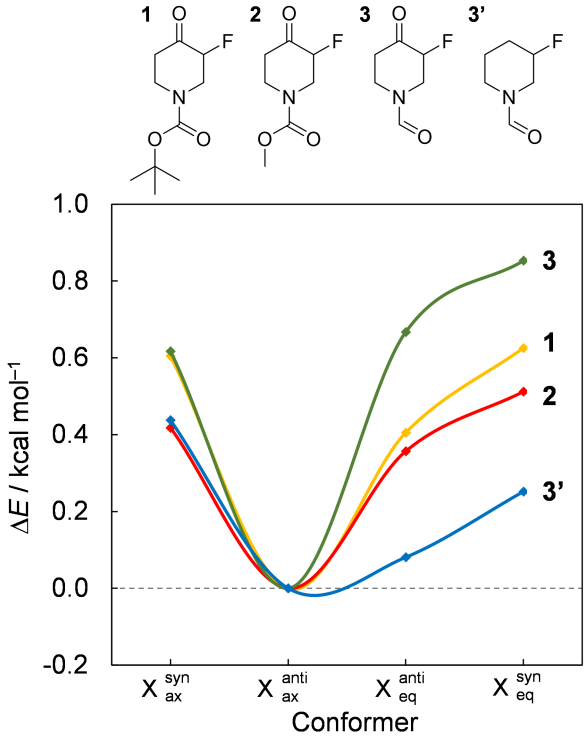

Figure 3.7: Relative conformational energies for the 2-fluorocyclohexanone analogs, where **X** = **1**–**3**. (**ax**: axial, **eq**: equatorial, **syn**: $\varphi_{C-N-C=O} \approx 0°$, **anti**: $\varphi_{C-N-C=O} \approx 180°$), computed at the B3LYP-D3(BJ)/6-311++G(d,p) level.

According to Figure 3.7, the energy trends of analogs **2** and **3** are quite similar to **1** (also regarding the energy trends in the NBO analysis, Appendix 3.3). The $\mathbf{X}_{\mathbf{ax}}^{\mathbf{anti}}$ is the global energy minimum and the conformational energy increases in the order: $\mathbf{X}_{\mathbf{ax}}^{\mathbf{anti}} < \mathbf{X}_{\mathbf{eq}}^{\mathbf{anti}} \approx \mathbf{X}_{\mathbf{ax}}^{\mathbf{syn}} < \mathbf{X}_{\mathbf{eq}}^{\mathbf{syn}}$. Due to the overall similarity in the energy trends on going from **1** to **3**, *i.e.*, on removing the *t*Bu group and the oxygen atom linked to it from the Boc group (Figure 3.7), it was possible to reduce the influence of the *N*-Boc group on the conformational stability of **1** to the amide group of analog **3**. Therefore, to specifically search for the *gauche* effect, the interaction between this amide group with the fluorine atom, without the influence of the ketone group (compound **3′** in Figure 3.7), was then evaluated. The removal of the carbonyl group to form **3′** leads to a

decrease in the relative energies among conformers (see Figure 3.7). In this case, the orientation of the amide group is more relevant for the conformational energies than the orientation of the fluorine atom. Conformers $\mathbf{3'^{anti}_{ax}}$ and $\mathbf{3'^{anti}_{eq}}$ have nearly the same total energy, and the energy difference between $\mathbf{3'^{syn}_{ax}}$–$\mathbf{3'^{anti}_{ax}}$ and $\mathbf{3'^{syn}_{eq}}$–$\mathbf{3'^{anti}_{eq}}$ is 0.44 and 0.17 kcal mol^{-1}, respectively. The energy difference is more significant for the axial fluorine probably due to the closer proximity with the amide carbonyl oxygen in $\mathbf{3'^{syn}_{ax}}$ (see Appendix 3.4). Additionally, the ΔE_{NL} and ΔE_{L} terms from the NBO analysis have opposite trends compared to **1**–**3** (see Appendix 3.3). With the removal of the carbonyl group, the $\sigma_{CH} \rightarrow \pi^{*}_{CO}$ charge transfer and the F_{eq}/C=O repulsion used to explain the conformational stability of the 2-fluorocyclohexanone are cancelled out. Now axial conformers are more favored by the ΔE_{NL} term, which can be related to the orbital interactions featured in the *gauche* effect, and less favored by the ΔE_{L} term relative to equatorial conformers, due to the removal of the F_{eq}/C=O repulsion and also to a possible incremental repulsion of the axial fluorine with the amide group.

Differently from other structures containing the fluoroethylamide fragment,[7] a stereoelectronic stabilization in the *gauche* arrangement is not the determining factor in the conformational behavior of the 2-fluorocyclohexanone analogs analyzed herein. Even without the influence of the ketone group in **3′**, the energy difference between axial and equatorial conformers (*gauche* and *anti*, respectively) is too small to observe any substantial stabilization due to the *gauche* effect. Earlier reports in the literature[13,22] have evaluated other endocyclic groups at the same position of the 2-fluorocyclohexanone backbone known to induce the *gauche* effect in acyclic compounds (*e.g.*, X = O[13] and S[22]). However, in all cases the conformational trends could not be attributed to hyperconjugation. It seems that the orbital interactions used to explain the preferred *gauche* orientation in acyclic compounds are, surprisingly, not strong enough to dictate the conformational preferences in heterocycles. Instead, conformational preferences of the 2-fluorocyclohexanone analogs are primarily affected by a short-range interaction with the ketone group.

To counterbalance the effect of the carbonyl group on the axial-equatorial equilibrium it is necessary to add an endocyclic group which can induce a stronger intramolecular interaction, probably electrostatic in nature. Thus, if the *N*-Boc group is continuously reduced to form analog **4** (which possesses only a hydrogen attached to the nitrogen atom, resembling part of the active nucleus of a 4-quinolone), then one can see a totally different trend (Table 2, see Appendix 3.3 for details). The conformational analysis of **4** has already been reported in the literature,[22] where the stability of the global energy minimum (which have both fluorine and

N–hydrogen atoms in the axial, $\mathbf{4}^{\mathbf{H\text{-}ax}}_{\mathbf{F\text{-}ax}}$ in Appendix 3.4) is attributed to an N–H$^{\delta+}\cdots^{\delta-}$F electrostatic interaction (in line with our NBO results in Appendix 3.3). This effect becomes stronger by protonating the amine group (to form analog **5**, the 3-fluoro-4-oxopiperidin-1-ium cation, in Table 2; see schematic representation in Appendix 3.4). In this case, the axial fluorine persists even in highly polar solvents, such as DMSO (Table 2), similar to the results reported for the 3-fluoropiperidinium cation that have been attributed to the so-called electrostatic *gauche* effect.[14d,23]

Table 3.2: Relative conformational energies (in kcal mol^{-1}) for the 2-fluorocyclohexanone analogs **4** and **5**, in gas phase and DMSO, computed at the B3LYP-D3(BJ)/6-311++G(d,p) level.

	4 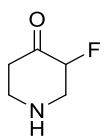			**5** 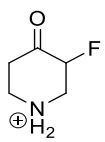	
Conf.	gas	DMSO	Conf.	gas	DMSO
$\mathbf{4}^{\mathbf{H\text{-}ax}}_{\mathbf{F\text{-}ax}}$	0.0	1.1	$\mathbf{5}_{\mathbf{F\text{-}ax}}$	0.0	0.0
$\mathbf{4}^{\mathbf{H\text{-}eq}}_{\mathbf{F\text{-}ax}}$	2.4	2.8			
$\mathbf{4}^{\mathbf{H\text{-}ax}}_{\mathbf{F\text{-}eq}}$	1.6	0.0			
$\mathbf{4}^{\mathbf{H\text{-}eq}}_{\mathbf{F\text{-}eq}}$	1.4	0.8	$\mathbf{5}_{\mathbf{F\text{-}eq}}$	5.4	0.3

3.3 Conclusion

The conformational preferences of **1** predicted by DFT calculations nicely reproduce the trends in the NMR experiments. There is an increase in the population of equatorial conformers on going from nonpolar to increasingly more polar solvents, as evidenced by the analysis of the $^3J_{HH}$ coupling constant. The conformational trends of **1** are quite similar to that of 2-fluorocyclohexanone itself (the same is observed for other 2-halocyclohexanones). The introduction of the endocyclic *N*-Boc group does not result in a significant stabilization of the axial fluorine due to interactions responsible for the *gauche* effect; the stabilization from hyperconjugation interactions featured in the *gauche* effect is overcome by the charge transfer from the occupied σ_{CHax} orbital to the empty π^*_{CO} orbital in the equatorial conformers. Through comparison with analogs **2**–**5**, it is possible to assess the influence of specific structural parts to the relative energies. The axial-equatorial equilibrium of the heterocycles analyzed herein is primarily dictated by the ketone group of the 2-fluorocyclohexanone backbone; however, an endocyclic group inducing strong electrostatic interactions shifts the conformational

preferences. Given the widely applicability of organofluorine compounds, understanding the factors ruling their molecular structure can assist in the design of novel compounds with improved molecular properties.

3.4 Experimental section

Commercial samples of 1-Boc-3-fluoro-4-oxopiperidine (**1**) were purchased and used without further purification. The ^{1}H NMR spectra were acquired at 499.99 MHz from 2.0 mg mL^{-1} solution of **1** in the appropriate solvents (*i.e.*, C_6D_{12}, $CDCl_3$, CD_3CN, and [D6]DMSO) in standard 5 mm glass tubes. A direct observation probe was employed, and the probe temperature was set to 298.1 K. The 90° observation pulses were previously calibrated and had typical durations of 11.75 μs.

Computational Details

The energy profile of rotation around the $\varphi_{C–N–C=O}$ dihedral angle for axial and equatorial conformers of **1** was obtained with a step size of 30° at the MP2/6-311++G(d,p) level. The geometries of the located energy minima of **1** were then optimized using density functional methods, namely the ωB97X-D, B3LYP, and M062X hybrid functionals as well as the B97-D and BLYP functionals with the 6-311++G(d,p) basis set,[15b] in order to determine the appropriate level of theory for the system in study. Dispersion effects were considered by the dispersion corrections proposed by Grimme et al. with the BJ damping function.[17] MP2 was used as the reference method. B3LYP-D3(BJ) was selected because, among the density functionals with the smallest MAE value, it better reproduces the trends in the conformational population compared to MP2 (see Appendix 3.1). Frequency calculations were performed to obtain thermodynamic energies and to ensure that structures converged to true energy minima. The role of solvent effects on this conformational equilibrium was assessed by geometry optimization and frequency calculations in implicit solvents (*i.e.*, cyclohexane, chloroform, acetonitrile, and DMSO) according to the integral equation formalism variant of the Polarizable Continuum Model (IEFPCM).[24] The NBO analysis[20] was used to search for prospective intramolecular interactions influencing conformational energies. All calculations were performed using the previously selected level of theory. Additionally, calculations of the spin–spin coupling constants (also in cyclohexane, chloroform, acetonitrile, and DMSO) using the *gauge including atomic orbital* (GIAO) method[25] with the EPR–III basis set[19] were

performed and compared with experimental NMR spectra in order to estimate the relative conformer population in each media. All abovementioned calculations were carried out using the Gaussian 09 rev. D01 program,[26] and molecular structures were illustrated using CYLview.[27]

3.5 References

[1] a) N. L. Allinger, H. M. Blatter, *J. Org. Chem.* **1962**, *27*, 1523; b) F. Yoshinaga, C. F. Tormena, M. P. Freitas, R. Rittner, R. J. Abraham, *J. Chem. Soc., Perkin Trans. 2* **2002**, *0*, 1494.

[2] a) J. V. Coelho, M. P. Freitas, *THEOCHEM* **2010**, *941*, 53; b) C. F. Tormena, *Prog. Nucl. Magn. Reson. Spectrosc.* **2016**, *96*, 73.

[3] a) L. Hunter, *Beilstein J. Org. Chem.* **2010**, *6*, 1; b) D. O'Hagan, *J. Org. Chem.* **2012**, *77*, 3689.

[4] L. Goodman, H. Gu, V. Pophristic, *J. Phys. Chem. A* **2005**, *109*, 1223.

[5] a) I. V. Alabugin, K. M. Gilmore, P. W. Peterson, *Wiley Interdiscip. Rev.: Comput. Mol. Sci.* **2011**, *1*, 109; b) C. Thiehoff, Y. P. Rey, R. Gilmour, *Isr. J. Chem.* **2017**, *57*, 92.

[6] D. Y. Buissonneaud, T. Van Mourik, D. O'Hagan, *Tetrahedron* **2010**, *66*, 2196.

[7] a) D. O'Hagan, C. Bilton, J. A. K. Howard, L. Knight, D. J. Tozer, *J. Chem. Soc., Perkin Trans. 2* **2000**, *0*, 605; b) C. R. S. Briggs, D. O'Hagan, J. A. K. Howard, D. S. Yufit, *J. Fluorine Chem.* **2003**, *119*, 9.

[8] a) Y. P. Rey, L. E. Zimmer, C. Sparr, E. M. Tanzer, W. B. Schweizer, H. M. Senn, S. Lakhdar, R. Gilmour, *Eur. J. Org. Chem.* **2014**, *2014*, 1202; b) M. Aufiero, R. Gilmour, *Acc. Chem. Res.* **2018**, *51*, 1701.

[9] C. S. Teschers, C. G. Daniliuc, G. Kehr, R. Gilmour, *J. Fluorine Chem.* **2018**, *210*, 1.

[10] S. Paul, W. B. Schweizer, G. Rugg, H. M. Senn, R. Gilmour, *Tetrahedron* **2013**, *69*, 5647.

[11] G. Pattison, *Beilstein J. Org. Chem.* **2017**, *13*, 2915.

[12] J. I. Seeman, *Chem. Rev.* **1983**, *83*, 83.

[13] T. F. B. Silva, L. A. F. Andrade, J. M. Silla, C. J. Duarte, R. Rittner, M. P. Freitas, *J. Phys. Chem. A* **2014**, *118*, 6266.

[14] a) R. Koudih, G. Gilbert, M. Dhilly, A. Abbas, L. Barre, D. Debruyne, F. Sobrio, *Eur. J. Med. Chem.* **2012**, *53*, 408; b) Y. Nakajima, T. Inoue, K. Nakai, K. Mukoyoshi, H. Hamaguchi, K. Hatanaka, H. Sasaki, A. Tanaka, F. Takahashi, S. Kunikawa, H. Usuda, A. Moritomo, Y. Higashi, M. Inami, S. Shirakami, *Bioorg. Med. Chem.* **2015**, *23*, 4871; c) B. Planty, C. Pujol, M. Lamothe, C. Maraval, C. Horn, B. Le Grand, M. Perez, *Bioorg. Med. Chem. Lett.* **2010**, *20*, 1735; d) A. Sun, D. C. Lankin, K. Hardcastle, J. P. Snyder, *Chem. Eur. J.* **2005**, *11*, 1579.

[15] a) M. Head-Gordon, J. A. Pople, M. Frisch, *Chem. Phys. Lett.* **1988**, *153*, 503; b) R. Krishnan, J. S. Binkley, R. Seeger, J. A. Pople, *J. Chem. Phys.* **1980**, *72*, 650.

[16] a) A. D. Becke, *Phys. Rev. A* **1988**, *38*, 3098; b) C. Lee, W. Yang, R. G. Parr, *Phys. Rev. B* **1988**, *37*, 785.

[17] S. Grimme, S. Ehrlich, L. Goerigk, *J. Comput. Chem.* **2011**, *32*, 1456.

[18] a) M. Karplus, *J. Chem. Phys.* **1959**, *30*, 11; b) M. Karplus, *J. Phys. Chem.* **1960**, *64*, 1793; c) M. Karplus, *J. Am. Chem. Soc.* **1963**, *85*, 2870.

[19] V. Barone, in Recent *Adv.* Density *Funct. Methods*, Part I (Ed.: D. P. Chong), World Scientific Publ. Co., Singapore, **1996**.

[20] a) E. D. Glendening, J. K. Badenhoop, A. E. Reed, J. E. Carpenter, J. A. Bohmann, C. M. Morales, C. R. Landis, F. Weinhold, *NBO 6.0*. Theoretical Chemistry Institute, University of Wisconsin, Madison, **2013**; b) E. D. Glendening, C. R. Landis, F. Weinhold, *J. Comput. Chem.* **2013**, *34*, 1429.

[21] F. Weinhold, C. R. Landis, E. D. Glendening, *Int. Rev. Phys. Chem.* **2016**, *35*, 399.

[22] F. A. Martins, J. M. Silla, M. P. Freitas, *Beilstein J. Org. Chem.* **2017**, *13*, 1781.

[23] J. M. Silla, W. G. D. P. Silva, R. A. Cormanich, R. Rittner, C. F. Tormena, M. P. Freitas, *J. Phys. Chem. A* **2014**, *118*, 503.

[24] J. Tomasi, B. Mennucci, R. Cammi, *Chem. Rev.* **2005**, *105*, 2999.

[25] a) K. Wolinski, J. F. Hinton, P. Pulay, *J. Am. Chem. Soc.* **1990**, *112*, 8251; b) R. Ditchfield, *J. Chem. Phys.* **1972**, *56*, 5688.

[26] M. J. Frisch, G. W. Trucks, H. B. Schlegel, G. E. Scuseria, M. A. Robb, J. R. Cheeseman, G. Scalmani, V. Barone, B. Mennucci, G. A. Petersson, H. Nakatsuji, M. Caricato, X. Li, H. P. Hratchian, A. F. Izmaylov, J. Bloino, G. Zheng, J. L. Sonnenberg, M. Hada, M. Ehara, K. Toyota, R. Fukuda, J. Hasegawa, M. Ishida, T. Nakajima, Y. Honda, O. Kitao, H. Nakai, T. Vreven, J. A. Montgomery Jr., J. E. Peralta, F. Ogliaro, M. Bearpark, J. J. Heyd, E. Brothers, K. N. Kudin, V. N. Staroverov, R. Kobayashi, J. Normand, K. Raghavachari, A. Rendell, J. C. Burant, S. S. Iyengar, J. Tomasi, M. Cossi, N. Rega, J. M. Millam, M. Klene, J. E. Knox, J. B. Cross, V. Bakken, C. Adamo, J. Jaramillo, R. Gomperts, R. E. Stratmann, O. Yazyev, A. J. Austin, R. Cammi, C. Pomelli, J. W. Ochterski, R. L. Martin, K. Morokuma, V. G. Zakrzewski, G. A. Voth, P. Salvador, J. J. Dannenberg, S. Dapprich, A. D. Daniels, O. Farkas, J. B. Foresman, J. V. Ortiz, J. Cioslowski, D. J. Fox, *Gaussian 09*, Revision D.01; Gaussian, Inc., Wallingford CT, **2013**.

[27] C. Y. Legault, *CYLview 1.0b*. University of Sherbrooke, Sherbrooke, **2009**.

3.6 Appendices

Appendix 3.1: Gas phase relative energies (ΔE and ΔG, the electronic and the Gibbs free energies, respectively) referenced to the global energy minimum (in kcal mol^{-1}), Boltzmann populations (in %, according to the standard Gibbs free energy) and the mean absolute error (MAE, relative to the MP2 energies) using different density functional approaches for the four conformers of the 1-Boc-3-fluoro-4-oxopiperidine (**1**).

	MP2			**ωB97X-D**			**B3LYP**			**M06-2X**		
	ΔE	ΔG	Pop	ΔE	ΔG	Pop	ΔE	ΔG	Pop	ΔE	ΔG	Pop
$\mathbf{1}_{ax}^{syn}$	0.88	0.57	17	0.66	0.80	12	0.36	0.36	18	0.89	0.67	14
$\mathbf{1}_{ax}^{anti}$	0.00	0.00	45	0.00	0.00	48	0.00	0.12	26	0.00	0.34	25
$\mathbf{1}_{eq}^{syn}$	0.94	0.62	16	0.57	0.24	32	0.35	0.19	24	0.87	0.63	15
$\mathbf{1}_{eq}^{anti}$	0.75	0.43	22	0.24	1.05	8	0.15	0.00	32	0.63	0.00	45
	MAE			0.28	0.31		0.43	0.30		0.05	0.22	
	BLYP			**B97D**			**B3LYP-D3(BJ)**			**BLYP-D3(BJ)**		
	ΔE	ΔG	Pop	ΔE	ΔG	Pop	ΔE	ΔG	Pop	ΔE	ΔG	Pop
$\mathbf{1}_{ax}^{syn}$	0.34	0.18	21	0.78	0.42	17	0.60	0.38	21	0.58	0.28	25
$\mathbf{1}_{ax}^{anti}$	0.00	0.02	28	0.00	0.00	35	0.00	0.00	39	0.00	0.00	40
$\mathbf{1}_{eq}^{syn}$	0.42	0.13	23	0.73	0.43	17	0.63	0.55	16	0.66	0.61	14
$\mathbf{1}_{eq}^{anti}$	0.21	0.00	29	0.48	0.08	31	0.41	0.27	25	0.44	0.36	22
	0.40	0.33		0.15	0.17		0.23	0.11		0.22	0.09	

Appendix 3.2: Molecular dipole moment (μ, in D), relative conformational energies (ΔE and ΔG, in kcal mol^{-1}) referenced to the global energy minimum, and populations (in %, according to the standard Gibbs free energy) for the conformers of **1** in gas phase and in implicit solvents at the B3LYP-D3(BJ)/6-311++G(d,p) level of theory.

	Gas phase				**Cyclohexane**				**Chloroform**			
	μ	ΔE	ΔG	Pop	μ	ΔE	ΔG	Pop	μ	ΔE	ΔG	Pop
$\mathbf{1}_{ax}^{syn}$	3.27	0.60	0.38	21	3.66	0.65	0.38	16	4.04	1.02	0.53	14
$\mathbf{1}_{ax}^{anti}$	2.63	0.00	0.00	39	2.94	0.18	0.12	25	3.25	0.72	0.47	16
$\mathbf{1}_{eq}^{syn}$	5.42	0.63	0.55	16	6.01	0.18	0.03	29	6.51	0.12	0.00	36
$\mathbf{1}_{eq}^{anti}$	3.74	0.41	0.27	25	4.08	0.00	0.00	30	4.33	0.00	0.03	34
	Acetonitrile				**DMSO**							
	μ	ΔE	ΔG	Pop	μ	ΔE	ΔG	Pop				
$\mathbf{1}_{ax}^{syn}$	4.46	1.31	0.86	10	4.49	1.32	0.88	10				
$\mathbf{1}_{ax}^{anti}$	3.57	1.20	1.17	6	3.59	1.22	1.20	6				
$\mathbf{1}_{eq}^{syn}$	6.96	0.03	0.06	40	6.98	0.03	0.07	39				
$\mathbf{1}_{eq}^{anti}$	4.53	0.00	0.00	44	4.54	0.00	0.00	46				

Appendix 3.3: Molecular dipole moment (μ, in D), relative conformational energies (kcal mol^{-1}) referenced to the global energy minimum and populations (%, according to the standard Gibbs free energy) for the 2-halocyclohexanone analogs.

	μ	Δ*G*	Pop	Δ*E*	ΔE_{NL}	ΔE_{L}	ΔE_{DISP}
$\mathbf{1}_{ax}^{syn}$	3.27	0.38	21	0.60	–1.46	1.74	0.33
$\mathbf{1}_{ax}^{anti}$	2.63	0.00	39	0.00	0.00	0.00	0.00
$\mathbf{1}_{eq}^{syn}$	5.42	0.55	16	0.63	–6.52	6.87	0.28
$\mathbf{1}_{eq}^{anti}$	3.74	0.27	25	0.41	–6.18	6.33	0.26
$\mathbf{1'}_{ax}^{syn}$	3.51	0.01	44	0.86	–0.60	0.80	0.66
$\mathbf{1'}_{ax}^{anti}$	2.80	0.00	45	0.00	0.00	0.00	0.00
$\mathbf{1'}_{eq}^{syn}$	5.36	1.25	5	1.87	–0.94	1.42	1.39
$\mathbf{1'}_{eq}^{anti}$	3.61	1.14	7	1.54	–0.11	0.39	1.26
$\mathbf{1''}_{ax}^{syn}$	3.55	0.41	28	0.82	–0.19	0.18	0.83
$\mathbf{1''}_{ax}^{anti}$	2.84	0.00	57	0.00	0.00	0.00	0.00
$\mathbf{1''}_{eq}^{syn}$	5.28	1.64	4	2.38	2.23	–1.63	1.78
$\mathbf{1''}_{eq}^{anti}$	3.52	0.98	11	2.03	2.83	–2.46	1.67
$\mathbf{2}_{ax}^{syn}$	2.99	0.38	20	0.42	–1.60	1.85	0.17
$\mathbf{2}_{ax}^{anti}$	2.43	0.00	38	0.00	0.00	0.00	0.00
$\mathbf{2}_{eq}^{syn}$	4.92	0.43	18	0.51	–6.78	7.10	0.20
$\mathbf{2}_{eq}^{anti}$	3.16	0.27	24	0.36	–6.60	6.77	0.19
$\mathbf{3}_{ax}^{syn}$	3.19	0.63	17	0.62	–3.17	3.63	0.16
$\mathbf{3}_{ax}^{anti}$	2.72	0.00	50	0.00	0.00	0.00	0.00
$\mathbf{3}_{eq}^{syn}$	4.21	0.77	14	0.85	–8.60	9.21	0.25
$\mathbf{3}_{eq}^{anti}$	1.11	0.59	19	0.67	–8.77	9.18	0.26
$\mathbf{3'}_{ax}^{syn}$	5.42	0.45	16	0.44	–1.72	2.05	0.11
$\mathbf{3'}_{ax}^{anti}$	5.11	0.00	33	0.00	0.00	0.00	0.00
$\mathbf{3'}_{eq}^{syn}$	4.89	0.22	23	0.25	0.86	–0.73	0.13
$\mathbf{3'}_{eq}^{anti}$	2.50	0.10	28	0.08	0.83	–0.88	0.13
$\mathbf{4}_{F\text{-}ax}^{H\text{-}ax}$	2.18	0.00	80	0.00	0.00	0.00	0.00
$\mathbf{4}_{F\text{-}ax}^{H\text{-}eq}$	3.59	2.06	2	2.37	1.82	0.33	0.22
$\mathbf{4}_{F\text{-}eq}^{H\text{-}ax}$	4.76	1.21	10	1.36	–2.94	3.99	0.31
$\mathbf{4}_{F\text{-}eq}^{H\text{-}eq}$	4.47	1.38	8	1.57	–7.86	9.25	0.18
$\mathbf{5}_{F\text{-}ax}$	8.07	0.00	100	0.00	0.00	0.00	0.00
$\mathbf{5}_{F\text{-}eq}$	10.45	5.17	0	5.42	–10.81	15.99	0.23

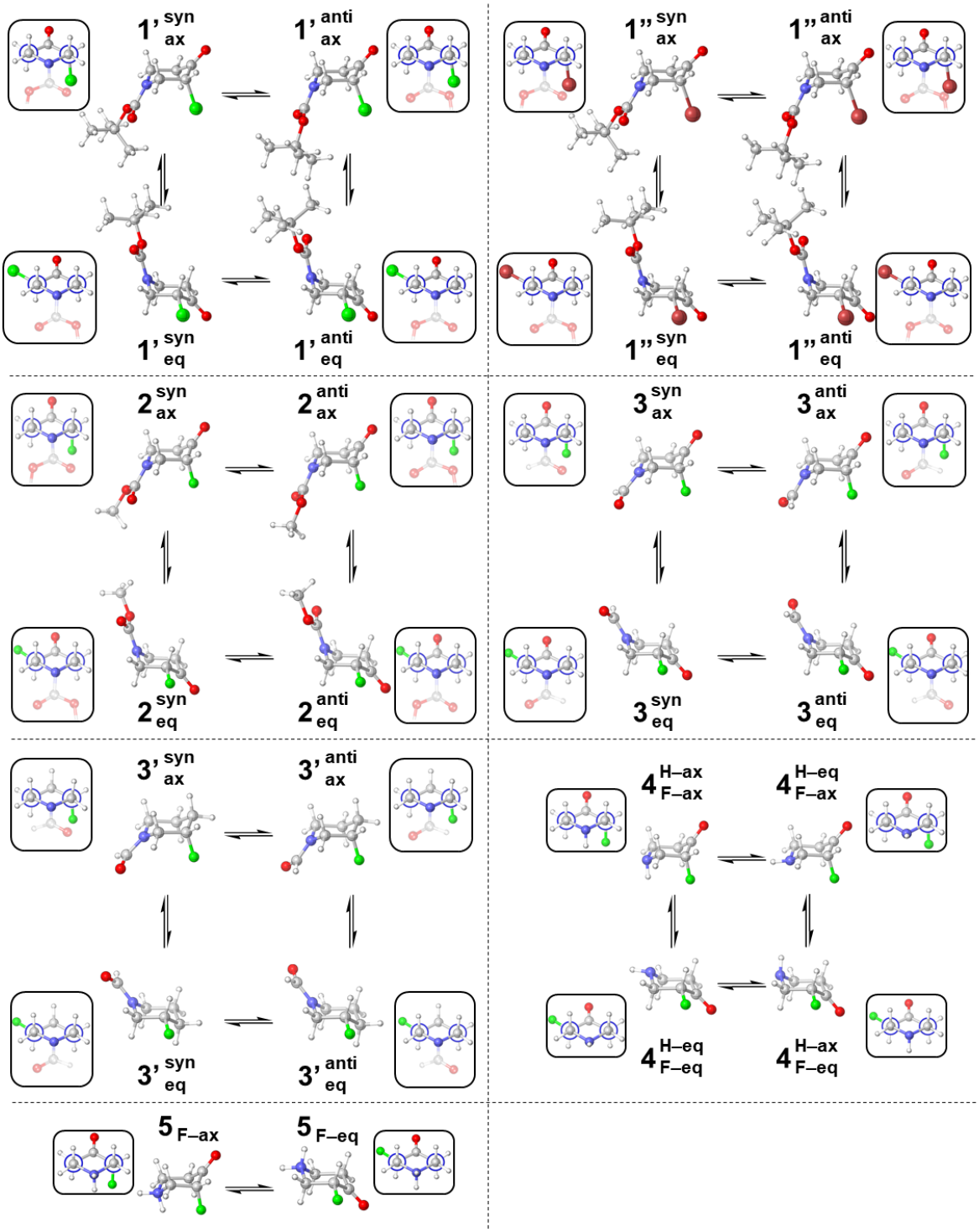

Appendix 3.4: Schematic representation of the conformational equilibrium of the 2-halocyclohexanone analogs studied herein.

Appendix 3.5: Electron delocalization energies (in kcal mol^{-1}) between occupied and unoccupied orbitals from NBO analysis in the gas phase for the conformers of **1**.

Conf.	$\sigma_{CH} \rightarrow \sigma^*_{CN}$	$\sigma_{CH} \rightarrow \sigma^*_{CF}$	$\sigma_{CH} \rightarrow \sigma^*_{CH}$	$\sigma_{CF} \rightarrow \sigma^*_{CN}$	$\sigma_{CN} \rightarrow \sigma^*_{CF}$	$\sigma_{CFax} \rightarrow \pi^*_{CO}$	$n_{Fax} \rightarrow \pi^*_{CO}$	$\sigma_{CHax} \rightarrow \pi^*_{CO}$
$\mathbf{1}^{syn}_{ax}$	2.89	4.56	-	-	-	2.12	1.69	-
$\mathbf{1}^{anti}_{ax}$	2.86	4.56	-	-	-	2.08	1.63	-
$\mathbf{1}^{anti}_{eq}$	-	-	2.38	1.03	1.81	-	-	6.78
$\mathbf{1}^{syn}_{eq}$	-	-	2.31	1.07	1.83	-	-	6.63

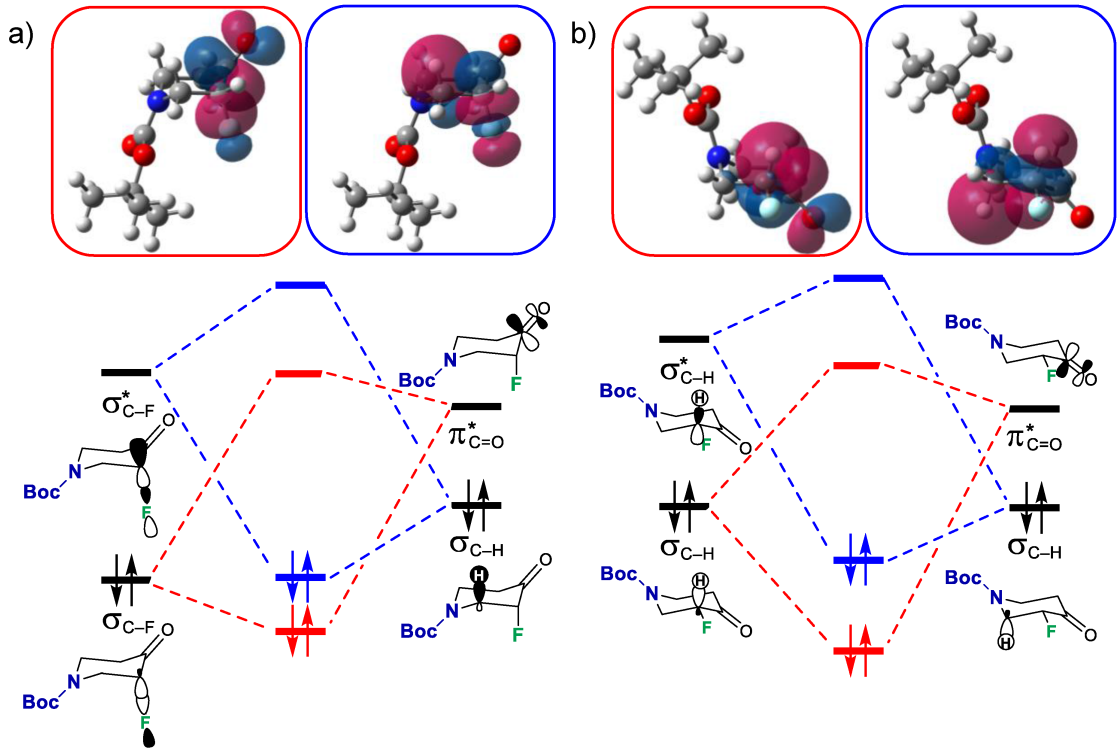

Appendix 3.6: Main orbital interactions in the axial (a, represented by the conformer $\mathbf{1}^{anti}_{ax}$) and equatorial (b, represented by the conformer $\mathbf{1}^{anti}_{eq}$) conformers of **1**. Orbital interaction involving the carbonyl groups in red and the charge transfer featured in the *gauche* effect in blue.

4 PAPER 2 – THE *GAUCHE* EFFECT

Part of this chapter previously appeared as

The Gauche Effect in XCH_2CH_2X Revisited
D. Rodrigues Silva, L. de Azevedo Santos, T. A. Hamlin, C. Fonseca Guerra, M. P. Freitas, F. M. Bickelhaupt
ChemPhysChem **2021**, *22*, 641–648.

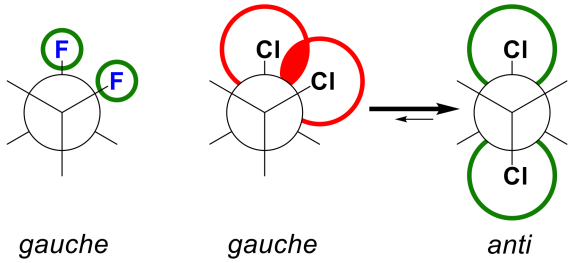

Abstract: We have quantum chemically investigated the rotational isomerism of 1,2-dihaloethanes XCH_2CH_2X (X = F, Cl, Br, I) at ZORA-BP86-D3(BJ)/QZ4P. Our Kohn-Sham molecular orbital (KS-MO) analyses reveal that hyperconjugative orbital interactions favor the *gauche* conformation in all cases (X = F–I), not only for X = F as in the current model of this so-called *gauche* effect. We show that, instead, it is the interplay of hyperconjugation with Pauli repulsion between lone-pair-type orbitals on the halogen substituents that constitutes the causal mechanism for the *gauche* effect. Thus, only in the case of the relatively small fluorine atoms, steric Pauli repulsion is too weak to overrule the *gauche* preference of the hyperconjugative orbital interactions. For the larger halogens, X•••X steric Pauli repulsion becomes sufficiently destabilizing to shift the energetic preference from *gauche* to *anti*, despite the opposite preference of hyperconjugation.

Keywords: Activation strain model, Bond theory, Conformational analysis, Energy decomposition analysis, *Gauche* effect

4.1 Introduction

The energy profile for rotation around the C–C bond in 1,2-disubstituted ethanes features four stationary points, that is, two staggered conformers (*gauche* and *anti*) connected via two eclipsed transition states (*syn* and *anticlinal*), as schematically illustrated in Figure 4.1a.[1] Depending on the nature of the substituted groups, the equilibrium can shift to favor either the *gauche* or the *anti*-conformer.[2] The so-called *gauche* effect, a term coined by Wolfe in 1972,[3] is the phenomenon that the *gauche* conformer is energetically more favorable than the *anti*-conformer in cases where X is an electron-withdrawing group (usually containing atoms from the second period of the periodic table, such as nitrogen, oxygen, or fluorine).[4] The *gauche* effect has been observed in a variety of molecules (especially those containing an organic fluorine)[5] and has been used as a tool for controlling the conformational preference in the design of organic compounds towards specific molecular properties.[6]

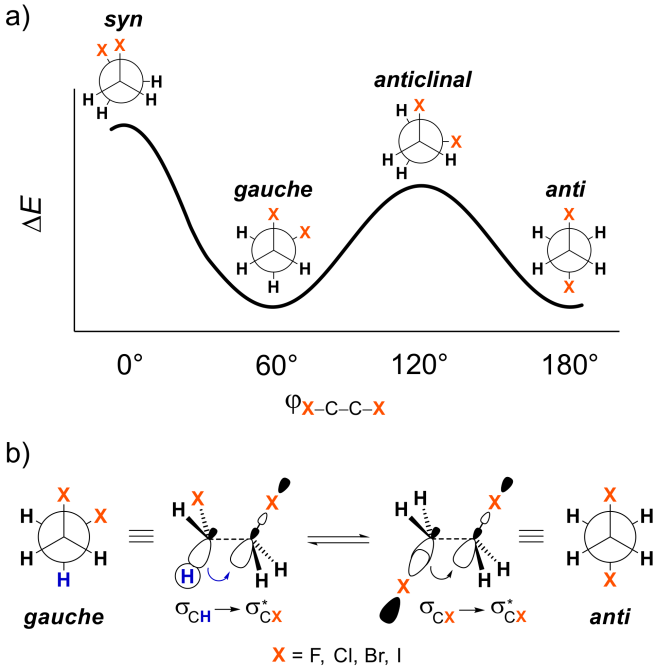

Figure 4.1: a) Stationary points in the energy profile for rotation around the C–C bond of 1,2-dihaloethanes and b) main orbital interactions affecting the *gauche-anti* equilibrium.

In the currently accepted model, the *gauche* effect arises from stabilizing hyperconjugative[7] interactions between antiperiplanar σ orbitals (see Figure 4.1b).[8] This picture was developed to explain experimental evidences on the conformational behavior of the 1,2-difluoroethane,[9] the simplest molecule that exhibits the *gauche* preference.[10] In this hyperconjugation model, the higher stability of the *gauche* conformer is attributed to the

antiperiplanar charge-transfer from the filled σ_{C-H} orbital to the empty σ^*_{C-F} orbital, which is stronger than the corresponding charge-transfer from the filled σ_{C-F} to the empty σ^*_{C-F} in the *anti*-conformer.[8] For heavier halogens, it is argued that this trend should be reversed, because of the better electron-donor and electron-acceptor capabilities of σ_{C-X} and σ^*_{C-X} orbitals as X goes from F to Cl, Br, or I.[11] However, recent reports have shed more light on the role of other forces behind this effect. Baranac-Stojanović[12] pointed out that stabilization of the *gauche* conformer is caused by orbital and also electrostatic interactions, Thacker and Popelier[13] attributed it solely to electrostatics, while Martín-Pendás and coworkers[14] explained it based on both electrostatic and exchange-correlation interactions.[15]

In view of this ongoing and highly relevant controversy, we have investigated the origin of the *gauche* effect within the framework of quantitative Kohn-Sham molecular orbital (KS-MO) theory using the series of 1,2-dihaloethanes $XH_2C–CH_2X$ (X = F, Cl, Br, I, see Figure 4.1). Herein, we show that, at variance to the currently prevailing model, the switch in preference from *gauche* for X = F to *anti* for X = Cl–I, is caused by the increasing steric demand of the substituent X, as the latter descends down a group in the periodic table. This trend does not originate from hyperconjugation, which we show to always favor *gauche* but only overrule steric (Pauli) X•••X repulsion in the *gauche* conformation for the smallest substituent X, in our model systems, the second-row fluorine atom. We also highlight how geometrical relaxation, in particular, the effect of the variation of the C–C bond length, upon internal rotation around this bond can mask the change in the various orbital and electrostatic interactions and needs to be taken into consideration to properly identify causalities.

4.2 Results and Discussion

To understand how the $XH_2C–CH_2X$ bonding mechanism determines conformational preferences, we have analyzed this bond explicitly for all four 1,2-dihaloethanes in terms of two open-shell $CH_2X^\bullet$ fragments forming a C–C electron-pair bond in various conformations. The MO diagram with the valence orbitals of the $CH_2X^\bullet$ fragments is provided in Figure 4.2 (see Appendix 4.1 for more details of $CH_2X^\bullet$ and the better known CH_3X molecular orbitals). The overall bond energy ΔE has been divided into two major components using the activation strain analysis (ASA):[16] the strain (ΔE_{strain}) that results from the distortion of the two $CH_2X^\bullet$ radicals from their equilibrium structure to the geometry they acquire in the $XH_2C–CH_2X$

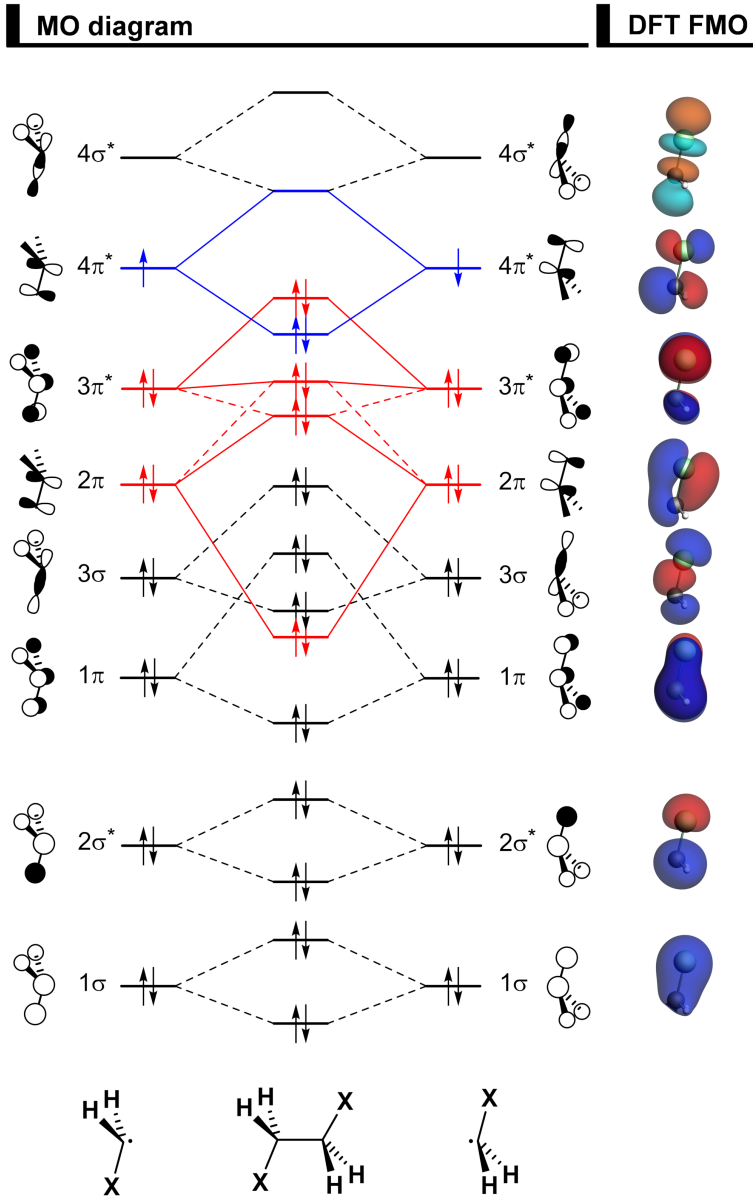

Figure 4.2: MO diagram for the formation of the 1,2-dihaloethanes $XH_2C–CH_2X$ (X = F, Cl, Br, I) from two open-shell $CH_2X^{\bullet}$ fragments, along with the fragment molecular orbitals (FMO) depicted as quantitative 3D plots (isovalue = 0.04) for $CH_2Cl^{\bullet}$, computed at ZORA-BP86-D3(BJ)/QZ4P.

molecule and the actual interaction (ΔE_{int}) between the deformed radical fragments. The interaction energy ΔE_{int} was further decomposed using our canonical energy decomposition analysis for open-shell fragments (EDA)[17] into four energy terms that can be associated with the following physical factors: electrostatic interactions (ΔV_{elstat}), Pauli repulsive orbital interactions (ΔE_{Pauli}) between closed-shell orbitals which is responsible for steric repulsion, stabilizing orbital attractions (ΔE_{oi}) that account, among others, for electron-pair bonding as well as donor-acceptor interactions, and corrections for dispersion interactions (ΔE_{disp}). A theoretical overview of this energy decomposition scheme is given in Chapter 2.5. For the

purpose of clarity, the above-mentioned energy terms along the internal rotation around the C–C bond are considered relative to the *syn* conformation (*i.e.*, represented as a $\Delta\Delta E$), since the latter represents the global energy maximum conformation in all cases. All calculations were performed using ZORA-BP86-D3(BJ)/QZ4P[18] as implemented in the Amsterdam Density Functional (ADF) program,[19] and PyFrag 2019 to facilitate all ASA and EDA analyses.[20]

Our rotational energy profiles of all 1,2-dihaloethanes are given in Figure 4.3. Firstly, we note the well-known energy profile of 1,2-dihaloethanes $XH_2C–CH_2X$,[11] that is, for 1,2-difluoroethane (X = F), the *gauche* conformer is the global energy minimum, whereas the *anti*-conformer is the global energy minimum for all heavier 1,2-dihaloethanes (X = Cl, Br, I). The torsion angle $\varphi_{X–C–C–X}$ (where X = F, Cl, Br, I) of the *gauche* conformer is shifted from 60° to *ca.* 70°, in good agreement with the experimental value of 71.0(3)° for 1,2-difluoroethane (X = F).[21] The C–C bond length directly correlates with conformational stabilities and is shorter in the energy minima and longer in the energy maxima (see Figure 4.3). For example, in 1,2-difluoroethane (X = F), the C–C bond shortens from *syn* (1.556 Å) to *gauche* (1.506 Å), then lengthens going towards the *anticlinal* conformation (1.526 Å) and shortens again at the *anti*-conformer (1.520 Å). Similar, though less pronounced effects are observed for the heavier halogens.

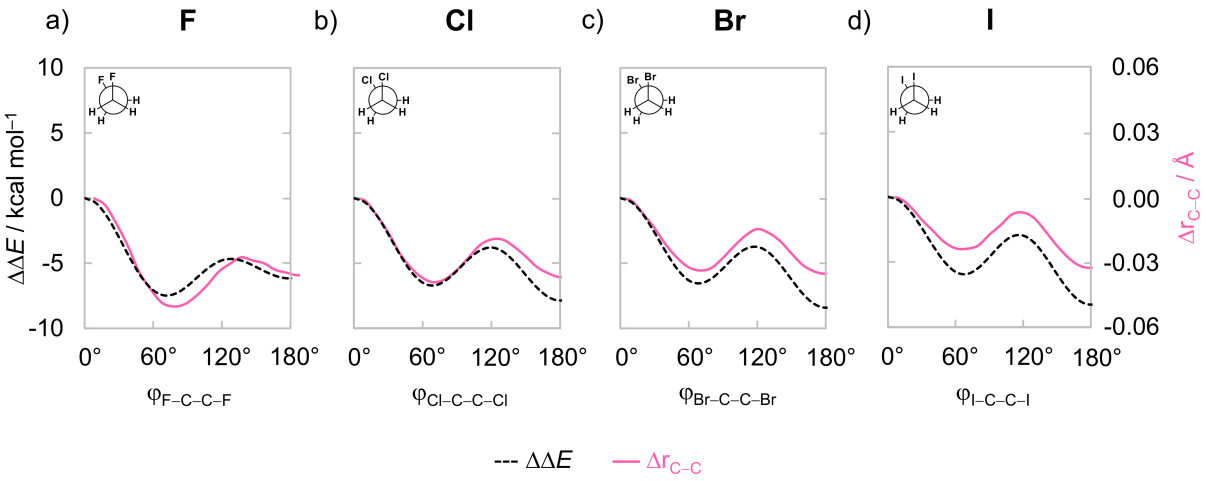

Figure 4.3: Rotational energy profile and C–C bond length variation as a function of the $\varphi_{X–C–C–X}$ dihedral angle of the 1,2-dihaloethanes $XH_2C–CH_2X$ (X = F, Cl, Br, I). Computed at ZORA-BP86-D3(BJ)/QZ4P.

Thus, the variation in C–C bond length along internal rotations is significant (*e.g.*, for 1,2-difluoroethane, it spans 0.05 Å). In the following, we address the question of where this

breathing in C–C bond distance between short in minima and long in maxima comes from, and how it affects the individual interaction mechanisms and their EDA energy terms.

Geometrical Relaxation and Rotational Energy Profile

Our analyses reveal an interesting interplay of effects in which steric Pauli repulsion is the dominant term behind both the raise in energy and the expansion of the C–C bond at eclipsed conformations. The results of these analyses also highlight the importance of separating changes in bonding mechanism, and thus in EDA terms, associated with the internal rotation from further changes in bonding, and thus in EDA terms, due to the further geometrical relaxation (in particular, C–C bond-length variation) that occurs in response to the internal rotation, because this further geometrical relaxation again modifies and thus hides the original causal factors.

Figure 4.4 shows how the different energy components (*i.e.*, Pauli repulsion, electrostatics, and orbital interactions) vary as a function of C–C separation for the *syn* and *gauche* conformations of the 1,2-dihaloethanes. Note that, in a fully relaxed rotation around the C–C bond, not only the C–C bond length changes, but also the geometry of the $CH_2X^\bullet$ fragments which becomes increasingly pyramidalized in the eclipsed conformation to mitigate the buildup of steric Pauli repulsion (*vide infra*). Therefore, to separate the effect of C–C bond length variation from the effect of $CH_2X^\bullet$ bending, we first focus on the curves with fixed $CH_2X^\bullet$ geometry as in the *gauche* conformer CH_2X(g) (solid lines, red for *syn* and black for *gauche*). Note that the upward slope of the ΔE_{Pauli} curve is larger than the downward slopes of the ΔV_{elstat} and ΔE_{oi} curves in all cases, which means that ΔE_{Pauli} changes faster as a function of the C–C distance. Also, the Pauli repulsion is strongest in the *syn* conformation for all distances shown and the gradient of the red line is larger than of the black line, that is, the increase of ΔE_{Pauli} with the shortening of the C–C bond length is greater in the *syn* case (see Appendix 4.2 for the derivative of the different energy terms with respect to the C–C bond length). The larger gradient of the ΔE_{Pauli} curve in the *syn* conformation will drive the molecule towards a longer equilibrium C–C bond length.[22] Therefore, steric Pauli repulsion is the reason why the C–C bond is longer at the *syn* conformation. The picture remains essentially the same if we consider the effect of $CH_2X^\bullet$ bending to the *syn* geometry CH_2X(s) (dotted lines, red for *syn* and black for *gauche*). The magnitude of all energy terms is however smaller since, in its *syn* geometry, $CH_2X^\bullet$ is more bent away from the C–C bond region which reduces the Pauli repulsion (but also other interactions) between the fragments.

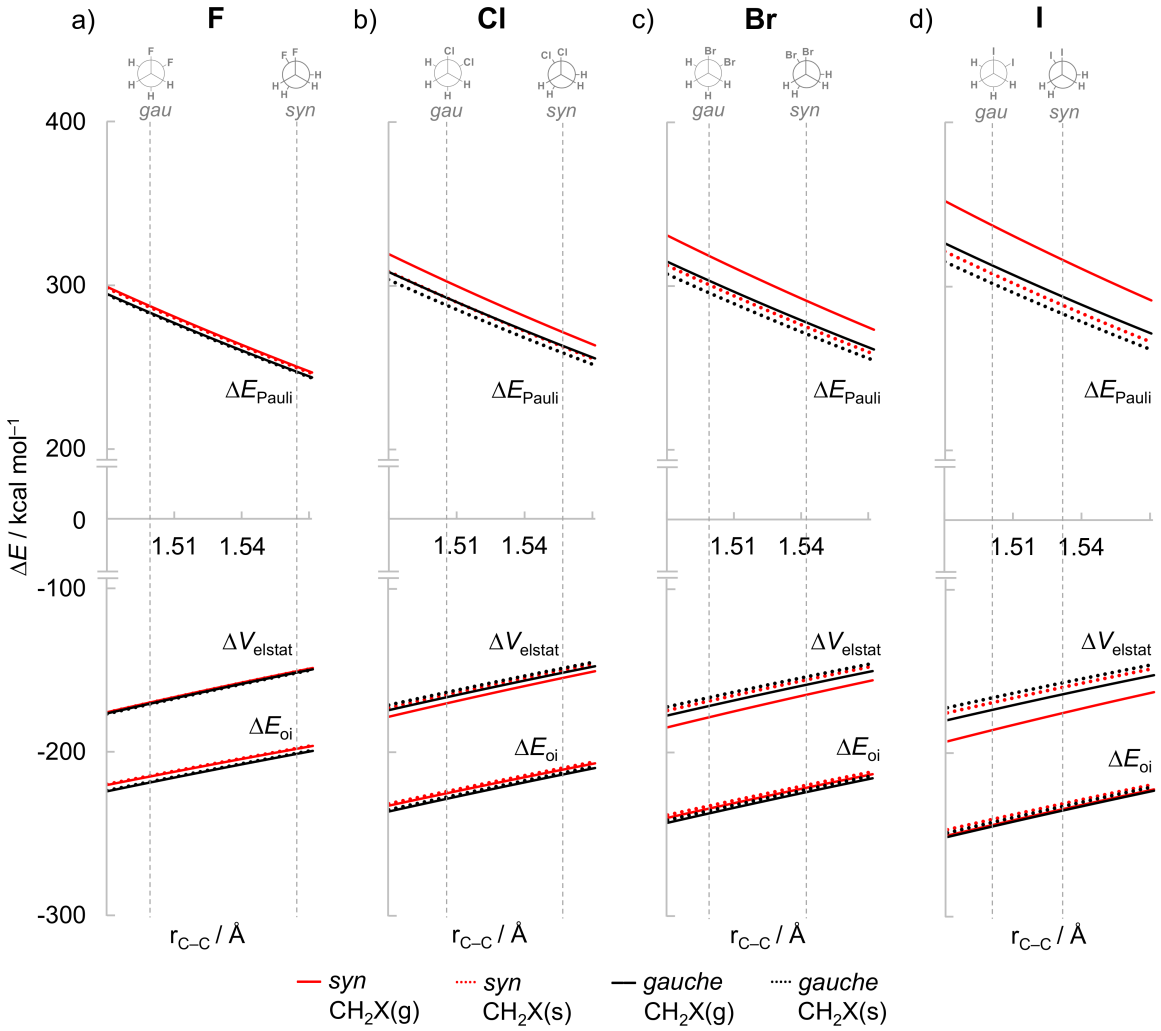

Figure 4.4: EDA of the interaction between two open-shell $CH_2X^{\bullet}$ fragments in 1,2-dihaloethanes $XH_2C–CH_2X$ (X = F, Cl, Br, I) as a function of the C–C separation, computed at ZORA-BP86-D3(BJ)/QZ4P. Vertical dashed lines denote the equilibrium bond distances of the *syn* and *gauche* conformations.

Next, we analyze how geometrical relaxation, in particular, the change in C–C bond length, affects the interpretation of the energy profile for internal rotation around this bond of the 1,2-dihaloethanes. Our results reveal that all energy components are strengthened in the global energy minima because of the shorter C–C bond in these conformations, that is, the observed trends in $\Delta\Delta V_{elstat}$, $\Delta\Delta E_{Pauli}$, and $\Delta\Delta E_{oi}$ are simply a function of the C–C distance.

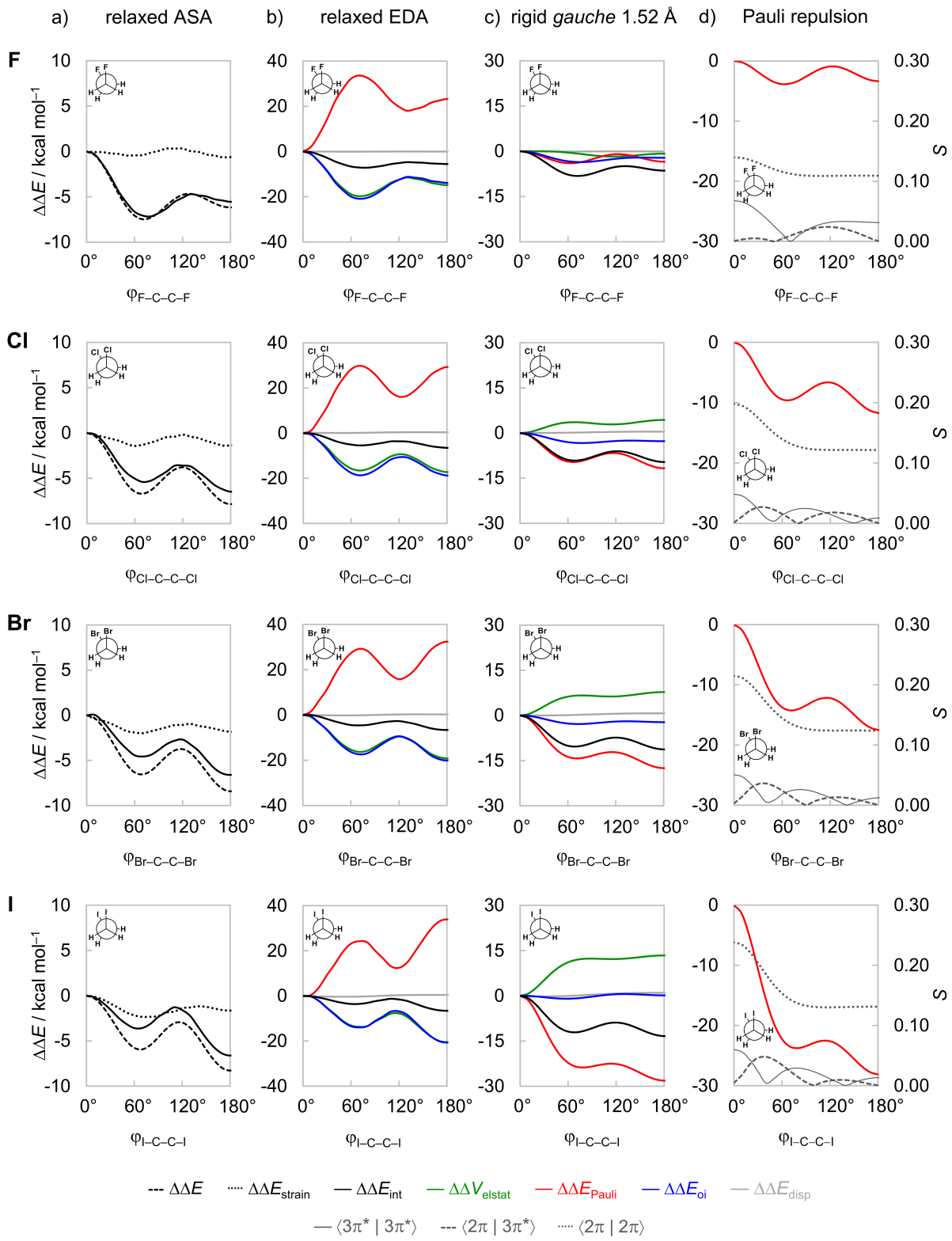

Figure 4.5: Activation strain (ASA) and energy decomposition analyses (EDA) as a function of the $\varphi_{X–C–C–X}$ dihedral angle of the 1,2-dihaloethanes $XH_2C–CH_2X$ (X = F, Cl, Br, I). a) ASA and b) EDA for fully relaxed rotation, c) EDA and d) key closed-shell–closed-shell overlaps for rigid rotation with $CH_2X^{\bullet}$ fragments in *gauche* geometry but with C–C distance set to 1.52 Å. Computed at ZORA-BP86-D3(BJ)/QZ4P.

Thus, care should be exercised when analyzing relaxed rotational barriers (*i.e.*, when all geometrical parameters are flexible to optimize during rotation). The key to understand the trends in the interacting terms is to first take a closer look at the fully relaxed rotation around the C–C bond. As can be seen from Figure 4.5a, the $\Delta\Delta E$ originates primarily from a more stabilizing $\Delta\Delta E_{int}$ that favors the *gauche* conformer for X = F and the *anti*-conformer for X = Cl, Br, I. The $\Delta\Delta E_{strain}$, stemming from the bending of the $CH_2X^{\bullet}$ fragments, is much smaller and more uniform along the rotation of the C–C bond. Since the interaction energy plays such a critical role in the observed trends, the different contributors to the interaction energy were analyzed in more detail using our EDA.[17] Figure 4.5b shows that, in all cases, the trends in the interaction energy are equally dictated by the stabilizing orbital and electrostatic interactions (the $\Delta\Delta E_{oi}$ and $\Delta\Delta V_{elstat}$ curves nearly coincide in all points of the rotation around the C–C bond). On first glance, these findings are, indeed, in line with a previous report that attributed the *gauche* effect to both orbital and electrostatic stabilization.[12] However, owing in particular to the C–C bond lengthening (which is caused by a higher steric Pauli repulsion at any given C–C distance, *vide supra*), the $\Delta\Delta E_{Pauli}$ term is lowest along this curve in the *syn* conformation. This observation is counterintuitive, as already shown in Figure 4.4 and stressed in the analysis of the rotation barrier of ethane,[22] in that the steric repulsion is least destabilizing in the eclipsed conformation where the two C–X bonds are pointing in the same direction and the halogen lone-pairs on each fragment are in closest proximity (see 2π and $3\pi^*$ orbitals in Figure 4.2). The trends observed in Figure 4.5b are dominated by consequence of the C–C bond shortening and stretching, that is, all energy terms are maximized when the C–C bond is shorter (*i.e.*, in the staggered conformers, $\Delta\Delta E_{oi}$ and $\Delta\Delta V_{elstat}$ are more stabilizing, and $\Delta\Delta E_{Pauli}$ is more destabilizing) whereas the opposite occurs when the C–C bond is longer (*i.e.*, in eclipsed conformers; see Figures 4.3 and 4.5b). Figure 4.6 confirms that the changes in the C–C bond length (Δr_{C-C}) correlate with both $\Delta\Delta E_{Pauli}$ and $\Delta\Delta E_{oi}$ terms.

Therefore, to obtain an unbiased picture, it is necessary to perform a numerical experiment in which the strong effect of C–C bond length variation on the energy terms has been eliminated. This can be achieved by performing a rigid rotation around the C–C bond while all geometry parameters but the torsion angle $\varphi_{X-C-C-X}$ are kept unchanged. To this end, let us take the *gauche* conformer of each 1,2-dihaloethane at its optimum geometry and rotate it from the *syn* to the *anti*-conformation. To compare all molecules on a more equal footing, we rotate all 1,2-dihaloethanes from the same C–C bond distance set to 1.52 Å (as in the staggered geometry with the longest C–C bond length, *i.e.*, the *anti*-conformer of the 1,2-difluoroethane; see Figure 4.5c). Note that the conformational preferences in the $\Delta\Delta E_{int}$ curve shown in Figure

4.5c remain the same as in the fully relaxed rotational profiles, that is, $\Delta\Delta E_{int}$ favors *gauche* for X = F and *anti* for X = Cl, Br, and I. The $\Delta\Delta E_{Pauli}$ is a minimum at the staggered conformations and goes to a maximum at the eclipsed conformations, as would be expected. Note that the other energy components have a smaller contribution to the trends in $\Delta\Delta E_{int}$. The $\Delta\Delta V_{elstat}$ term is more stabilizing at the eclipsed conformations (see ref. [22] for a detailed discussion on the behavior of $\Delta\Delta V_{elstat}$ in rotation barriers), the $\Delta\Delta E_{oi}$ only slightly changes, and the $\Delta\Delta E_{disp}$ is nearly constant upon rotation around the C–C bond. The same overall trend is found if we rotate all 1,2-dihaloethanes from their optimum *gauche* or *anti* (Appendix 4.3) as well as *syn* geometries (Appendix 4.4). Note that the strain energy ΔE_{strain} vanishes in this analysis because it is constant for geometrically frozen fragments; therefore, $\Delta\Delta E_{strain}$ is zero and $\Delta\Delta E_{int} = \Delta\Delta E$.

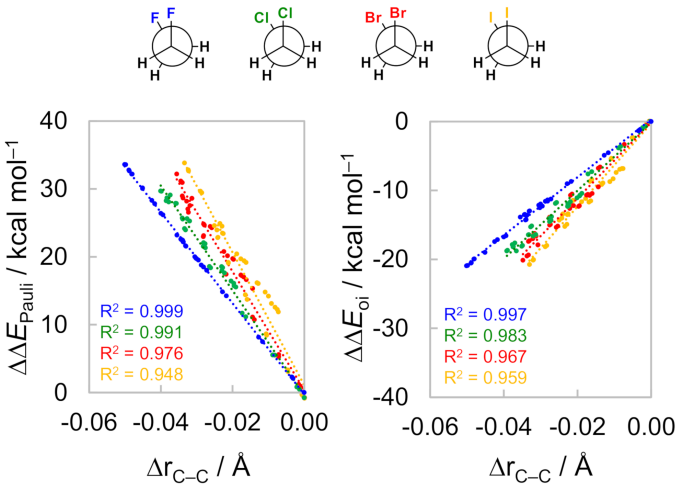

Figure 4.6: Correlation between the C–C bond stretching with steric Pauli repulsion and orbital interactions during rotation around the C–C bond. Computed at ZORA-BP86-D3(BJ)/QZ4P.

The smallest $\Delta\Delta E_{Pauli}$ for *syn* observed in the flexible rotation (Figure 4.5b) is, therefore, a result of the elongation of the C–C bond and the bending of the $CH_2X^{\bullet}$ fragments, that reduces the overlap between the orbitals of the vicinal C–X bonds. Note, for example, that the rigid rotation from the equilibrium *gauche* conformer of the 1,2-difluoroethane to the *syn* orientation leads to 4.0 kcal mol^{-1} more Pauli repulsion (Figure 4.7). Then, when we keep the molecule in the *syn* conformation but relax the other geometry parameters, the Pauli repulsion lowers almost 40 kcal mol^{-1}, much more than the initial rise of 4.0 kcal mol^{-1}. Similar effects can be observed for other 1,2-dihaloethanes (see Appendix 4.4 for the connection of each EDA term between a staggered and an eclipsed rigid rotation of all 1,2-dihaloethanes). This highlights that analyses over relaxed rotational barriers, or final equilibrium geometries, only reflect the consequences but not the reason that leads to a given structural preference in the first place. The importance

of taking into account the strong effect of geometrical relaxation in the course of a chemical phenomenon when elucidating the physical factors underlying it has already been nicely pointed out in the literature.[22,23] Therefore, detailed analyses of the rotational profiles of 1,2-dihaloethanes performed herein clearly demonstrate that $\Delta\Delta E_{\text{Pauli}}$ is the dominant, causal term that determines the observed trends in the variation of the C–C bond length and in the overall rotational energy profile.[24]

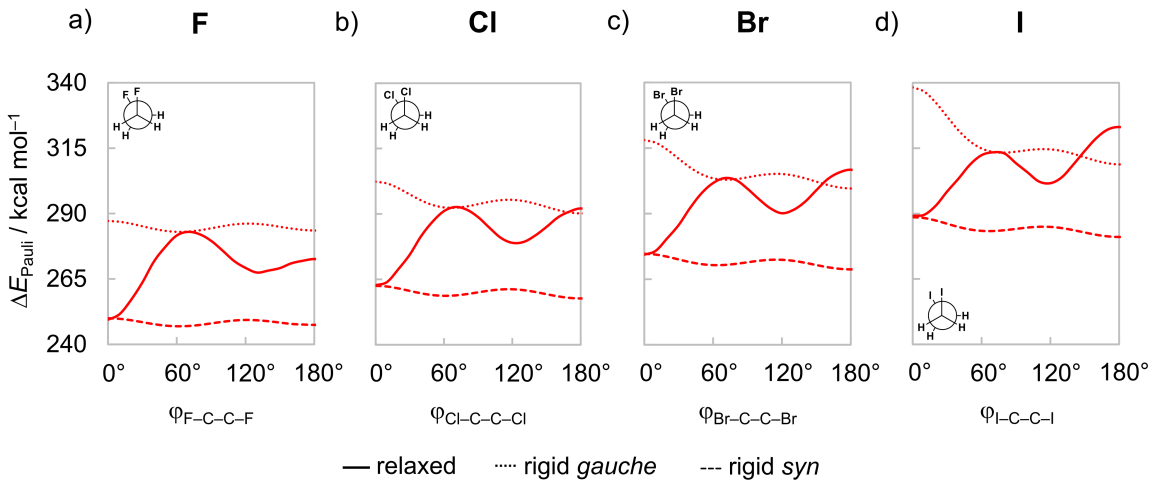

Figure 4.7: Pauli repulsion as a function of the $\varphi_{\text{X–C–C–X}}$ dihedral angle of the 1,2-dihaloethanes $XH_2C–CH_2X$ (X = F, Cl, Br, I). Computed at ZORA-BP86-D3(BJ)/QZ4P.

Steric Pauli Repulsion and the *Gauche* Effect

In the following, we discuss how the above analysis of the rotational energy profiles affects the interpretation of the *gauche* effect observed in the 1,2-difluoroethane. We show that the fluorine atoms in FCH_2CH_2F are too small to cause significant steric Pauli repulsion in the *gauche* conformation and, for this reason, hyperconjugation dominates for X = F.

The most significant closed-shell–closed-shell overlaps between the two $CH_2X^\bullet$ fragments contributing to the trend in $\Delta\Delta E_{\text{Pauli}}$ (shown in Figure 4.5c) arise between the well-known C–X π-bonding and π*-antibonding $CH_2X^\bullet$ FMOs,[25] 2π and 3π*, respectively, each of which possesses both, X lone-pair character as well as carbon 2p amplitude (see Figure 4.8). $\Delta\Delta E_{\text{Pauli}}$ is a maximum at the *syn* because of a larger $\langle 2\pi|2\pi\rangle$ overlap, which decreases as the C–C bond is rotated to the *anti*-conformer (see Figure 4.5d). This effect is more pronounced for heavier halogens because of the larger spatial extension of their valence *n*p atomic orbitals.

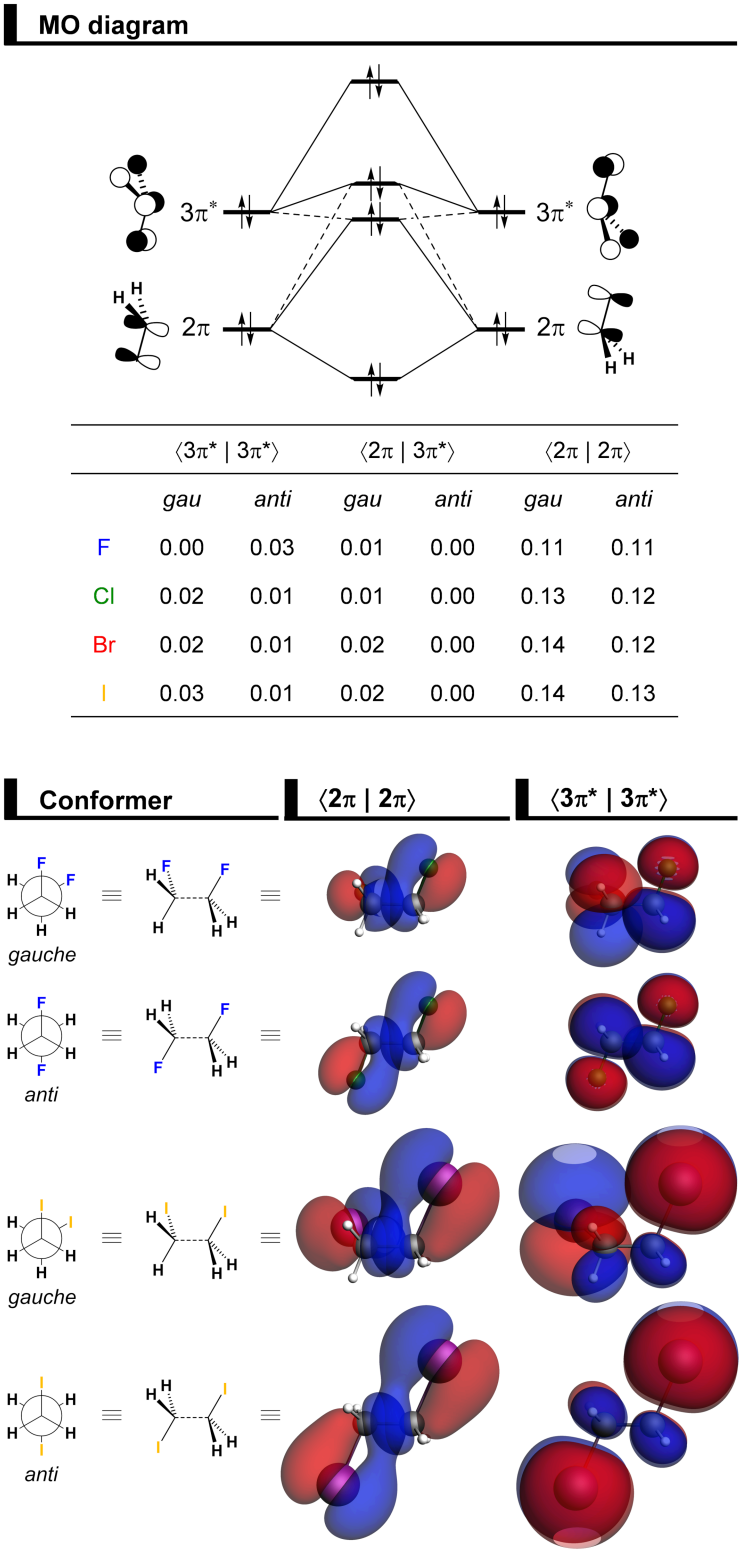

	⟨3π* | 3π*⟩		⟨2π | 3π*⟩		⟨2π | 2π⟩	
	gau	*anti*	*gau*	*anti*	*gau*	*anti*
F	0.00	0.03	0.01	0.00	0.11	0.11
Cl	0.02	0.01	0.01	0.00	0.13	0.12
Br	0.02	0.01	0.02	0.00	0.14	0.12
I	0.03	0.01	0.02	0.00	0.14	0.13

Figure 4.8: MO diagram and the most significant occupied-occupied orbital overlaps between the $CH_2X^{\bullet}$ fragments (where X = F, Cl, Br, I), along with $\langle 2\pi|2\pi\rangle$ (isovalue = 0.04) and $\langle 3\pi^*|3\pi^*\rangle$ (isovalue = 0.02) in the *gauche* and *anti*-conformers of the 1,2-difluoro and 1,2-diiodoethane. Analysis in rigid rotation in *gauche* geometry but with C–C distance set to 1.52 Å, computed at ZORA-BP86-D3(BJ)/QZ4P.

Note that the difference in $\langle 2\pi|2\pi\rangle$ between *gauche* and *anti*-conformers also increases as X goes from F to I. For example, for X = F, the $\langle 2\pi|2\pi\rangle$ is the same in the *gauche* and *anti*, whereas, for X = Cl, Br, and I, it is larger in the *gauche* (see Figure 4.8). A similar behavior is found for the $\langle 2\pi|3\pi^*\rangle$ overlap integral. Thus, the trend in Pauli repulsion determines that the conformational equilibrium gradually shifts to the *anti*-conformer as the halogen increases in size.[11] Interestingly, only for 1,2-difluoroethane, the $\Delta\Delta E_{\text{Pauli}}$ is slightly larger for *anti* than *gauche* (see Appendix 4.5). This can be ascribed to the $\langle 3\pi^*|3\pi^*\rangle$ overlap, in which the amplitude of the $3\pi^*$ orbital is larger on the less electronegative carbon atom because of the out-of-phase mixing of C 2p and F 2p orbitals, resulting in a larger $\langle 3\pi^*|3\pi^*\rangle$ for *anti* than *gauche* (see Figure 4.8). As the atomic p orbital of the halogen atom goes up in energy (and becomes more diffuse) going down group 17 in the periodic table, the amplitude of the $3\pi^*$ orbital increases on the halogen atom and, thus, the $\langle 3\pi^*|3\pi^*\rangle$ overlap is smaller for *anti* than *gauche* for X = Cl, Br, and I. At variance to the heavier and effectively larger halogens, the fluorine orbitals are too compact to cause significant overlap and steric Pauli repulsion and, therefore, cannot shift the conformational equilibrium to *anti*.

The important role played by steric Pauli repulsion is not surprising for heavier 1,2-dihaloethanes (X = Cl, Br, I),[11] but it constitutes an unprecedented physical factor behind the *gauche* effect in 1,2-difluoroethane (X = F).[26] In contrast to the widespread belief that the fluorine atoms would repel each other in the *gauche* conformation, our analysis at the consistent geometries (*i.e.*, all conformations at the same C–C bond length of 1.52 Å) shows that $\Delta\Delta E_{\text{Pauli}}$ slightly favors (by 0.4 kcal mol^{-1}) the *gauche* over the *anti*-conformer for X = F (Figure 4.5d). In this way, any subtle attractive interaction can effectively determine its conformational preference, which is the case of the hyperconjugative interactions used to explain the *gauche* effect in the 1,2-difluoroethane.

The hyperconjugative orbital interactions are more favorable in the *gauche* conformer, in line with the current view of the *gauche* effect.[8] However, this is the case for all 1,2-dihaloethanes analyzed herein, not only for X = F, because the orbital energy gap of the donor–acceptor interaction favoring *gauche* (*i.e.*, $3\pi^* \rightarrow 4\sigma^*$) is smaller than the one favoring *anti* (*i.e.*, $2\pi \rightarrow 4\sigma^*$; see MO diagram in Figure 4.2). Thus, the stabilization due to the $\Delta\Delta E_{\text{oi}}$ results predominantly from a charge-transfer from the occupied $3\pi^*$ orbital of one fragment into the unoccupied $4\sigma^*$ orbital of the other fragment (see Figure 4.9, or Appendix 4.6 for the full data along the rotation of the C–C bond). This is more stabilizing for the 1,2-difluoroethane solely because of the larger orbital overlap ($\langle 3\pi^*|4\sigma^*\rangle$ = 0.15 and 0.02 for X = F and I, respectively).

Again, due to the difference in electronegativity in the C–F bond, the amplitude of both antibonding orbitals, $3\pi^*$ and $4\sigma^*$, is larger on the less electronegative atom, that is, on carbon (see Figure 4.9). Thus, as the difference in electronegativity decreases on going towards heavier halogens, the orbital overlap between the two $CH_2X^\bullet$ fragments also decreases. For the same reason, the orbital energy gap is always bigger when X = F ($\Delta\varepsilon$ = 9.2 eV for X = F and $\Delta\varepsilon$ = 4.6 eV for X = I), that is, it shows a trend opposite to that of $\Delta\Delta E_{oi}$. This is interesting because previously the strength of hyperconjugative interactions in substituted ethanes has been typically attributed to the orbital energies alone.[27] Note that the contribution from the $3\sigma \rightarrow 4\sigma^*$ is less important for the conformational preferences because of a larger orbital energy gap and the associated overlap is similar for *gauche* and *anti* (see Figures 4.2 and Appendix 4.6).

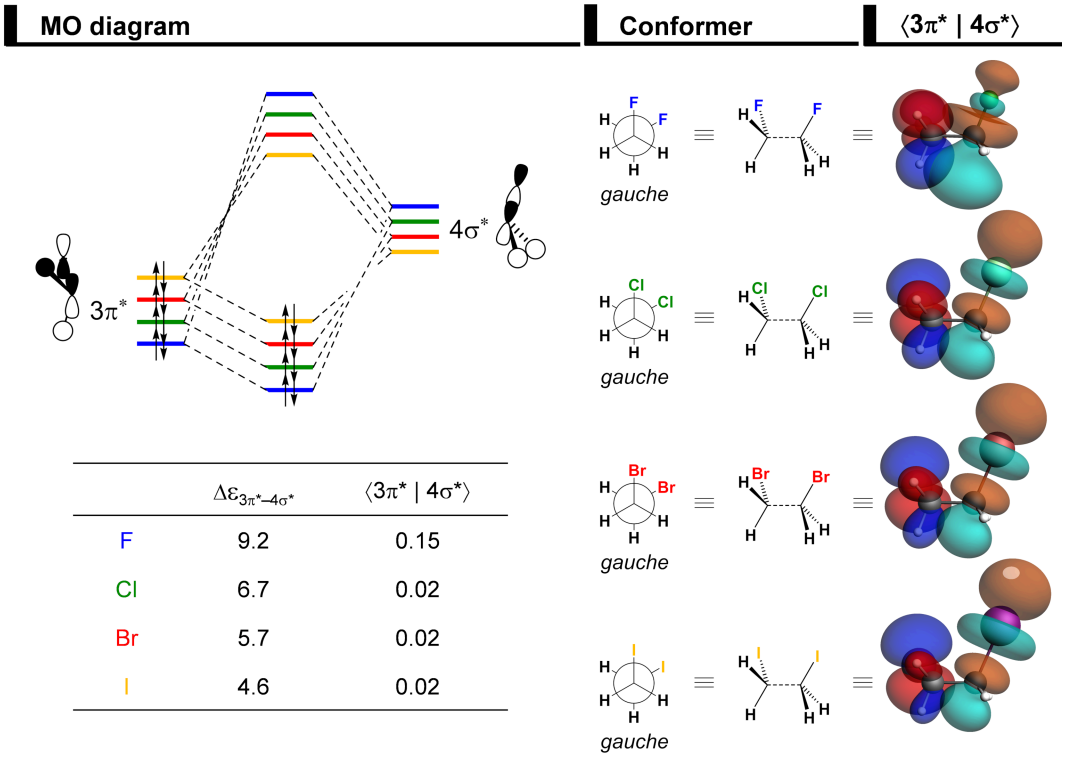

	$\Delta\varepsilon_{3\pi^*-4\sigma^*}$	$\langle 3\pi^* \mid 4\sigma^* \rangle$
F	9.2	0.15
Cl	6.7	0.02
Br	5.7	0.02
I	4.6	0.02

Figure 4.9: MO diagram for the donor-acceptor interaction between the occupied $3\pi^*$ orbital of one fragment and the unoccupied $4\sigma^*$ orbital of the other fragment, along with $3\pi^*$ overlapping with $4\sigma^*$ as 3D plots (isovalue = 0.04) in the *gauche* conformers of the 1,2-dihaloethanes. Analysis in rigid rotation in *gauche* geometry but with C–C distance set to 1.52 Å, computed at ZORA-BP86-D3(BJ)/QZ4P.

The above agrees well with the fact that the orbital interactions have the strongest preference for the *gauche* conformer of 1,2-dihaloethanes in the case of X = F. Nevertheless, the reason that this preference of the orbital interactions for *gauche* can become decisive for X

= F is the very small difference in Pauli repulsion $\Delta\Delta E_{\text{Pauli}}$, in that case, between *gauche* and *anti*-conformers.

4.3 Conclusion

At variance with the current model, the *gauche* effect in 1,2-dihaloethanes (X = F, Cl, Br, I) is not caused by hyperconjugation alone, but also by steric Pauli repulsion between substituents X, as follows from our quantum chemical analysis based on relativistic dispersion-corrected density functional theory. The *gauche* effect refers to the phenomenon that the *gauche* conformer is energetically favored for X = F while, in all other cases (X = Cl, Br, I), the preferred conformer is *anti*. The current model ascribes the *gauche* effect to hyperconjugative orbital interactions that favor *gauche* in case of X = F. Our Kohn-Sham molecular orbital (KS-MO) analyses, however, reveal that such hyperconjugative orbital interactions favor the *gauche* conformation in all cases, not only for X = F but also for X = Cl, Br, and I. The analyses show that it is Pauli repulsion between lone-pair-type orbitals on the halogen substituents that constitutes the causal mechanism for the *gauche* effect. Thus, only in the case of the relatively small fluorine atoms, steric Pauli repulsion is small enough to not overrule the *gauche* preference of the hyperconjugative orbital interactions. For the larger halogens, X•••X steric Pauli repulsion destabilizes the *gauche* conformer and, in this way, shifts the energetic preference from *gauche* to *anti*, despite the inverse preference of hyperconjugation.

4.4 Computational Details

All calculations were performed using the Amsterdam Density Functional (ADF) program 2017.103.[19] Geometry optimization and vibrational analysis of the energy minimum conformations and rotational barrier analysis were carried out using the dispersion-corrected BP86-D3(BJ)[18c-18f] functional in conjunction with the quadruple-ζ quality augmented with polarization functions (two 2*p* and two 3*d* sets on H, two 3*d* and two 4*f* sets on C, F; three 3*d* and two 4*f* sets on Cl, two 4*d* and three 4*f* sets on Br, one 5*d* and three 4*f* sets on I) QZ4P basis set.[18g] The zeroth-order regular approximation (ZORA)[18a,18b] was used to account for scalar relativistic effects. This level is referred to as ZORA-BP86-D3(BJ)/QZ4P. The activation strain and energy decomposition analyses were performed using the PyFrag program at the same level of theory.[20]

4.5 References

[1] E. L. Eliel, S. H. Wilen, L. N. Mander, *Stereochemistry of Organic Compounds*, John Wiley & Sons, Inc., New York, **1994**, pp. 606–615.

[2] See, for instance: a) F. A. Martins, M. P. Freitas, *Eur. J. Org. Chem.* **2019**, *2019*, 6401; b) M. Baranac-Stojanović, J. Aleksić, M. Stojanović, *RSC Adv.* **2015**, *5*, 22980; c) R. A. Cormanich, M. P. Freitas, *J. Org. Chem.* **2009**, *74*, 8384; d) M. P. Freitas, R. Rittner, *J. Phys. Chem. A* **2007**, *111*, 7233.

[3] S. Wolfe, *Acc. Chem. Res.* **1972**, *5*, 102.

[4] a) I. V. Alabugin, K. M. Gilmore, P. W. Peterson, *WIREs Comput. Mol. Sci.* **2011**, *1*, 109; b) I. V. Alabugin, *Stereoelectronic Effects: the Bridge between Structure and Reactivity*, John Wiley & Sons Ltd, Hoboken, **2016**, p. 110.

[5] a) R. A. Cormanich, D. O'Hagan, M. Bühl, *Angew. Chem. Int. Ed.* **2017**, *56*, 7867; *Angew. Chem.* **2017**, *129*, 7975; b) C. Thiehoff, M. C. Holland, C. Daniliuc, K. N. Houk, R. Gilmour, *Chem. Sci.* **2015**, *6*, 3565; c) J. Aleksić, M. Stojanović, M. Baranac-Stojanović, *J. Org. Chem.* **2015**, *80*, 10197; d) L. A. F. Andrade, J. M. Silla, C. J. Duarte, R. Rittner, M. P. Freitas, *Org. Biomol. Chem.* **2013**, *11*, 6766; e) D. O'Hagan, *J. Org. Chem.* **2012**, *77*, 3689; f) D. Y. Buissonneaud, T. van Mourik, D. O'Hagan, *Tetrahedron* **2010**, *66*, 2196.

[6] For application of the *gauche* effect in catalysis, biological systems, and modulation of physical properties, see: a) Y. P. Rey, L. E. Zimmer, C. Sparr, E. M. Tanzer, W. B. Schweizer, H. M. Senn, S. Lakhdar, R. Gilmour, *Eur. J. Org. Chem.* **2014**, *2014*, 1202; b) M. Aufiero, R. Gilmour, *Acc. Chem. Res.* **2018**, *51*, 1701; c) C. S. Teschers, C. G. Daniliuc, G. Kehr, R. Gilmour, *J. Fluorine Chem.* **2018**, *210*, 1; d) P. Bentler, K. Bergander, C. G. Daniliuc, C. Mück-Lichtenfeld, R. P. Jumde, A. K. H. Hirsch, R. Gilmour, *Angew. Chem. Int. Ed.* **2019**, *58*, 10990; *Angew. Chem.* **2019**, *131*, 11106; e) S. Lingier, R. Szpera, B. Goderis, B. Linclau, F. E. Du Prez, *Polymer* **2019**, *164*, 134; f) B. Jeffries, Z. Wang, H. R. Felstead, J.-Y. Le Questel, J. S. Scott, E. Chiarparin, J. Graton, B. Linclau, *J. Med. Chem.* **2020**, *63*, 1002.

[7] The International Union of Pure and Applied Chemistry (IUPAC) Gold Book defines hyperconjugation as the interaction between σ and π bonds. However, the term is used in modern scientific literature to refer to the σ antiperiplanar interactions featured in the *gauche* effect, instead of σ conjugation (see Ref. [4a]). To be in line with other reports regarding the *gauche* effect, we also use the term hyperconjugation model in this work. IUPAC. *Compendium of Chemical Terminology 2nd ed.* (the "Gold Book"), Blackwell Scientific Publications, Oxford, **1997**.

[8] a) L. Goodman, H. Gu, V. Pophristic, *J. Phys. Chem. A* **2005**, *109*, 1223; b) T. K. Brunck, F. Weinhold, *J. Am. Chem. Soc.* **1979**, *101*, 1700; c) L. Radom, W. A. Lathan, W. J. Hehre, J. A. Pople, *J. Am. Chem. Soc.* **1973**, *95*, 693.

[9] For representative experimental studies, see: a) J. R. During, J. Liu, T. S. Little, *J. Phys. Chem.* **1992**, *96*, 8224; b) N. C. Craig, A. Chen, K. H. Suh, S. Klee, G. C. Mellau, B. P. Winnewisser, M. Winnewisser, *J. Am. Chem. Soc.* **1997**, *119*, 4789.

[10] C. Thiehoff, Y. P. Rey, R. Gilmour, *Isr. J. Chem.* **2017**, *57*, 92.

[11] a) F. R. Souza, M. P. Freitas, R. Rittner, *J. Mol. Struct.* **2008**, *863*, 137; b) D. Nori-Shargh, J. E. Boggs, *Struct. Chem.* **2011**, *22*, 253.

[12] M. Baranac-Stojanović, *RSC Adv.* **2014**, *4*, 43834.

[13] J. C. R. Thacker, P. L. A. Popelier, *J. Phys. Chem. A* **2018**, *122*, 1439.

[14] N. Díaz, F. Jiménez-Grávalos, D. Suárez, E. Francisco, A. Martín-Pendás, *Phys. Chem. Chem. Phys.* **2019**, *21*, 25258.

[15] For other theoretical studies on the conformational preferences of 1,2-difluoroethane, see: a) K. B. Wiberg, M. A. Murcko, K. E. Laidig, P. J. MacDougall, *J. Phys. Chem.* **1990**, *94*, 6956; b) K. B. Wiberg, *Acc. Chem. Res.* **1996**, *29*, 229; c) P. R. Rablen, R. W. Hoffmann, D. A. Hrovat, W. T. Borden, *J. Chem. Soc. Perkin Trans. 2* **1999**, 1719, and references cited therein; d) C. Trindle, P. Crum, K. Douglass, *J. Phys. Chem. A* **2003**, *107*, 6236.

[16] a) P. Vermeeren, S. C. C. van der Lubbe, C. Fonseca Guerra, F. M. Bickelhaupt, T. A. Hamlin, *Nat. Protoc.* **2020**, *15*, 649; b) F. M. Bickelhaupt, K. N. Houk, *Angew. Chem. Int. Ed.* **2017**, *56*, 10070; *Angew. Chem.* **2017**, *129*, 10204; c) L. P. Wolters, F. M. Bickelhaupt, *WIREs Comput. Mol. Sci.* **2015**, *5*, 324; d) I. Fernández, F. M. Bickelhaupt, *Chem. Soc. Rev.* **2014**, *43*, 4953; e) W.-J. van Zeist, F. M. Bickelhaupt, *Org. Biomol. Chem.* **2010**, *8*, 3118; f) F. M. Bickelhaupt, *J. Comput. Chem.* **1999**, *20*, 114.

[17] a) F. M. Bickelhaupt, E. J. Baerends, in *Reviews in Computational Chemistry* (Eds.: K. B. Lipkowitz, D. B. Boyd), Wiley, Hoboken, **2000**, pp. 1–86; b) R. van Meer, O. V. Gritsenko, E. J. Baerends, *J. Chem. Theory Comput.* **2014**, *10*, 4432.

[18] a) E. van Lenthe, E. J. Baerends, J. G. Snijders, *J. Chem. Phys.* **1993**, *99*, 4597; b) E. van Lenthe, E. J. Baerends, J. G. Snijders, *J. Chem. Phys.* **1994**, *101*, 9783; c) A. D. Becke, *Phys. Rev. A* **1988**, *38*, 3098; d) J. P. Perdew, *Phys. Rev. B: Condens. Matter Mater. Phys.* **1986**, *33*, 8822; e) S. Grimme, J. Antony, S. Ehrlich, H. Krieg, *J. Chem. Phys.* **2010**, *132*, 154104; f) S. Grimme, S. Ehrlich, L. Goerigk, *J. Comput. Chem.* **2011**, *32*, 1456; g) E. van Lenthe, E. J. Baerends, *J. Comput. Chem.* **2003**, *24*, 1142.

[19] a) G. te Velde, F. M. Bickelhaupt, E. J. Baerends, C. Fonseca Guerra, S. J. A. van Gisbergen, J. G. Snijders, T. Ziegler, *J. Comput. Chem.* **2001**, *22*, 931; b) C. Fonseca Guerra, J. G. Snijders, G.

te Velde, E. J. Baerends, *Theor. Chem. Acc.* **1998**, *99*, 391; c) ADF2017.103, SCM Theoretical Chemistry, Vrije Universiteit Amsterdam (Netherlands), 2010. http://www.scm.com.

[20] a) W. -J. van Zeist, C. Fonseca Guerra, F. M. Bickelhaupt, *J. Comp. Chem.* **2008**, *29*, 312; b) X. Sun, T. M. Soini, J. Poater, T. A. Hamlin, F. M. Bickelhaupt, *J. Comput. Chem.* **2019**, *40*, 2227.

[21] H. Takeo, C. Matsumura, Y. Morino, *J. Chem. Phys.* **1986**, *84*, 4205.

[22] F. M. Bickelhaupt, E. J. Baerends, *Angew. Chem. Int. Ed.* **2003**, *42*, 4183; *Angew. Chem.* **2003**, *115*, 4315.

[23] W. H. E. Schwarz, H. Schmidbaur, *Chem. Eur. J.* **2012**, *18*, 4470.

[24] Steric effects have been found to control other rotation barriers. See, for instance: a) Y. Mo, W. Wu, L. Song, M. Lin, Q. Zhang, J. Gao, *Angew. Chem. Int. Ed.* **2004**, *43*, 1986; *Angew. Chem.* **2004**, *116*, 2020; b) Y. Mo, J. Gao, *Acc. Chem. Res.* **2007**, *40*, 113; c) Z. Chen, C. Corminboeuf, Y. Mo, *J. Phys. Chem. A* **2014**, *118*, 5743.

[25] F. M. Bickelhaupt, T. Ziegler, P. von Ragué Schleyer, *Organometallics* **1996**, *15*, 1477.

[26] a) D. O'Hagan, *Chem. Soc. Rev.* **2008**, *37*, 308; b) L. Hunter, *Beilstein J. Org. Chem.* **2010**, *6*, 1.

[27] I. V. Alabugin, T. A. Zeidan, *J. Am. Chem. Soc.* **2002**, *124*, 3175.

4.6 Appendices

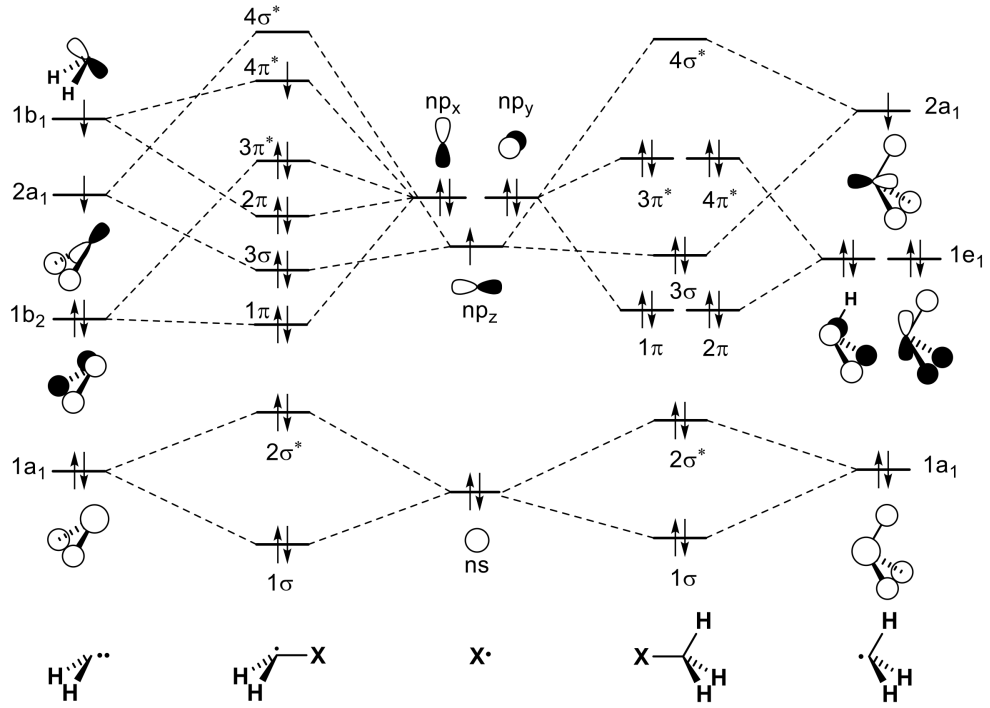

Appendix 4.1: MO diagram for the formation of $H_2C^{\bullet}$–X (left side) and H_3C–X (right side) from $X^{\bullet}$ (= $F^{\bullet}$, $Cl^{\bullet}$, $Br^{\bullet}$, $I^{\bullet}$) interacting with $H_2C^{\bullet\bullet}$ and $H_3C^{\bullet}$, respectively.

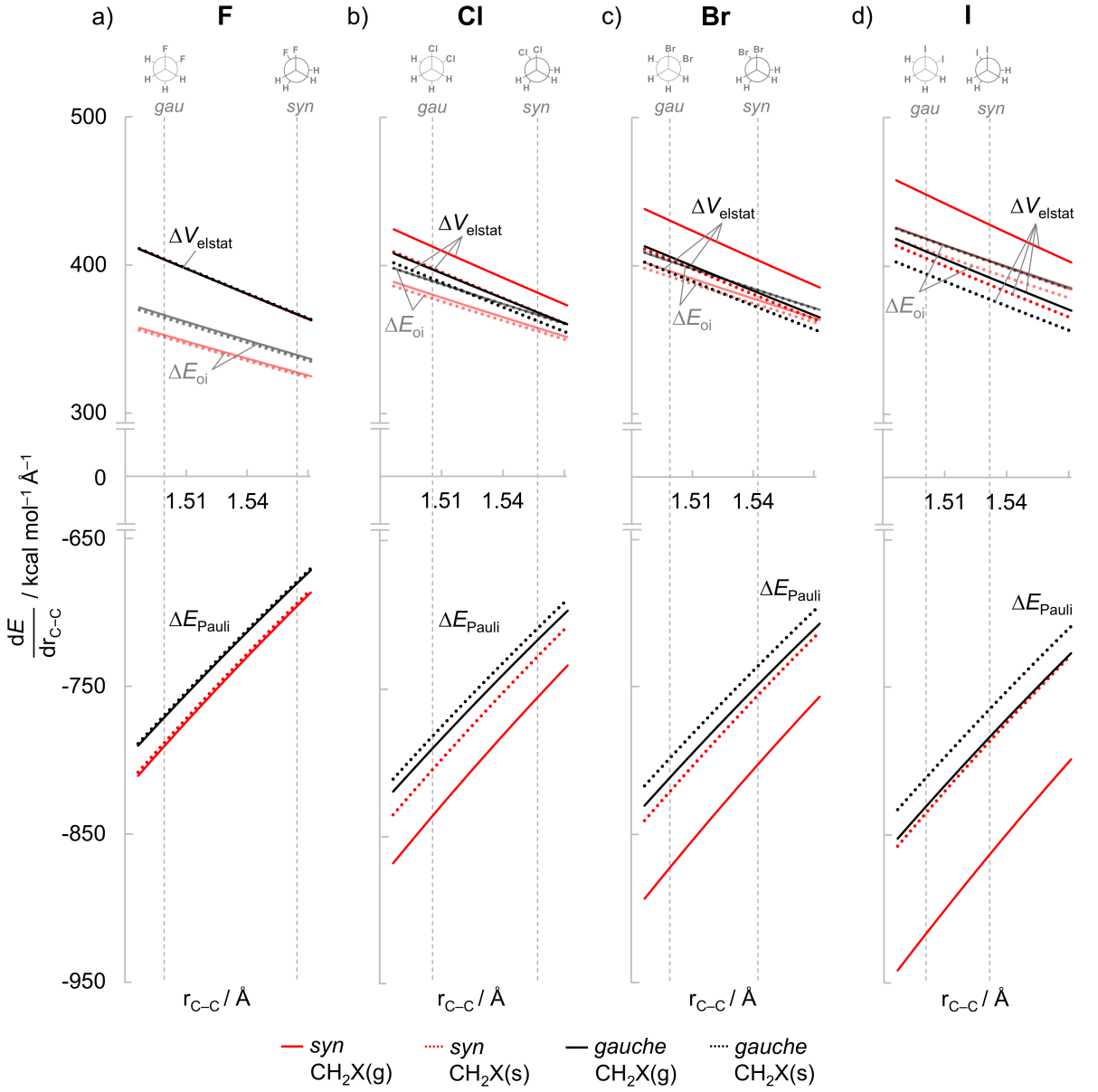

Appendix 4.2: Derivative of the EDA terms with respect to $r_{C–C}$ of the interaction between two open-shell $CH_2X^{\bullet}$ fragments in 1,2-dihaloethanes $XH_2C–CH_2X$ (X = F, Cl, Br, I) as a function of the C–C separation. Computed at ZORA-BP86-D3(BJ)/QZ4P. Vertical dashed lines denote the equilibrium bond distances of the *syn* and *gauche* conformations. Since the ΔV_{elstat} and ΔE_{oi} curves are almost superposing each other in some cases, the orbital interaction curves are slightly transparent for clarity.

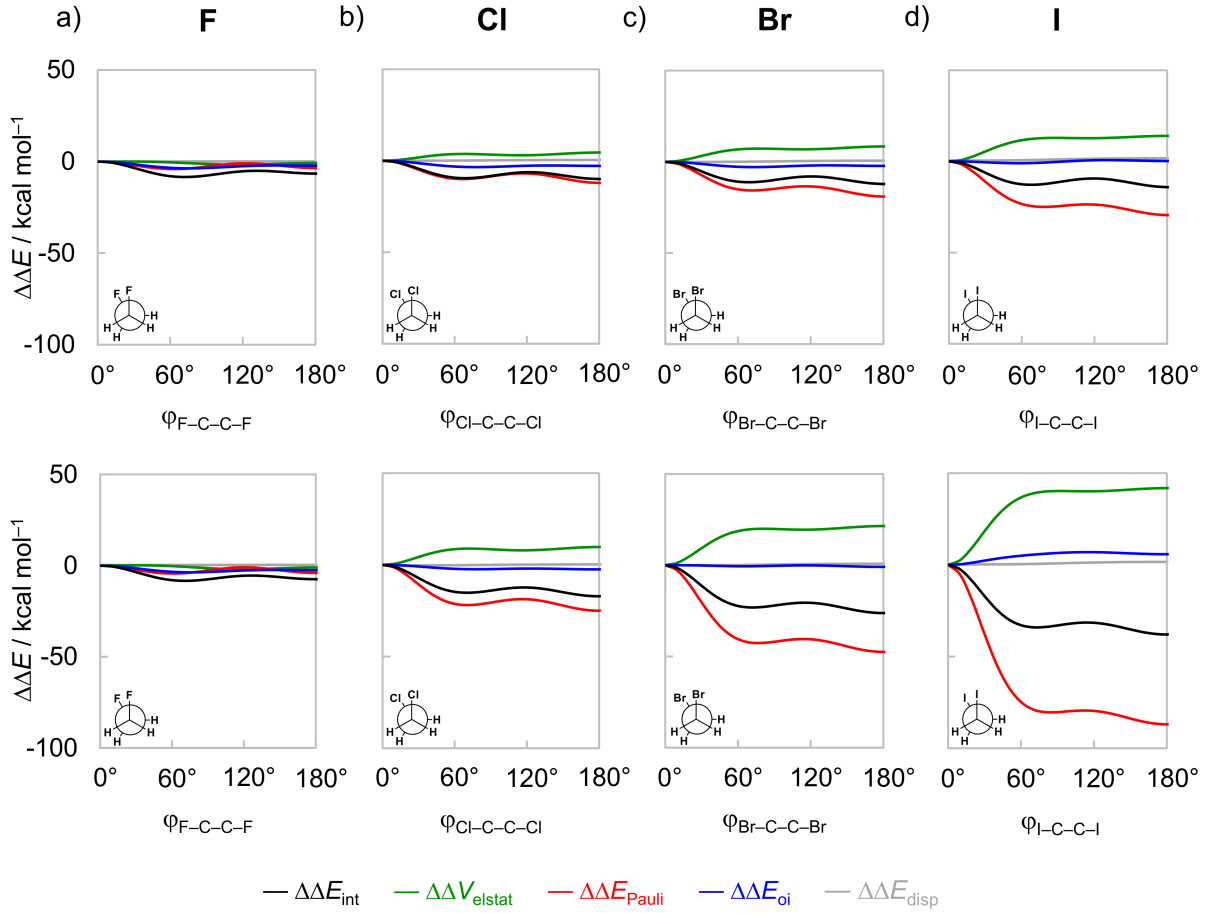

Appendix 4.3: EDA as a function of the $\varphi_{X–C–C–X}$ dihedral angle of the 1,2-dihaloethanes $XH_2C–CH_2X$ (X = F, Cl, Br, I) for rigid rotation in frozen *gauche* (top) and *anti* (bottom) geometries, computed at ZORA-BP86-D3(BJ)/QZ4P.

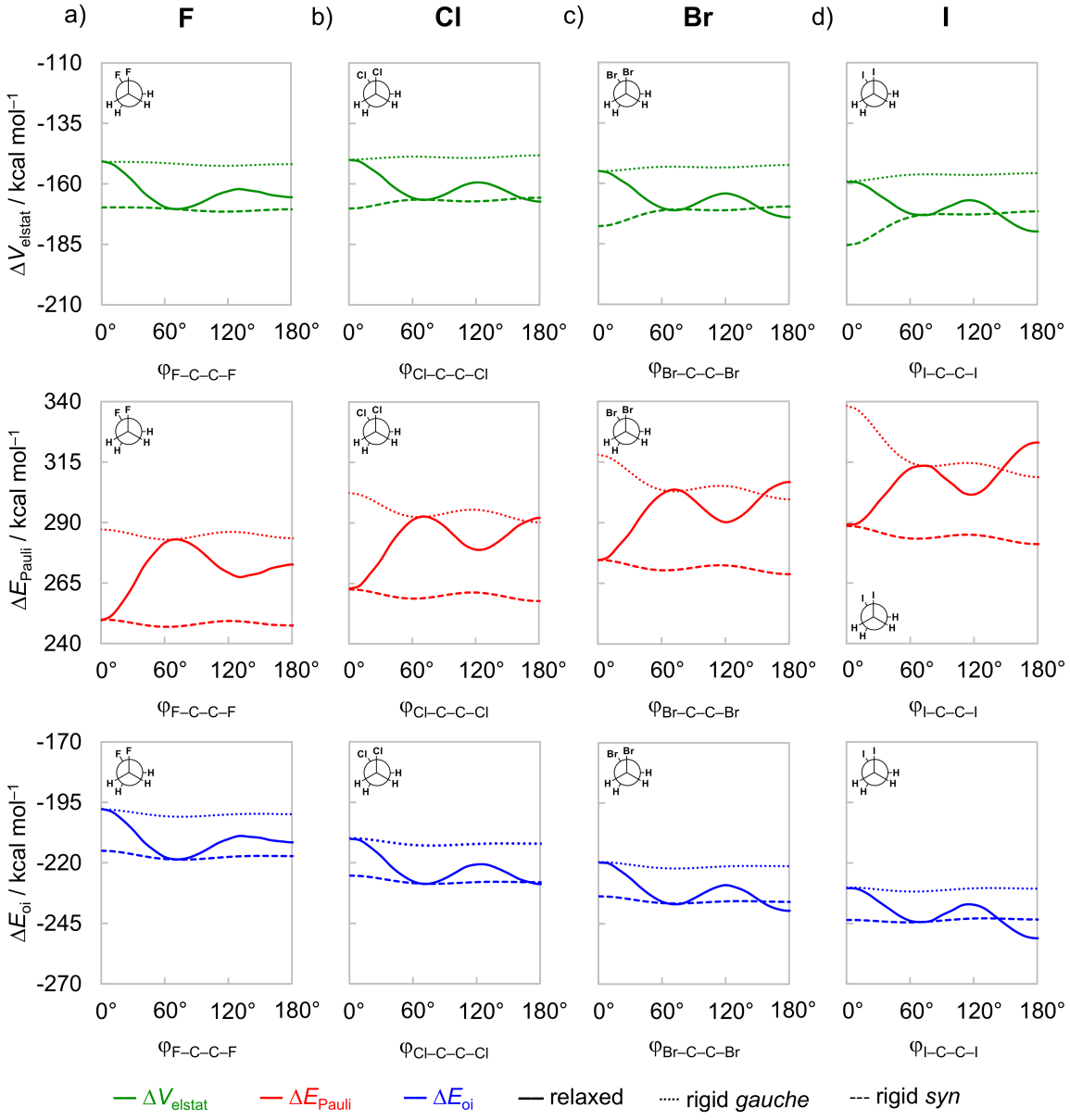

Appendix 4.4: Electrostatic interaction, Pauli repulsion, and orbital interaction energy terms as a function of the $\varphi_{X–C–C–X}$ dihedral angle of the 1,2-dihaloethanes $XH_2C–CH_2X$ (X = F, Cl, Br, I). Full lines: EDA for fully relaxed rotation; doted lines: EDA for rigid rotation in frozen *gauche* geometry; dashed lines: EDA for rigid rotation in frozen *syn* geometry. Computed at ZORA-BP86-D3(BJ)/QZ4P.

Appendix 4.5: EDA terms (in kcal mol^{-1}) of the energy minimum stationary points relative to the *syn* conformer in rigid rotation around the C–C bond in *gauche* geometry but with C–C distance set to 1.52 Å.[a]

X	$\Delta\Delta E_{int}$		$\Delta\Delta V_{elstat}$		$\Delta\Delta E_{Pauli}$		$\Delta\Delta E_{oi}$		$\Delta\Delta E_{disp}$	
	gau	*anti*	*gau*	*anti*	*gau*	*anti*	*gau*	*anti*	*gau*	*anti*
F	–8.0	–6.3	–0.7	–0.8	–3.8	–3.4	–3.5	–2.1	0.0	0.0
Cl	–9.1	–9.6	3.6	4.3	–9.6	–11.7	–3.3	–2.7	0.1	0.5
Br	–10.3	–11.3	6.6	7.8	–10.3	–11.3	–2.8	–2.2	0.2	0.7
I	–12.1	–13.4	11.9	13.4	–23.5	–28.1	–0.9	0.1	0.3	1.2

[a] Compute at ZORA-BP86-D3(BJ)/QZ4P.

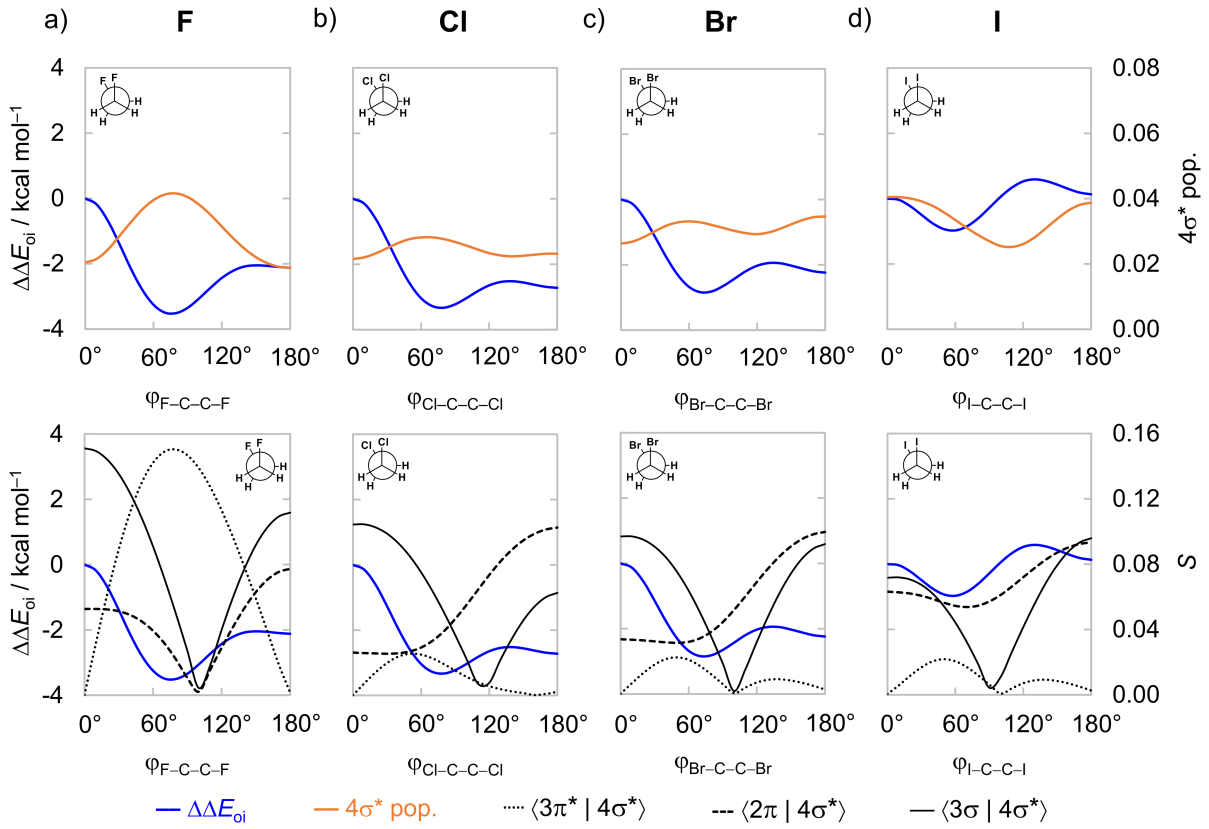

Appendix 4.6: Orbital interactions along with the gross population of the 4σ* orbital and the main occupied–unoccupied orbital overlaps as a function of the $\varphi_{X–C–C–X}$ dihedral angle of the 1,2-dihaloethanes $XH_2C–CH_2X$ (X = F, Cl, Br, I). Analysis in rigid rotation in *gauche* geometry with C–C distance set to 1.52 Å. Computed at ZORA-BP86-D3(BJ)/QZ4P.

5 PAPER 3 – DIPOLAR REPULSION IN α-HALOCARBONYL COMPOUNDS

Part of this chapter previously appeared as

Dipolar Repulsion in α-Halocarbonyl Compounds Revisited
D. Rodrigues Silva, L. de Azevedo Santos, T. A. Hamlin, F. M. Bickelhaupt,
M. P. Freitas, C. Fonseca Guerra
Phys. Chem. Chem. Phys. **2021**, *23*, 20883–20891

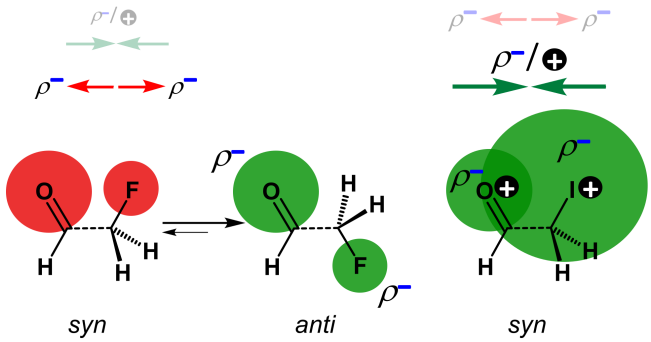

Abstract: The concept of dipolar repulsion has been widely used to explain several phenomena in organic chemistry, including the conformational preferences of carbonyl compounds. This model, in which atoms and bonds are viewed as point charges and dipole moment vectors, respectively, is however oversimplified. To provide a causal model rooted in quantitative molecular orbital theory, we have analyzed the rotational isomerism of haloacetaldehydes OHC–CH_2X (X = F, Cl, Br, I), using relativistic density functional theory. We have found that the overall trend in the rotational energy profiles is set by the combined effects of Pauli repulsion (introducing a barrier around *gauche* that separates minima at *syn* and *anti*), orbital interactions (which can pull the *anti* minimum towards *anticlinal* to maximize hyperconjugation), and electrostatic interactions. Only for X = F, not for X = Cl – I, electrostatic interactions push the preference from *syn* to *anti*. Our bonding analyses show how this trend is related to the compact nature of F versus the more diffuse nature of the heavier halogens.

Keywords: Carbonyl group, Conformation analysis, Density functional calculations, Electrostatic interactions, Point charges

5.1 Introduction

The carbonyl group is one of the most common functional groups in organic chemistry. Its unique chemistry renders the carbonyl group a site for a wide spectrum of chemical transformations[1] and interactions[2] that govern the structure of important biological systems, such as proteins,[3] and nucleic acids.[4] Attempts to understand and rationalize the structure and properties of compounds bearing a carbonyl group abound.[5] In particular, the forces underlying their conformational preferences, and the resulting influence on their physical, chemical, and biological properties, have intrigued organic chemists for decades.[6]

Several theoretical[7] and experimental[8] studies have explored the conformational landscape of haloacetaldehydes OHC–CH_2X (X = F, Cl, Br, I) as archetypal model systems to investigate the main intramolecular interactions involving the carbonyl group. The rotation around the C–C bond in these systems results in the energy profile schematically illustrated in Figure 5.1a. The relative conformational stability has typically been ascribed to dipolar interactions, that is, the *syn* conformer (*i.e.*, $\varphi_{O=C-C-X}$ = 0°) experiences a strong electrostatic repulsion between the partially negatively charged oxygen and halogen atoms, which shifts the conformational equilibrium to *anti* (*i.e.*, $\varphi_{O=C-C-X}$ = 180°; see Coulombic interactions in Figure 5.1b).[7a] This is equivalent to the explanation that the O=C and C–X bond dipoles in the O=C–C–X arrangement achieve the most or least unfavorable dipole–dipole interaction in the case of maximum (*syn*) or minimal (*anti*) overall dipole moment (see dipole minimization in Figure 5.1b).[9] The same rationalization has also been used to explain conformational energies in other systems containing polar groups, such as in the anomeric effect.[10] Additionally, for heavier haloacetaldehydes, it is argued that the global energy minimum gradually shifts from the *anti* to the *anticlinal* conformation (*i.e.*, $\varphi_{O=C-C-X}$ = 120°) because of the better donor ability of the σ_{CX} orbital to engage in stabilizing orbital interaction with the π^*_{CO} orbital of the carbonyl group as X goes from F to I (see hyperconjugative interactions in Figure 5.1b).[7a,11]

The above concept of dipolar repulsion depicts the electrostatic interaction as deriving from the sum of pairwise interactions between atoms that follows Coulomb's law for the respective point charges; this same representation can also be found in organic chemistry textbooks.[12] However, the validity of such an oversimplified picture, the treatment of atoms as point charges, has been questioned in the literature. It can lead to incorrect predictions in, for instance, rationalizing the factors governing the conformational preferences of small organic molecules,[13] chemical bonding,[14] and non-covalent interactions.[15] Molecules are characterized by a more complex charge distribution of nuclei and a 3-dimensional electron

charge density that, more often than not, does not behave as a collection of point charges.[14b] For example, some diatomic molecules, such as N_2 and O_2, would not be bound without the contribution from the attractive electrostatic component.[14a]

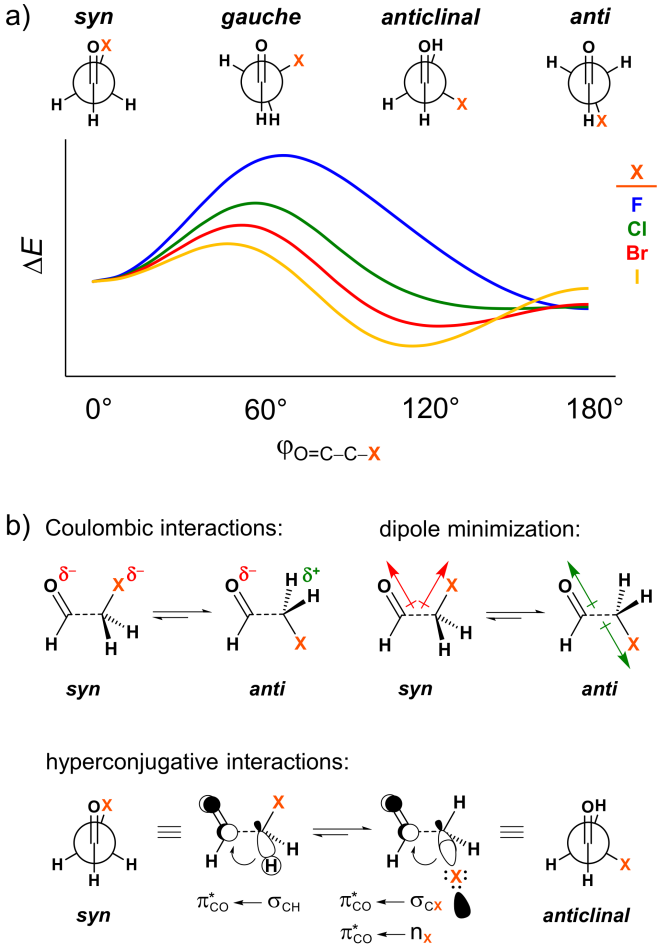

Figure 5.1: a) Stationary points in the energy profile for rotation around the C–C bond of haloacetaldehydes and b) intramolecular interactions used to rationalize the conformational preferences.

In this work, we have, therefore, analyzed the rotational isomerism of haloacetaldehydes OHC–CH_2X (X = F, Cl, Br, and I, see Figure 5.1) within the framework of quantitative Kohn-Sham molecular orbital (KS-MO) theory to reveal the physical mechanism behind the conformational preferences. In particular, we have investigated the role of dipolar repulsion as compared to other features in the bonding mechanism. Our bonding analyses show how the overall trend in the rotational energy profiles is set by the combined effects of Pauli repulsion, orbital interactions, and electrostatic interactions. Pauli repulsion, as will be explained, introduces a rotational barrier around *gauche* which separates minima at *syn* and *anti*. In

addition, orbital interactions can pull the *anti* minimum towards a more *anticlinal* conformation to maximize hyperconjugation. And, only for X = F, not for X = Cl – I, electrostatic interactions push the preference from *syn* to *anti*. Our results furthermore reveal how this trend in electrostatic interactions is related to the compact nature of F, which shows behavior that is reminiscent of a partially negative point charge that has Coulomb repulsion with the partially negative O. At variance, the more diffuse nature of the heavier halogens X = Cl – I cause a more pronounced overlap of charge densities between O and X which goes with a breakdown of the point-charge picture. The most striking consequence is a net stabilizing electrostatic interaction due to the reduced repulsion between the overlapping O and X densities in combination with significant stabilization of these densities by the nuclei of the other atom.

5.2 Methods

Computational Details

All calculations were performed using the Amsterdam Density Functional (ADF) software package.[16] The geometry of the stationary points and energy profile along rotation around the C–C bond of the haloacetaldehydes OHC–CH_2X (X = F, Cl, Br, and I) were calculated at the BP86 level of the generalized gradient approximation (GGA); exchange functional developed by Becke (B) and correlation functional developed by Perdew (P86).[17] The BP86 functional has been shown to accurately reproduce the rotational profile of 1,2-disubstituted ethanes.[18] The DFT-D3(BJ) method developed by Grimme and coworkers,[19] which contains the damping function proposed by Becke and Johnson,[20] was used to describe dispersion interactions. Scalar relativistic effects are accounted for using the zeroth-order regular approximation (ZORA).[21] Molecular orbitals (MO) were expanded in a large, uncontracted set of Slater type orbitals (STOs) containing diffuse functions: QZ4P.[22] The basis set is of quadruple-ζ quality augmented with polarization functions, *i.e.*, two 2*p* and two 3*d* sets on H, two 3*d* and two 4*f* sets on C, O, F; three 3*d* and two 4*f* sets on Cl, two 4*d* and three 4*f* sets on Br, one 5*d* and three 4*f* sets on I. All electrons were included in the variational process, *i.e.*, no frozen core approximation was applied. The accuracies of the fitting scheme (ZLM fit)[23] and the integration grid (Becke grid)[24] were set to 'VERY GOOD'. All optimized structures were confirmed to be true minima (no imaginary frequencies) or transition states (only one imaginary frequency) through vibrational analyses.[25]

Activation Strain Model and Energy Decomposition Analysis

To understand how the OHC–CH_2X bonding mechanism determines conformational preferences, we have analyzed this bond explicitly for all four haloacetaldehydes in terms of two open-shell fragments, $OHC^{\bullet}$ and $CH_2X^{\bullet}$, forming a C–C electron-pair bond in various conformations (*i.e.*, by varying the $\varphi_{O=C-C-X}$ dihedral angle). The overall bond energy ΔE has been divided into two major components using the activation strain model (ASM),[26] ΔE_{strain} and ΔE_{int}, and projected these values onto $\varphi_{O=C-C-X}$ [Eq. (5.1)].

$$\Delta E = \Delta E_{strain} + \Delta E_{int} \tag{5.1}$$

In this equation, the strain energy ΔE_{strain} results from the distortion of the two open-shell fragments from their equilibrium structure to the geometry they acquire in the overall molecule, and ΔE_{int} is the actual interaction between the deformed fragments. The interaction energy ΔE_{int} was further decomposed using canonical energy decomposition analysis for open-shell fragments (EDA)[27] into four physically meaningful energy terms [Eq. (5.2)]: electrostatic interactions ΔV_{elstat}, steric Pauli repulsion ΔE_{Pauli}, stabilizing orbital interactions ΔE_{oi}, and corrections for dispersion interactions ΔE_{disp}.[19] A theoretical overview of this energy decomposition scheme is given in Chapter 2.5.

$$\Delta E_{int} = \Delta V_{elstat} + \Delta E_{Pauli} + \Delta E_{oi} + \Delta E_{disp} \tag{5.2}$$

The ΔV_{elstat} term, which corresponds to classical electrostatic interaction between the unperturbed charge distributions of the (deformed) fragments and is usually attractive, can be further divided into four components:[27a]

$$\begin{aligned}\Delta V_{elstat} = & \sum_{\substack{\alpha \in A \\ \beta \in B}} \frac{Z_\alpha Z_\beta}{R_{\alpha\beta}} - \int \sum_{\alpha \in A} \frac{Z_\alpha \rho_B(r)}{|r - R_\alpha|} dr - \int \sum_{\beta \in B} \frac{Z_\beta \rho_A(r)}{|r - R_\beta|} dr \\ & + \int\int \frac{\rho_A(r_1)\rho_B(r_2)}{r_{12}} dr_1 dr_2 \\ = & \ \Delta V_{elstat}(n_A n_B) + \Delta V_{elstat}(n_A \rho_B) + \Delta V_{elstat}(\rho_A n_B) + \Delta V_{elstat}(\rho_A \rho_B)\end{aligned} \tag{5.3}$$

where A and B stand for $OHC^{\bullet}$ and $CH_2X^{\bullet}$, respectively. The first term is the electrostatic repulsion between the nuclei of fragments A and B, $\Delta V_{elstat}(n_A n_B)$; the second and third terms

are the electrostatic attraction between the nuclei of fragment A and the electron density of fragment B, $\Delta V_{elstat}(n_A\rho_B)$, and *vice versa*, $\Delta V_{elstat}(\rho_A n_B)$; while the last term is the electrostatic repulsion between the electron densities of fragments A and B, $\Delta V_{elstat}(\rho_A\rho_B)$.

For the purpose of clarity, all above-mentioned energy terms along rotation around the C–C bond are considered relative to the *syn* conformation (*i.e.*, $\varphi_{O=C-C-X} = 0°$) and represented as a $\Delta\Delta E$. To facilitate the analyses, the ASM and EDA were performed using the PyFrag 2019 program.[28]

5.3 Results and Discussion

Rotational Energy Profiles

The energy profiles for half a rotation around the C–C bond, that is, from $\varphi_{O=C-C-X} = 0°$ to 180°, of all haloacetaldehydes from our ZORA-BP86-D3(BJ)/QZ4P calculations are given in Figure 5.2. Note that only half a rotation is shown because the energy profile from 180° to 360° mirrors the one from 0° to 180°. From Figure 5.2a, we note the well-known energy profile of these systems which features two minimum-energy conformations: (i) one is always the *syn* conformer and (ii) the second one gradually changes its geometric character from *anti* to *anticlinal*, as X goes from F to I. This latter conformer is the global energy minimum in all cases, in line with earlier reports in the literature.[8] Furthermore, the energy profile for half a rotation of the fluoroacetaldehyde has a onefold rotational barrier with one energy maximum around the *gauche* orientation (*i.e.*, $\varphi_{O=C-C-X} = 70°$), whereas the iodoacetaldehyde has a twofold rotational barrier with energy maxima at the *gauche* and *anti*-conformations.

To understand the origin of the conformational energy differences, the various contributors to the bond energy along internal rotation around the C–C bond were analyzed by applying the activation strain model (ASM)[26] with canonical energy decomposition analysis (EDA)[27]. At this point, it is important to emphasize that the energy components are highly dependent on the geometry and the distance between the fragments.[26a] In previous studies,[18] we have shown that the interpretation of fully relaxed rotational energy profiles (*i.e.*, where all geometrical parameters are flexible to optimize during rotation) can be misleading because they comprise both, the change in the interaction terms due to the mutual reorientation of the two fragments along the internal rotation as well as the change in the interaction terms due to geometrical relaxation in response to the former changes (see Chapter 4). Along the relaxed

rotation around the C–C bond of 1,2-dihaloethanes, the C–C distance expands or contracts as a result of the steric Pauli repulsion experienced in each conformation. When the C–C bond is shorter, the various orbital and electrostatic interactions are maximized, and the opposite occurs when the C–C bond is longer. Therefore, the changes manifested in the interaction energy components are just a consequence of the C–C bond distance variation. Similar behavior is observed in the relaxed rotation of the haloacetaldehydes studied herein (see Appendix 5.1). Thus, to properly identify causalities in rotational profiles, it is necessary to perform the analysis at a rigid rotation around the C–C bond, that is, where all geometry parameters but the $\varphi_{O=C-C-X}$ torsion angle are kept unchanged. To this end, we take the *syn* conformer of each haloacetaldehyde at its equilibrium geometry and rotate it with fixed C–C bond length and $OHC^{\bullet}$ and $CH_2X^{\bullet}$ geometries to the *anti*-conformation. To compare all molecules on a more equal footing, the rotation of all haloacetaldehydes is performed from the same C–C distance set to 1.51 Å (as in the conformer with the shortest C–C bond length, *i.e.*, the *syn*-iodoacetaldehyde; see Figure 5.2b). We note that, although physically plausible, our choices of geometrical constraints might seem somewhat arbitrary. We have, therefore, verified that all trends and conclusions that play a role in the following discussion are not affected if other plausible choices of fragment geometry and C–C distance are made. The same overall trend is found if the rigid rotation is performed from their equilibrium *syn* or *anti* geometries or in a longer C–C bond length (see Appendix 5.2).

Inspection of the EDA plots in Figure 5.2b reveals three major features about the rotational isomerism of haloacetaldehydes: (i) a barrier around *gauche* because of an increased steric Pauli repulsion $\Delta\Delta E_{\text{Pauli}}$ (red curve) that separates *anti* and *syn* energy minima; (ii) the global energy minimum shifts from *anti* to *anticlinal* as X goes from F to I to maximize stabilizing orbital interactions $\Delta\Delta E_{\text{oi}}$ (blue curve); and (iii) the only contribution from electrostatic interactions $\Delta\Delta V_{\text{elstat}}$ (green curve) is to stabilize the *anti*-form for X = F. Note that the dispersion energy $\Delta\Delta E_{\text{disp}}$ (grey curve) remains nearly constant upon rotation around the C–C bond and, therefore, does not contribute to the overall trend in the rotational energy profiles. For the purpose of clarity, all energy terms are represented as a $\Delta\Delta E$ relative to the *syn* conformer. Thus, the strain energy ΔE_{strain} vanishes in this analysis because it is constant for geometrically frozen fragments; that is, $\Delta\Delta E_{\text{strain}}$ is zero and $\Delta\Delta E_{\text{int}} = \Delta\Delta E$. In the following, we address each one of the abovementioned features and their underlying physical mechanism individually.

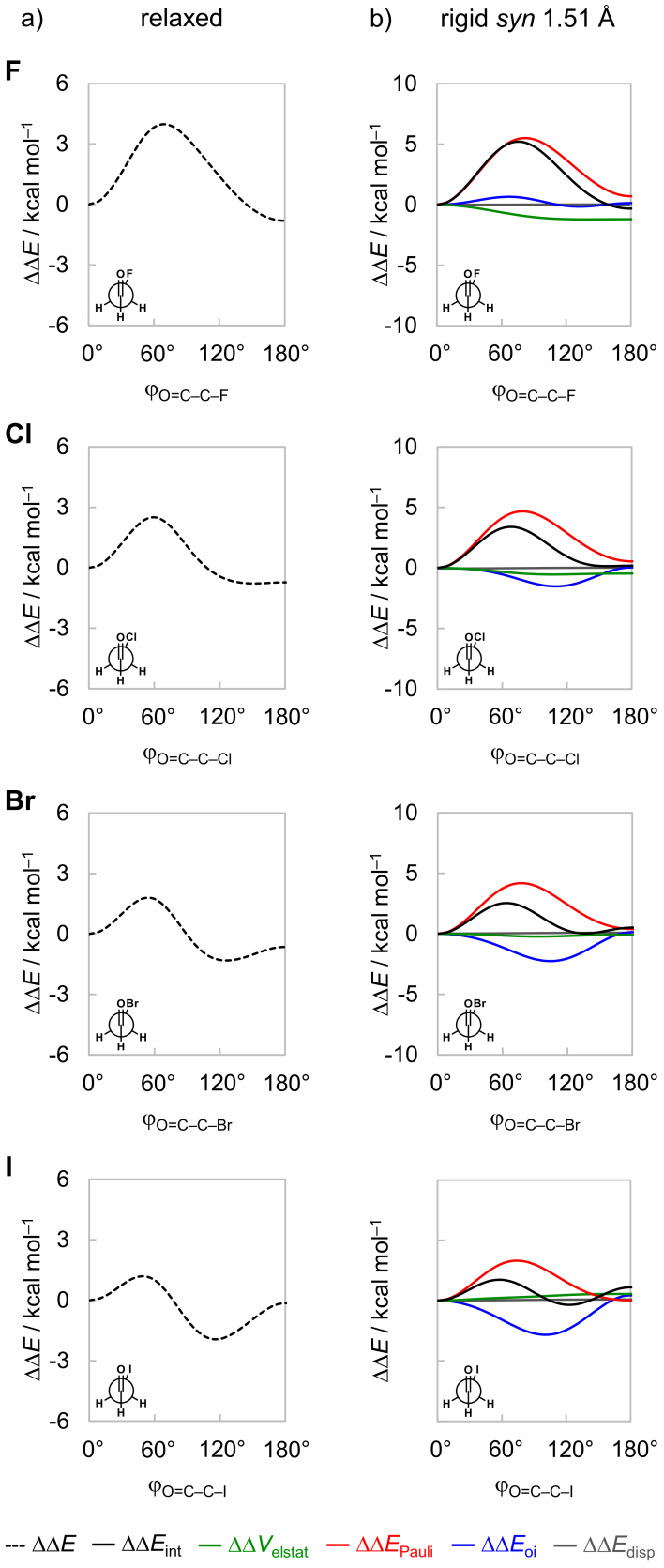

Figure 5.2: Rotational energy profile as a function of the $\varphi_{O=C-C-X}$ dihedral angle of haloacetaldehydes OHC–CH_2X (X = F, Cl, Br, and I). a) fully relaxed rotation around the C–C bond, and b) energy decomposition analysis (EDA) for rigid rotation in *syn* geometry but with a fixed C–C distance set to 1.51. Energy terms relative to the *syn* conformer, $\Delta\Delta E$, computed at ZORA-BP86-D3(BJ)/QZ4P.

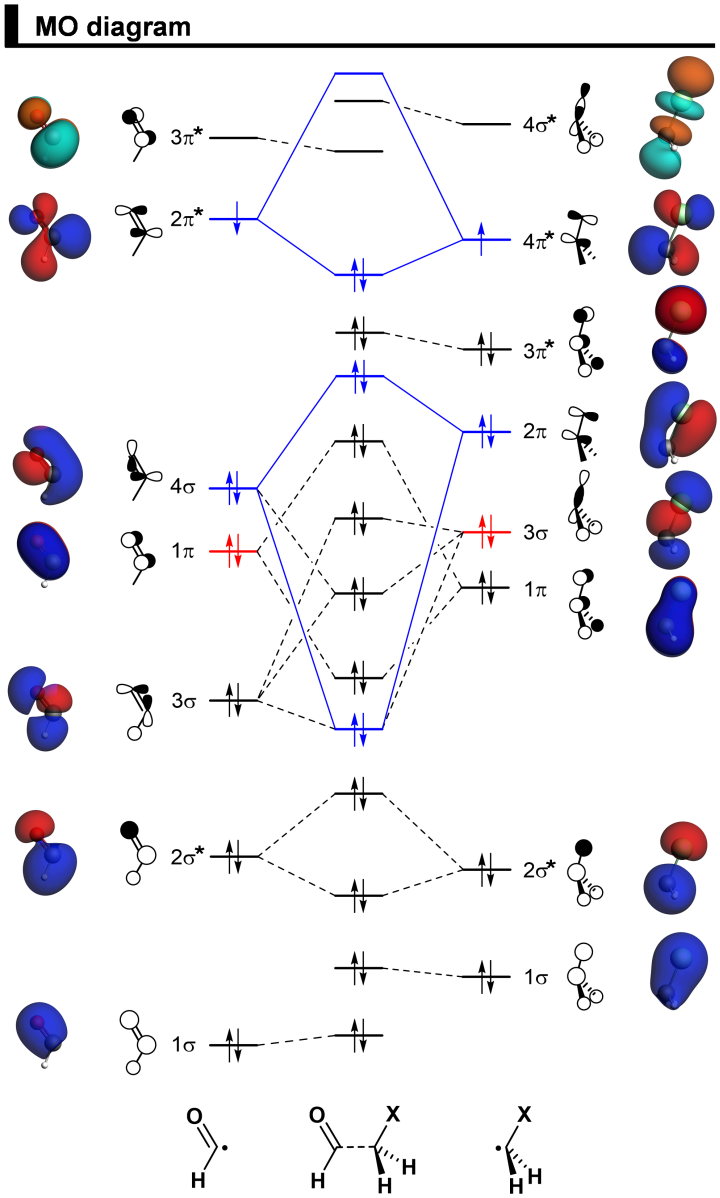

Figure 5.3: Schematic MO diagram for the formation of the *syn*-haloacetaldehydes OHC–CH_2X (X = F, Cl, Br, I) from two open-shell fragments, $OHC^{\bullet}$ and $CH_2X^{\bullet}$, along with the fragment molecular orbitals (FMO) depicted as quantitative 3D plots (isovalue = 0.04) for the representative *syn*-chloroacetaldehyde, computed at ZORA-BP86-D3(BJ)/QZ4P. Note that the overlap between the closed shell 1π $OHC^{\bullet}$ and 3σ $CH_2X^{\bullet}$ orbitals (in red) builds up from $\varphi_{O=C-C-X} = 0°$ to 90° and causes the central rotational barrier (see Figure 5.4).

Steric Pauli Repulsion and Rotational Barriers

Our analysis of rotational energy profiles reveals that steric Pauli repulsion $\Delta\Delta E_{Pauli}$ is the dominant term behind main rotational trends, namely, the central rotational barrier and the fact that both *anti* (for heavier halogens hyperconjugation pulls *anti* towards *anticlinal*, *vide infra*) and *syn* are energy minimum conformers. This is one more example that highlights the

important role of steric Pauli repulsion in controlling rotational landscapes of organic molecules.[18,29] As seen from Figure 5.2b, $\Delta\Delta E_{Pauli}$ is a minimum at the *syn* and *anti*-conformations and goes to a maximum when the OHC• and CH_2X• fragments are nearly perpendicular (*i.e.*, $\varphi_{O=C-C-X}$ is *ca.* 70-80°). The most significant closed-shell–closed-shell overlap contributing to the trend in $\Delta\Delta E_{Pauli}$ arises between the C=O π-bonding OHC• FMOs with the C–X σ-bonding CH_2X• FMOs, that is, ⟨1π|3σ⟩. The MO diagram with the valence orbitals of the OHC• and CH_2X• fragments is provided in Figure 5.3 and the ⟨1π|3σ⟩ overlap is illustrated in more detail in Figure 5.4. Note that ⟨1π|3σ⟩ is zero at the *syn* and *anti*-conformations as the 3σ orbital of CH_2X• overlaps symmetrically with the nodal plane region of the 1π orbital of OHC• (see Figure 5.4). But, as the dihedral angle $\varphi_{O=C-C-X}$ is rotated in between, ⟨1π|3σ⟩ deviates from zero and achieves a maximum around 90°. This maximum becomes larger and the effect is more pronounced as the 3σ orbital becomes more diffuse, *i.e.*, for heavier halogens X. For example, at $\varphi_{O=C-C-X}$ = 90°, ⟨1π|3σ⟩ varies from a value of 0.06 to

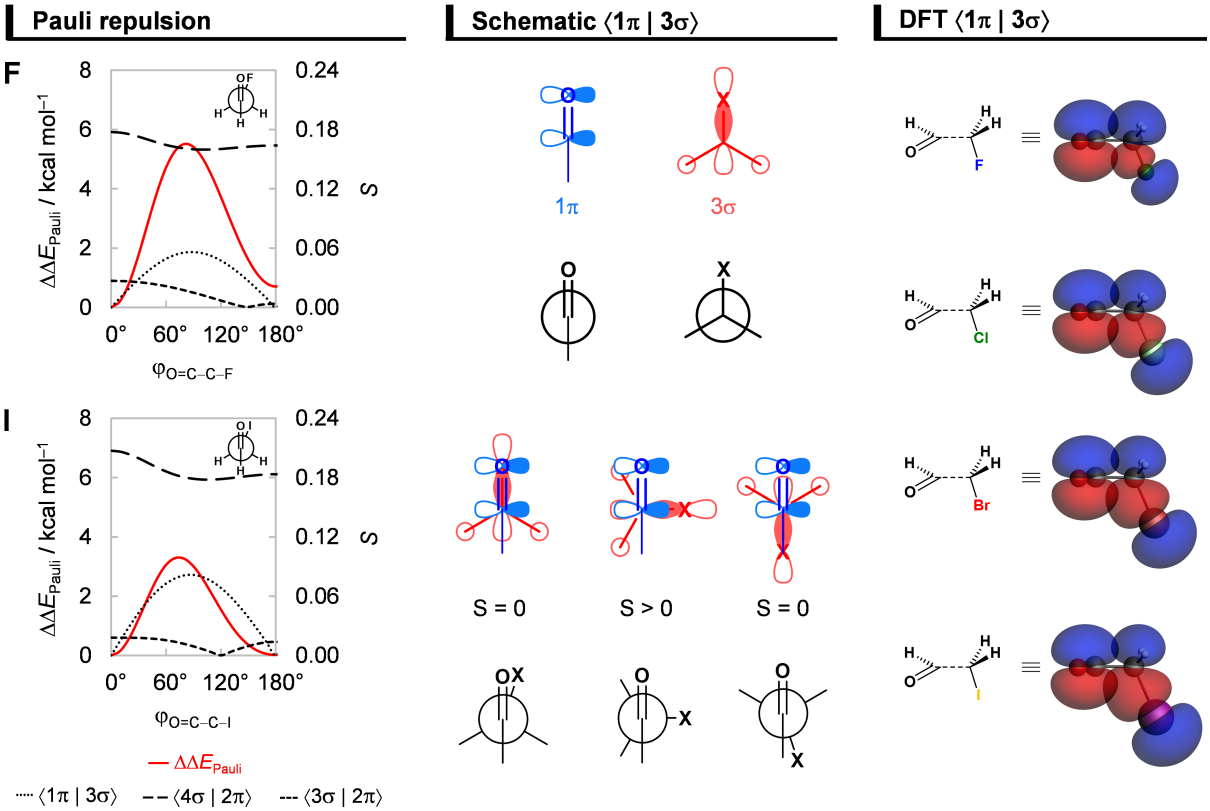

Figure 5.4: Steric Pauli repulsion $\Delta\Delta E_{Pauli}$ and the most significant occupied–occupied orbital overlaps *S* as a function of the $\varphi_{O=C-C-X}$ dihedral angle of the fluoro and iodoacetaldehydes, schematic representation of the ⟨1π|3σ⟩ overlap for $\varphi_{O=C-C-X}$ = 0° (*syn*), 90°, and 180° (*anti*), and the ⟨1π|3σ⟩ overlap depicted as 3D plots (isosurface at 0.03 a.u.) for all haloacetaldehydes. Analysis in rigid rotation in *syn* geometry but with C–C bond distance set to 1.51 Å. Energy terms relative to the *syn* conformer, $\Delta\Delta E$, computed at ZORA-BP86-D3(BJ)/QZ4P.

0.08 along X = F to I (see Figure 5.4). Similar behavior is found for the $\langle 1\pi|2\pi\rangle$ and $\langle 3\sigma|1\pi\rangle$ overlap integrals (see Appendix 5.3; see also Appendix 5.4 for the orbital overlap depicted as 3D plots).

It is interesting to observe that $\Delta\Delta E_{\text{Pauli}}$ along rotation around the C–C bond favors the *syn* conformer, where the most electron-rich atoms on each fragment are in closest proximity. The reason for this is twofold. Firstly, the overlap between FMOs that possess O and X lone-pair character, $\langle 3\sigma|2\pi\rangle$ and $\langle 4\sigma|2\pi\rangle$, expected to give a more destabilizing $\Delta\Delta E_{\text{Pauli}}$ at the *syn*, only slightly changes upon rotation around the C–C bond (see Figure 5.4). This is because the overlapping region is largest in between the two carbons, on the C–C bond region, and, therefore, varies less as a function of the $\varphi_{\text{O=C–C–X}}$ torsional angle (see Appendix 5.4 for the 3D plots of $\langle 3\sigma|2\pi\rangle$ and $\langle 4\sigma|2\pi\rangle$). Secondly, the $3\pi^*$ orbital, one of the main contributors to the Pauli repulsion in the rotational barrier of 1,2-dihaloethanes,[18b] is actually empty in the OHC$^\bullet$ fragment (see Figure 5.3) and, thus, $\langle 3\pi^*|3\pi^*\rangle$ does not give rise to any Pauli repulsion between the OHC$^\bullet$ and $CH_2X^\bullet$ fragments. Therefore, the trends in steric Pauli repulsion of haloacetaldehydes stem mostly from the $\langle 1\pi|3\sigma\rangle$ overlap integral (Figure 5.4), which is zero at the *syn* and *anti*-conformations.

Hyperconjugative Interactions

Next, we comment on the role of orbital (hyperconjugative) interactions $\Delta\Delta E_{\text{oi}}$ to the conformational energies. In agreement with previous reports in the literature,[7a,11] the hyperconjugation becomes increasingly more stabilizing at the *anticlinal* conformer for heavier haloacetaldehydes (see Figure 5.5). This is the reason why the global energy minimum conformation gradually shifts from *anti* to *anticlinal* as X goes from F to I. The stabilization due to $\Delta\Delta E_{\text{oi}}$ results predominantly from a charge transfer into the empty C=O π^*-antibonding OHC$^\bullet$ FMO from the occupied C–X σ-bonding $CH_2X^\bullet$ FMO, that is, the $3\pi^*$–3σ interaction (see Figure 5.5). Additional but less stabilizing contribution from the $3\pi^*$–2π interaction is given in Appendix 5.3 and 5.5. These orbital interactions are more stabilizing for the iodoacetaldehyde because of both smaller orbital energy gap and larger orbital overlap (*e.g.*, $\Delta\varepsilon_{3\pi^*-3\sigma}$ = 9.9 and 6.5 eV, and $\langle 3\pi^*|3\sigma\rangle$ = 0.12 and 0.18 for X = F and I, respectively). As the electronegativity of the halogen atom decreases from F to I,[30] the 3σ orbital becomes higher in energy, which leads to a smaller energy gap with the $3\pi^*$ orbital of OHC$^\bullet$. The associated $\langle 3\pi^*|3\sigma\rangle$ orbital overlap is largest at $\varphi_{\text{O=C–C–X}} = 90°$ (see Figures 5.5, and Appendix 5.3 for data along the rotation of the C–C bond) and increases as the 3σ orbital becomes more diffuse, due

to the larger *n*p atomic orbital of heavier halogen atoms. These findings consolidate earlier studies on the role of hyperconjugative orbital interactions.[7a,11]

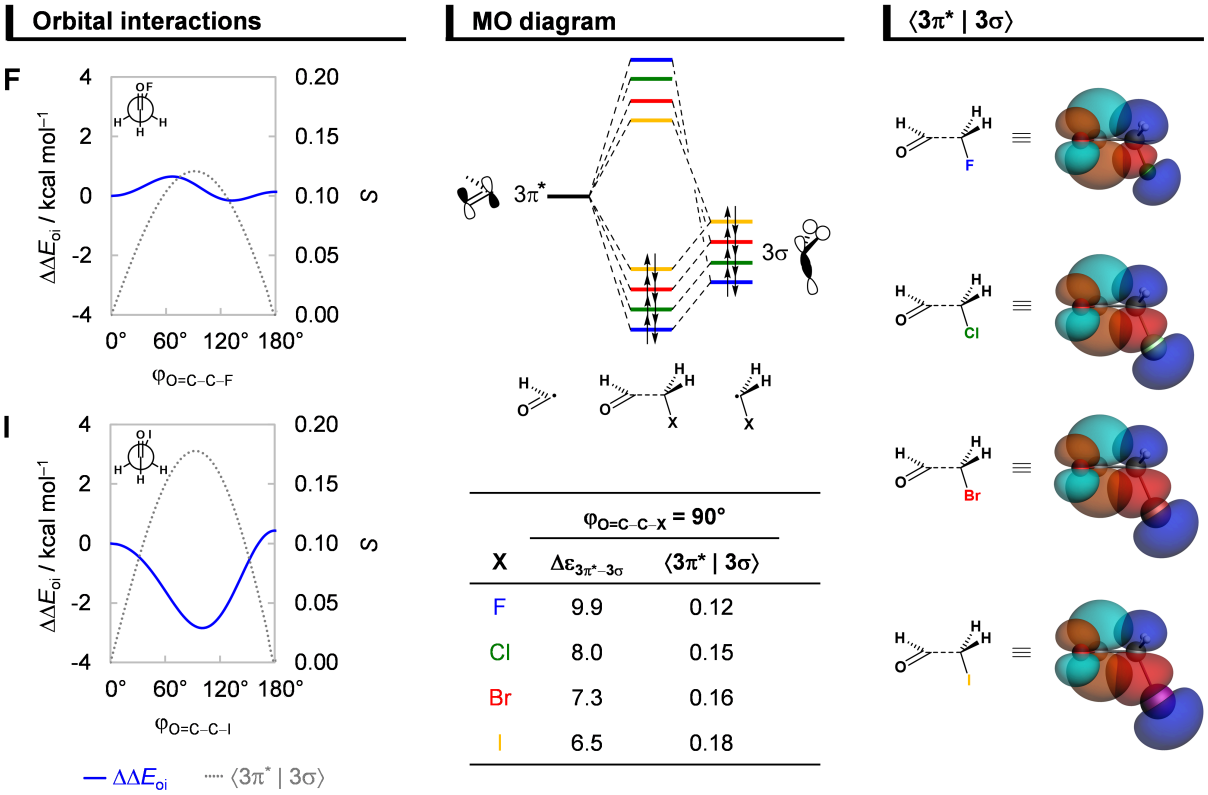

Figure 5.5: Orbital interactions as a function of the $\varphi_{O=C-C-X}$ dihedral angle of the fluoro and iodoacetaldehydes, MO diagram along with the orbital energy gap (in eV) and overlap for the donor–acceptor interaction between the unoccupied 3π* orbital of OHC$^{\bullet}$ and the occupied 3σ orbital of $CH_2X^{\bullet}$ (isosurface at 0.03 a.u.) of all haloacetaldehydes. Analysis in rigid rotation in *syn* geometry but with C–C distance set to 1.51 Å. Energy terms relative to the *syn* conformer, $\Delta\Delta E$, computed at ZORA-BP86-D3(BJ)/QZ4P.

Electrostatic Interactions and Dipolar Repulsion

Finally, we address the small role of electrostatic interactions $\Delta\Delta V_{elstat}$ to the rotational energy profiles, which, for X = F and I, favors *anti* and *syn*, respectively (see Figure 5.2b). As will become clear in the following, this difference in preference originates from the small, compact nature of fluorine and the large, more diffuse nature of iodine. The small nucleus and compact electron density render the fluorine atom a point-charge-like behavior, which gradually fades as one goes down group 17 in the periodic table. The large nucleus and more diffuse electron density of the iodine atom result in more electrostatic attraction with the electron density and nucleus of the oxygen atom, respectively, as well as less repulsion between electron densities

compared to point charges. This results in the rotational trends mentioned above, that is, along the $\Delta\Delta V_{elstat}$ curve, the *anti* is preferred for X = F to reduce electrostatic repulsion, whereas the opposite is observed for X = I, the preference shifts to *syn* to enhance electrostatic attraction.

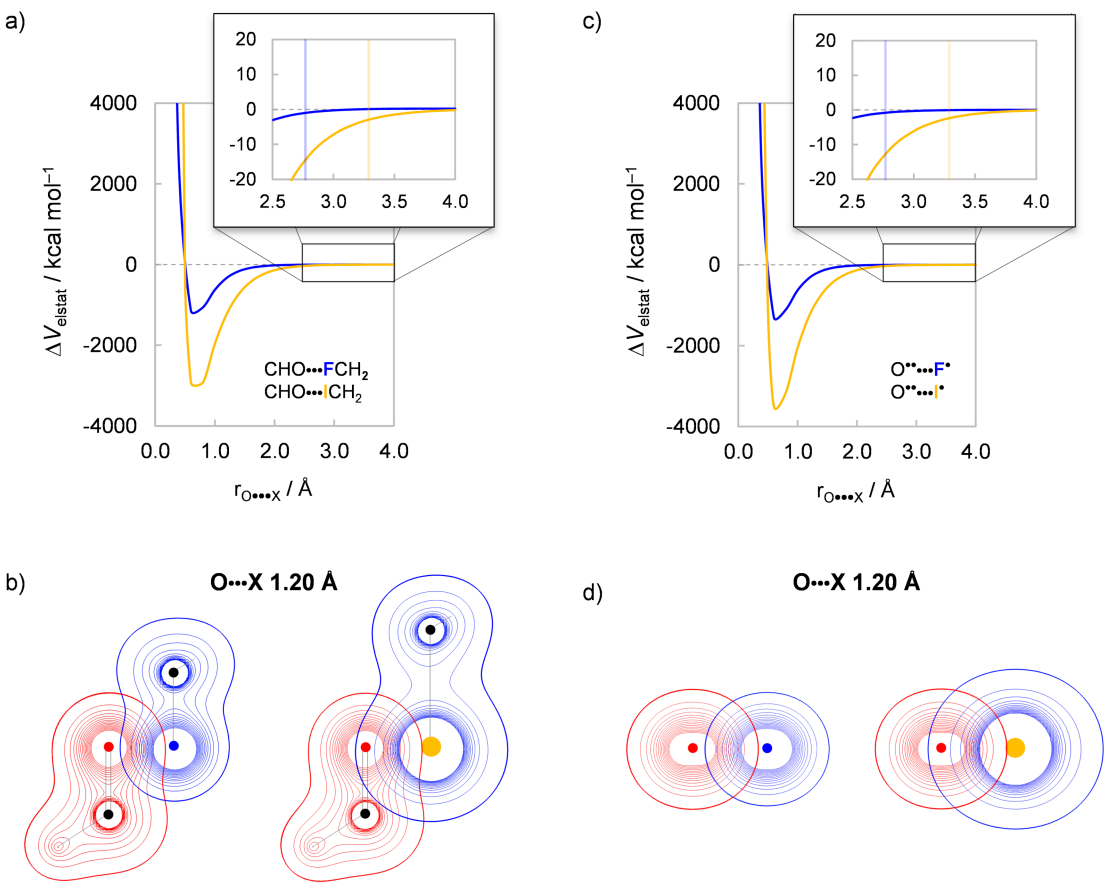

Figure 5.6: Electrostatic interaction between oxygen and halogen atoms. a) ΔV_{elstat} as a function of the $r_{O\cdots X}$ distance and b) density contours from –0.9 to 0.9 Bohr^{-3} for the lateral approach of the OHC$^{\bullet}$ and $CH_2X^{\bullet}$ fragments. c) ΔV_{elstat} as a function of the $r_{O\cdots X}$ distance and b) density contours from –0.9 to 0.9 Bohr^{-3} for the approach of the isolated O$^{\bullet\bullet}$ and X$^{\bullet}$ atoms in the electronic configuration of the haloacetaldehydes. Vertical lines indicate the $r_{O\cdots X}$ separation in the geometry of the corresponding haloacetaldehyde. Computed at ZORA-BP86-D3(BJ)/QZ4P.

To specifically evaluate the magnitude of the electrostatic interaction between the oxygen and halogen atoms, we approach the OHC$^{\bullet}$ and $CH_2X^{\bullet}$ fragments not by forming a C–C electron-pair bond, but along the O•••X distance (where X = F and I), as shown in Figures 5.6a and 5.6b. The ΔV_{elstat} energy becomes repulsive only at a very short internuclear distance ($r_{O\cdots X} < 0.8$ Å), which stems mostly from the nuclei-nuclei repulsion.[14b] Note that the physical

nature of the charge densities is different from point charges, and the former yields less electrostatic repulsion than the latter.[14a] Furthermore, ΔV_{elstat} is less stabilizing for X = F than X = I all along the O•••X distance, even at their $r_{O\cdots X}$ distance in the corresponding haloacetaldehydes (see vertical lines in Figure 5.6a). The same overall trend is observed if one analyzes the electrostatic interaction by approaching the OHC• and CH_2X• fragments along the C=O•••X–C bond axis (see Appendix 5.6). This can be traced back to the electrostatic interaction between the bare O•• and X• atoms in the electronic configuration of the haloacetaldehydes (see Figures 5.6c and 5.6d). The overlap between electron densities and nuclei of the OHC• and CH_2X• fragments is better for X = I because the electron density of the iodine atom is more diffuse and its nucleus is larger than the fluorine atom (Figure 5.6d), resulting in stronger electrostatic attraction with the oxygen atom (Figure 5.6c). Therefore, the electrostatic interaction ΔV_{elstat} between OHC• and CH_2X• is predominantly attractive and increases in magnitude from X = F to I, leading to a breakdown of the point-charge picture.

However, at short distances, even the compact fluorine atom can deviate from point-charge behavior. Along the series of haloacetaldehydes, this can be achieved by artificially shortening the C–X bond length and, therefore, the O•••X separation. Table 5.1 shows the $\Delta\Delta V_{elstat}$ energy of the *syn* relative to the *anti*-conformation. We recall that ΔV_{elstat} is predominantly attractive and, therefore, positive (*i.e.*, less stabilizing) values of $\Delta\Delta V_{elstat}$ indicate that *syn* is electrostatically less favorable than *anti*, whereas negative (*i.e.*, more stabilizing) values of $\Delta\Delta V_{elstat}$ denote the opposite. By decreasing the O•••X distance, the overlap between electron densities and nuclei of OHC• and CH_2X• becomes more effective, resulting in more stabilizing electrostatics at the *syn* conformer for all haloacetaldehydes (see Table 5.1, column "C–X –0.3Å"). This is further corroborated by the fact that the *anti* preference dominates with the elongation of the C–X bond length and, therefore, of the O•••X distance (see Table 5.1, column "C–X +0.3Å"). At a longer O•••X separation, ΔV_{elstat} becomes less stabilizing, which shifts the electrostatic preference to *anti*. Thus, the electrostatic preference for *syn* or *anti* depends on the balance between the attractive and repulsive components of ΔV_{elstat} (see Eq. (5.3) and Appendix 5.3). For X = I, ΔV_{elstat} is strongly stabilizing and prefers to be *syn* to maximize the overlap between the electron density on one with the nuclei on the other of the OHC• and CH_2X• fragments. For X = F, on the other hand, the electrostatic attraction is weaker than for X = I and does not compensate for the electrostatic repulsion between nuclei and between densities on either fragment at *syn*, therefore shifting the preference to *anti* (see Appendix 5.7). The oversimplified concept of dipolar repulsion does not capture this interplay of electrostatic interactions. At variance with this rationale, the point-

charge-like behavior of the fluorine atom along the $\Delta\Delta V_{elstat}$ curve is not due to a larger electrostatic repulsion, but instead stems from the attractive electrostatic components that are less stabilizing than for larger halogens.

Table 5.1: *Syn* relative to *anti* electrostatic interactions $\Delta\Delta V_{elstat}$ (in kcal mol^{-1}) of haloacetaldehydes OHC–CH_2X (X = F, Cl, Br, and I).[a]

	C–X –0.3 Å	**C–X equil** [b]	**C–X +0.3 Å**
X	$\Delta\Delta V_{elstat}$	$\Delta\Delta V_{elstat}$	$\Delta\Delta V_{elstat}$
F	–0.4	1.2	2.4
Cl	–0.3	0.5	1.5
Br	–0.9	0.1	1.1
I	–1.7	–0.5	0.5

[a] Computed at ZORA-BP86-D3(BJ)/QZ4P. [b] Data from the rigid rotation in *syn* geometry but with C–C distance set to 1.51 Å.

5.4 Conclusions

The overall rotational energy profile of haloacetaldehydes OHC–CH_2X (X = F, Cl, Br, and I) is set by an interplay of steric Pauli repulsion, which causes a barrier separating *syn*- and *anti*-minima, orbital interactions, which pull the *anti*-minimum towards *anticlinal* in order to optimize hyperconjugative overlap, and electrostatic interactions, which drive the preference to *anti* only in the case of X = F. This follows from our detailed analyses based on relativistic dispersion-corrected density functional theory at ZORA-BP86-D3(BJ)/QZ4P.

The results of our quantitative Kohn-Sham molecular orbital theory analyses reveal that steric Pauli repulsion is the causal term giving rise to the central rotation barrier between *syn*- and *anti*-minima, which reaches a maximum when the C=O and C–X bonds are nearly perpendicular, due to the maximum overlap in the four–electron interaction between the filled π orbital of the carbonyl group with the filled σ orbital of the halogenated methyl fragment. This closed-shell–closed-shell orbital overlap is zero at the *syn* and *anti*-conformations because the $CH_2X^{\bullet}$ σ orbital overlaps symmetrically with the nodal plane region of the $OHC^{\bullet}$ π orbital. Therefore, Pauli repulsion is also the reason why the *syn* is an energy minimum conformer for all haloacetaldehydes. The global energy minimum, on the other hand, gradually shifts from *anti* to *anticlinal* as X goes from F to I because of the more stabilizing orbital interactions in the latter, in line with the currently accepted rationale. As the halogen atom increases in size, the orbital overlap becomes larger, and the orbital energy gap becomes smaller for the charge

transfer to the empty π* orbital of the carbonyl group from the filled σ orbital of the halogenated methyl.

Electrostatic interactions are intuitively seen as the repulsion or attraction between atoms with partial charges of the same or opposite signs, respectively. As such, they are often represented as the sum of pairwise interactions that follows Coulomb's law for the respective point charges, which is the center of the concept of dipolar repulsion. We show that this oversimplified view is, however, only valid for compact atoms, in our model systems, the second-row fluorine atom. As the halogen atom increases in size and becomes more diffuse, it deviates more from the behavior of point charge to an atomic charge distribution. This results in a net stabilizing electrostatic interaction between O and X arising from both less repulsion between overlapping densities and more attraction between overlapping density and nucleus. Therefore, while the electrostatic energy favors *anti* for X = F to reduce O(ρ^-)•••(ρ^-)F and O(⊕)•••(⊕)F repulsion, it favors *syn* for X = I to enhance O(⊕)•••(ρ^-)I and O(ρ^-)•••(⊕)I attractions.

5.5 References

[1] Clayden, J.; Greevs, N.; Warren, S. G. *Organic Chemistry*; Oxford University Press: Oxford, UK, **2012**.

[2] Newberry, R. W.; Raines, R. T. *Acc. Chem. Res.* **2017**, *50*, 1838–1846.

[3] (a) Pauling, L.; Corey, R. B.; Branson, H. R. *Proc. Natl. Acad. Sci. U. S. A.* **1951**, *37*, 205−211.(b) Pauling, L.; Corey, R. B. *Proc. Natl. Acad. Sci. U. S. A.* **1951**, *37*, 729−740.

[4] (a) Fonseca Guerra, C.; Bickelhaupt, F. M.; Snijders, J. G.; Baerends, E. J. *Chem. Eur. J.* **1999**, *5*, 3581−3594. (b) Watson, J. D.; Crick, F. H. C. *Nature* **1953**, *171*, 737−738.

[5] (a) Dickens, T. K.; Warren, S. *Chemistry of the Carbonyl Group: A Step-by-Step Approach to Understanding Organic Reaction Mechanisms*; John Wiley & Sons: Hoboken, NJ, **2018**. (b) Jones, J. *Core Carbonyl Chemistry*; Oxford University Press Inc.: New York, **1997**.

[6] See, for instance: (a) Muchowska, K. B.; Pascoe, D. J.; Borsley, S.; Smolyar, I. V.; Mati, I. K.; Adam, C.; Nichol, G. S.; Ling, K. B.; Cockroft, S. L. *Angew. Chem. Int. Ed.* **2020**, *59*, 14602–14608; *Angew. Chem.* **2020**, *132*, 14710–14716. (b) Rodrigues Silva, D.; Zeoly, L. A.; Cormanich, R. A.; Fonseca Guerra, C.; Freitas, M. P. *Eur. J. Org. Chem.* **2020**, *2020*, 884–890. (c) Pattison, G. *Beilstein J. Org. Chem.* **2017**, *13*, 2915–2921. (d) Martins, F. A.; Silla, J. M.; Freitas, M. P. *Beilstein J. Org. Chem.* **2017**, *13*, 1781–1787. (e) Cormanich, R. A.; Ducati, L. C.; Tormena, C. F.; Rittner, R. *Chem. Phys.* **2013**, *421*, 32–38. (f) Wiberg, K. B. *Acc. Chem. Res.*

1999, *32*, 922–929; and references cited therein. (g) Seeman, J. I. *Chem. Rev.* **1983**, *83*, 83–134. (h) Allinger, N. L.; Allinger, J.; DaRooge, M. A. *J. Am. Chem. Soc.* **1964**, *86*, 4061–4067.

[7] For selected theoretical studies, see: (a) Pontes, R. M.; Fiorin, B. C.; Basso, E. A. *Chem. Phys. Lett.* **2004**, *395*, 205–209. (b) Frenking, G.; Köhler, K. F.; Reetz, M. T. *Tetrahedron* **1994**, *50*, 11197–11204. (c) Phan, H. V.; Durig, J. R. *J. Mol. Struct. (Theochem.)* **1990**, *209*, 333–347. (d) Durig, J. R.; Phan, H. V.; Little, T.S. *J. Mol. Struct. (Theochem.)* **1989**, *202*, 143–157.

[8] For representative experimental studies, see: (a) Abraham, R. J.; Jones, A. D.; Warne, M. A.; Rittner, R.; Tormena, C. F. *J. Chem. Soc., Perkin Trans. 2* **1996**, 533–539. (b) Dyngeseth, S.; Schei, H.; Hagen, K. *J. Mol. Struct.* **1983**, *102*, 45–54. (c) Malloy, Jr., T. B.; Carreira, L. A. *J. Chem. Phys.* **1977**, *66*, 4246–4247. (d) Ford, R. G. *J. Chem. Phys.* **1976**, *65*, 354–362. (e) Karabatsos, G. J.; Fenoglio, D. J. *J. Am. Chem. Soc.* **1969**, *91*, 1124–1129. (f) Bellamy, L. J.; Williams, R. L. *J. Chem. Soc.* **1957**, 4294–4304.

[9] Juaristi, E.; Cuevas, G. *The anomeric effect*; CRC Press, Inc.: Boca Raton, Florida, **1995**.

[10] (a) Wiberg, K. B.; Bailey, W. F.; Lambert, K. M.; Stempel, Z. D. *J. Org. Chem.* **2018**, *83*, 5242–5255. (b) Filloux, C. M. *Angew. Chem. Int. Ed.* **2015**, *54*, 8880–8894; *Angew. Chem.* **2015**, *127*, 9006–9021. (c) Mo, Y. *Nat. Chem.* **2010**, *2*, 666–671. (d) Wang, C.; Ying, F.; Wu, W.; Mo, Y. *J. Org. Chem.* **2014**, *79*, 1571–1581.

[11] Coelho, J. V.; Freitas, M. P.; Ramalho, T. C. *Struct. Chem.* **2008**, *19*, 671–677.

[12] Eliel, E. L.; Wilen, S. H.; Mander, L. N. *Stereochemistry of Organic Compounds*; John Wiley & Sons, Inc.: New York, **1994**.

[13] (a) Solel, E.; Ruth, M.; Schreiner, P. R. *J. Org. Chem.* **2021**, Article ASAP. DOI: 10.1021/acs.joc.1c00767. (b) Baranac-Stojanović, M. *RSC Adv.* **2014**, *4*, 43834–43838.

[14] (a) Frenking, G.; Bickelhaupt, F. M. In *The Chemical Bond: Fundamental Aspects of Chemical Bonding*; Frenking, G.; Shaik, S., Eds.; Wiley-VCH: Weinheim, **2014**, 121–158. (b) Krapp, A.; Bickelhaupt, F. M.; Frenking, G. *Chem. Eur. J.* **2006**, *12*, 9196–9216. (c) Kovács, A.; Esterhuysen, C.; Frenking, G. *Chem. Eur. J.* **2005**, *11*, 1813–1825. (d) Esterhuysen, C.; Frenking, G. *Theor. Chem. Acc.* **2004**, *111*, 381–389.

[15] (a) Politzer, P.; Murray, J. S.; Concha, M. C. *J. Mol. Model.* **2008**, *14*, 659–665. (b) van der Lubbe, S. C. C.; Zaccaria, F.; Sun, X.; Fonseca Guerra, C. *J. Am. Chem. Soc.* **2019**, *141*, 4878−4885.

[16] (a) te Velde, G.; Bickelhaupt, F. M.; Baerends, E. J.; Fonseca Guerra, C.; van Gisbergen, S. J. A.; Snijders, J. G.; Ziegler, T. *J. Comput. Chem.* **2001**, *22*, 931–967. (b) Fonseca Guerra, C.; Snijders, J. G.; te Velde, G.; Baerends, E. J. *Theor. Chem. Acc.* **1998**, *99*, 391–403. (c) ADF2017.103, SCM Theoretical Chemistry; Vrije Universiteit, Amsterdam, The Netherlands, http://www.scm.com.

[17] (a) Becke, A. D. *Phys. Rev. A* **1988**, *38*, 3098−3100. (b) Perdew, J. P. *Phys. Rev. B* **1986**, *33*, 8822−8824.

[18] (a) Bickelhaupt, F. M.; Baerends, E. J. *Angew. Chem. Int. Ed.* **2003**, *42*, 4183–4188; *Angew. Chem.* **2003**, *115*, 4315–4320. (b) Rodrigues Silva, D.; de Azevedo Santos, L.; Hamlin, T. A.; Fonseca Guerra, C.; Freitas, M. P.; Bickelhaupt, F. M. *ChemPhysChem* **2021**, *22*, 641–648.

[19] (a) Grimme, S.; Antony, J.; Ehrlich, S.; Krieg, H. *J. Chem. Phys.* **2010**, *132*, 154104. (b) Grimme, S.; Ehrlich, S.; Goerigk, L. *J. Comput. Chem.* **2011**, *32*, 1456–1465.

[20] Johnson, E. R.; Becke, A. D. *J. Chem. Phys.* **2005**, 123, 024101.

[21] (a) van Lenthe, E.; van Leeuwen, R.; Baerends, E. J.; Snijders, J. G. *Int. J. Quantum Chem.* **1996**, *57*, 281–293. (b) van Lenthe, E.; Baerends, E. J.; Snijders, J. G. *J. Chem. Phys.* **1994**, *101*, 9783–9792.

[22] van Lenthe, E.; Baerends, E. J. *J. Comput. Chem.* **2003**, *24*, 1142–1156.

[23] Franchini, M.; Philipsen, P. H. T.; van Lenthe, E.; Visscher, L. *J. Chem. Theory Comput.* **2014**, *10*, 1994–2004.

[24] Franchini, M.; Philipsen, P. H. T.; Visscher, L. *J. Comput. Chem.* **2013**, *34*, 1819–1827.

[25] (a) Bérces, A.; Dickson, R. M.; Fan, L.; Jacobsen, H.; Swerhone, D.; Ziegler, T. *Comput. Phys. Commun.* **1997**, *100*, 247–262. (b) Jacobsen, H.; Bérces, A.; Swerhone, D. P.; Ziegler, T. *Comput. Phys. Commun.* **1997**, *100*, 263–276. (c) Wolff, S. K. *Int. J. Quantum Chem.* **2005**, *104*, 645–659.

[26] (a) Vermeeren, P.; van der Lubbe, S. C. C.; Fonseca Guerra, C.; Bickelhaupt, F. M.; Hamlin, T. *Nat. Protoc.* **2020**, *15*, 649–667. (b) Bickelhaupt, F. M.; Houk, K. N. *Angew. Chem. Int. Ed.* **2017**, *56*, 10070–10086; *Angew. Chem.* **2017**, *129*, 10204–10221. (c) Wolters, L. P.; Bickelhaupt, F. M. *WIRES Comput. Mol. Sci.* **2015**, *5*, 324–343. (d) Fernández, I.; Bickelhaupt, F. M. *Chem. Soc. Rev.* **2014**, *43*, 4953–4967. (e) van Zeist, W.-J.; Bickelhaupt, F. M. *Org. Biomol. Chem.* **2010**, *8*, 3118–3127. (f) Bickelhaupt, F. M. *J. Comput. Chem.* **1999**, *20*, 114–128.

[27] (a) Hamlin, T. A.; Vermeeren, P.; Fonseca Guerra, C.; Bickelhaupt, F. M. In *Complementary Bonding Analysis*; Grabowsky, S. Eds.; De Gruyter: Berlin, **2021**, pp 199–212; (b) Bickelhaupt, F. M.; Baerends, E. J. In *Reviews in Computational Chemistry*; Lipkowitz, K. B.; Boyd, D. B., Eds.; Wiley-VCH: New York, **2000**; Vol. 15, pp 1–86. (c) van Meer, R.; Gritsenko, O. V.; Baerends, E. J. *J. Chem. Theory Comput.* **2014**, *10*, 4432–4441.

[28] (a) van Zeist, W.-J.; Fonseca Guerra, C.; Bickelhaupt, F. M. *J. Comp. Chem.* **2008**, *29*, 312–315; (b) Sun, X.; Soini, T. M.; Poater, J.; Hamlin, T. A.; Bickelhaupt, F. M. *J. Comp. Chem.* **2019**, *40*, 2227–2233. (c) PyFrag 2007-2020: X. Sun, T. Soini, L. P. Wolters, W.-J. van Zeist, C. Fonseca Guerra, T. A. Hamlin, F. M. Bickelhaupt, Vrije Universiteit Amsterdam, The Netherlands.

[29] (a) Mo, Y.; Wu, W.; Song, L.; Lin, M.; Zhang, Q.; Gao, J. *Angew. Chem. Int. Ed.* **2004**, *43*, 1986–1990; Angew. Chem. 2004, 116, 2020–2024. (b) Mo, Y.; Gao, J. *Acc. Chem. Res.* **2007**, *40*, 113–119. (c) Chen, Z.; Corminboeuf, C.; Mo, Y. *J. Phys. Chem. A* **2014**, *118*, 5743–5747.

[30] (a) Pauling, L. *The Nature of the Chemical Bond*; Cornell University Press: Ithaca, NY, **1960**. (b) Allred, A. L. *J. Inorg. Nucl. Chem.* **1961**, *17*, 215–221.

5.6 Appendices

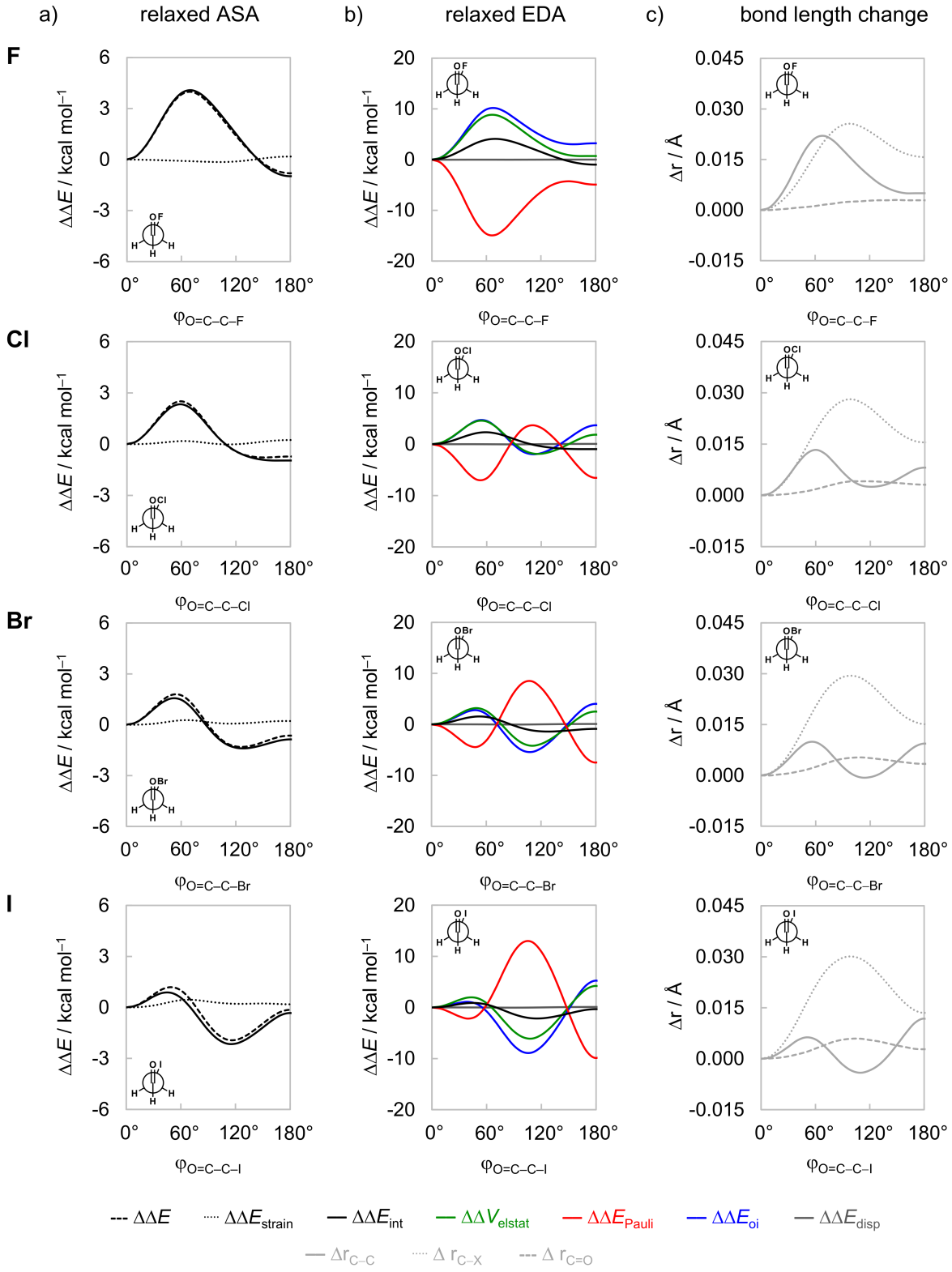

Appendix 5.1: a) Activation strain (ASA) and b) energy decomposition analyses (EDA) of the fully relaxed rotation around the C–C bond along with c) key bond length variations as a function of the $\varphi_{O=C-C-X}$ dihedral angle of haloacetaldehydes OHC–CH_2X (X = F, Cl, Br, and I). Energy terms and distances relative to the *syn* conformer, $\Delta\Delta E$ and Δr, computed at ZORA-BP86-D3(BJ)/QZ4P.

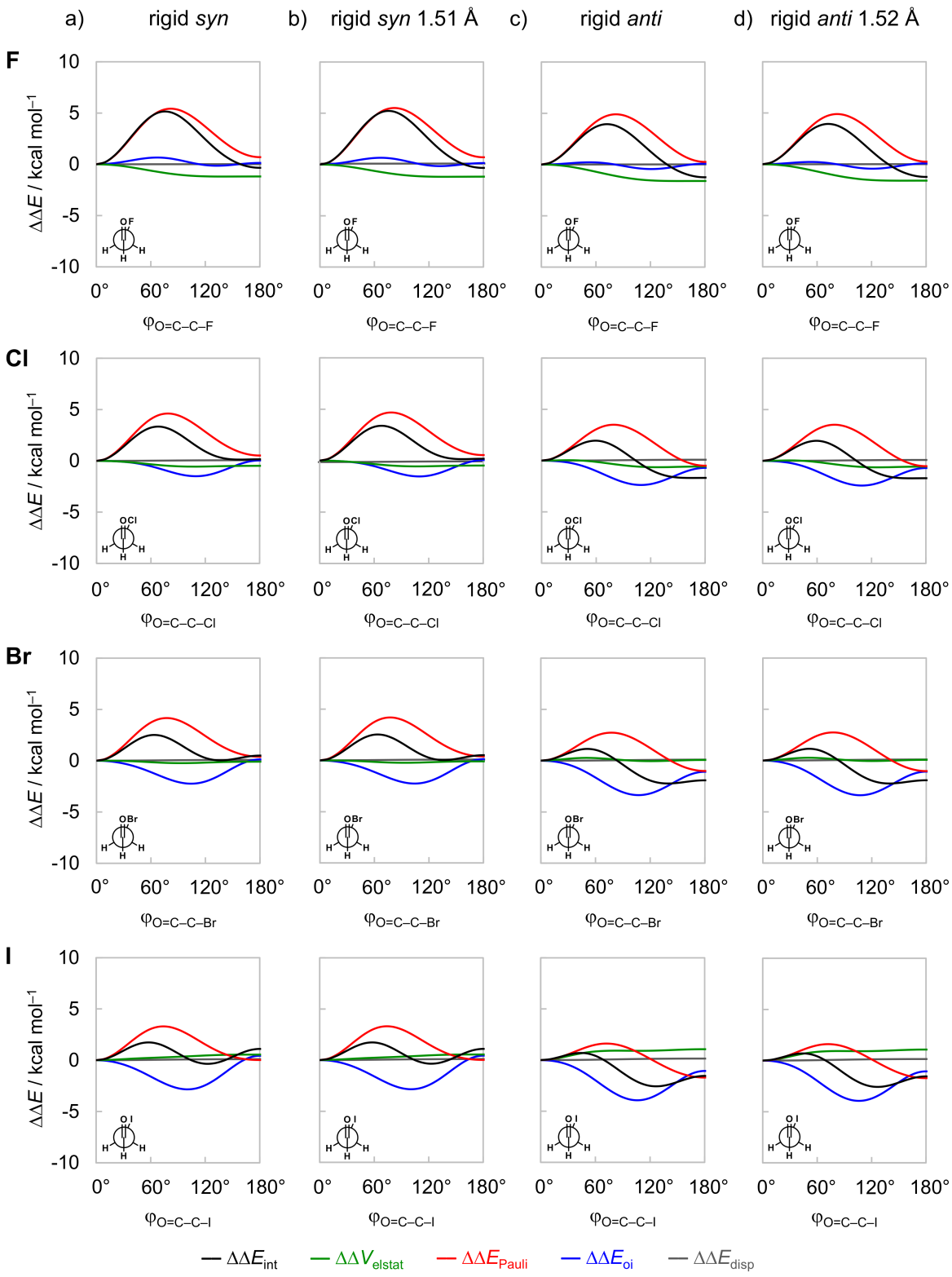

Appendix 5.2: Energy decomposition analysis (EDA) for rigid rotation around the C–C bond as a function of the $\varphi_{O=C-C-X}$ dihedral angle of haloacetaldehydes OHC–CH_2X (X = F, Cl, Br, and I). a) rigid rotation in *syn* geometry, b) rigid rotation in *syn* geometry but with C–C distance set to 1.51 Å (as in the *syn*-iodoacetaldehyde), c) rigid rotation in *anti*-geometry, and d) rigid rotation in *anti*-geometry but with C–C distance set to 1.52 Å (as in the *anti*-fluoroacetaldehyde). Energy terms relative to the *syn* conformer, $\Delta\Delta E$, computed at ZORA-BP86-D3(BJ)/QZ4P.

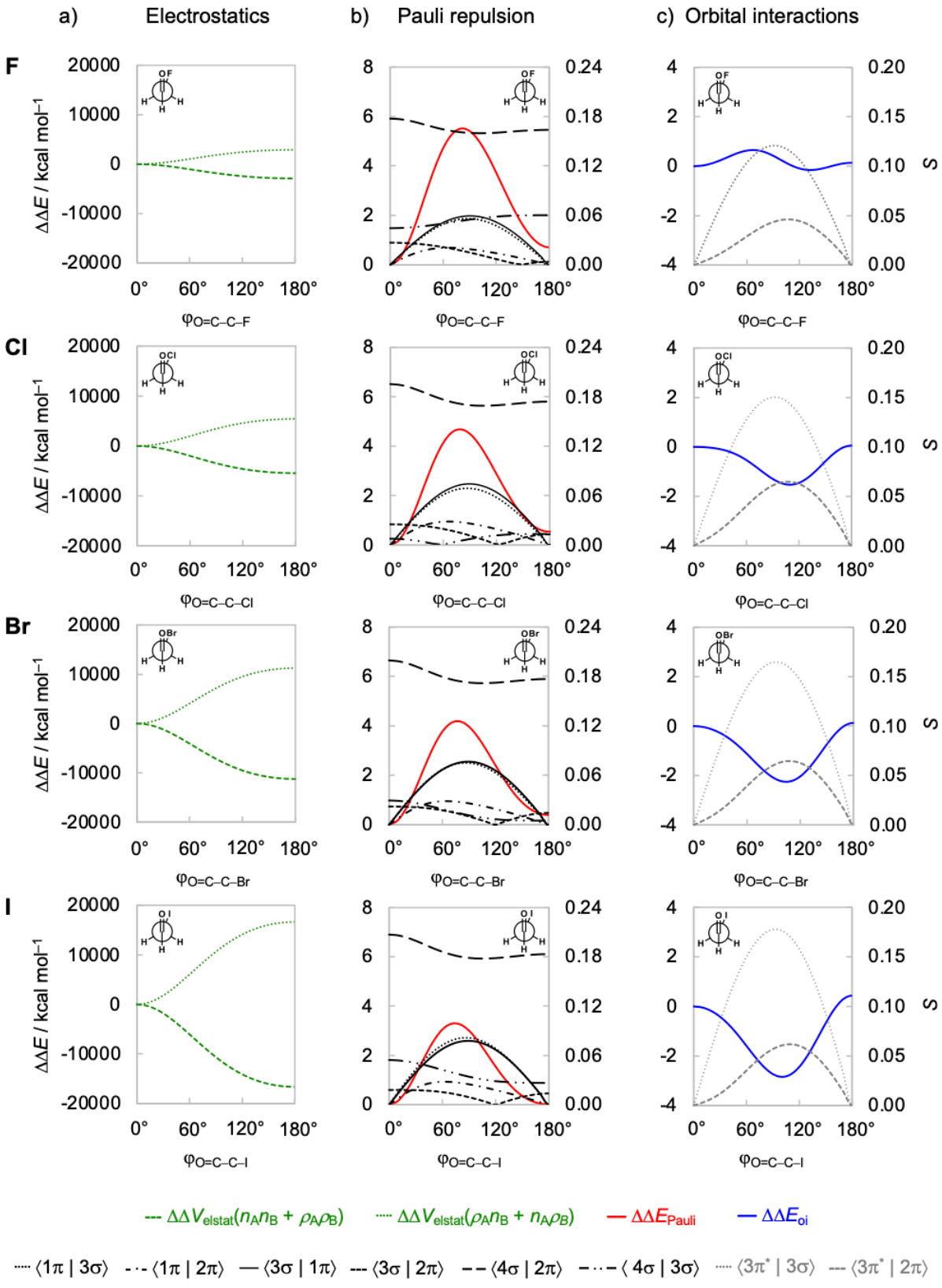

Appendix 5.3: a) Electrostatic interaction energy components, b) Pauli repulsion and key occupied–occupied orbital overlaps, and c) orbital interactions and key unoccupied–occupied orbital overlaps as a function of the $\varphi_{O=C-C-X}$ dihedral angle of haloacetaldehydes OHC–CH_2X (X = F, Cl, Br, and I). Analysis in rigid rotation in *syn* geometry but with C–C distance set to 1.51 Å. Energy terms relative to the *syn* conformer, $\Delta\Delta E$, computed at ZORA-BP86-D3(BJ)/QZ4P.

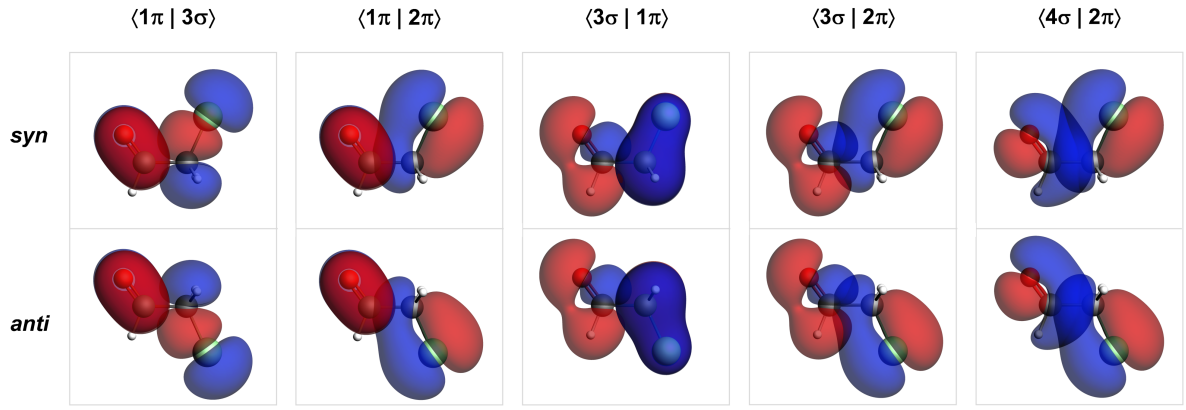

Appendix 5.4: Key closed-shell–closed-shell overlaps between fragment molecular orbitals (FMOs, isosurface at 0.03 a.u.) in the *syn* and *anti*-conformers depicted as quantitative 3D plots for the chloroacetaldehyde analogue. Analysis in rigid rotation in *syn* geometry but with C–C bond distance set to 1.51 Å, computed at ZORA-BP86-D3(BJ)/QZ4P.

Appendix 5.5: Orbital energy gap (in eV) and overlap of key unoccupied–occupied orbital interactions of haloacetaldehydes OHC–CH_2X (X = F, Cl, Br, and I).[a]

	$\varphi_{O=C-C-X} = 90°$ [b]			$\varphi_{O=C-C-X} = 100°$ [b]		
X	$\Delta\varepsilon_{3\pi^*-3\sigma}$ [c]	$\langle 3\pi^*\|3\sigma\rangle$ [c]	$S^2/\Delta\varepsilon$ x 10^3	$\Delta\varepsilon_{3\pi^*-2\pi}$ [c]	$\langle 3\pi^*\|2\pi\rangle$ [c]	$S^2/\Delta\varepsilon$ x 10^3
F	9.9	0.12	1.5	8.2	0.05	0.3
Cl	8.0	0.15	2.8	6.1	0.06	0.6
Br	7.3	0.16	3.5	5.4	0.06	0.7
I	6.5	0.18	5.0	4.7	0.06	0.8

[a] Computed at ZORA-BP86-D3(BJ)/QZ4P. [b] The orientation of the dihedral angle where each interaction is the most stabilizing (where X = F, Cl, Br, and I). [c] The 3π* unoccupied orbital of the $OHC^{\bullet}$ fragment and 3σ and 2π occupied orbitals of the $CH_2X^{\bullet}$ fragment.

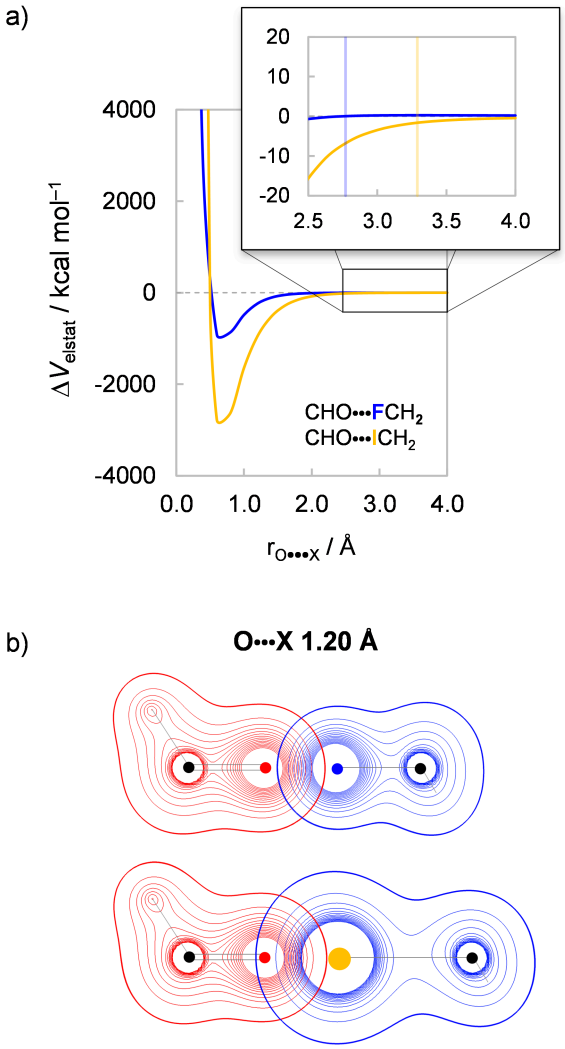

Appendix 5.6: Electrostatic interaction between oxygen and halogen atoms for the C=O•••X–C colinear approach of the OHC• and CH_2X• fragments. a) ΔV_{elstat} as a function of the $r_{O\cdots X}$ distance (vertical lines indicate $r_{O\cdots X}$ separation in the corresponding haloacetaldehyde); b) density contours from –0.9 to 0.9 $Bohr^{-3}$ for OHC• and CH_2X• fragments (X = F, I for upper and lower, resp.). Computed at ZORA-BP86-D3(BJ)/QZ4P.

Appendix 5.7: Orbital energy gap (in eV) and overlap of key unoccupied–occupied orbital interactions of haloacetaldehydes OHC–CH_2X (X = F, Cl, Br, and I).[a]

X	$\Delta\Delta V_{elstat}$	$\Delta\Delta V_{elstat}$ ($n_A n_B$)	$\Delta\Delta V_{elstat}$ ($n_A \rho_B$)	$\Delta\Delta V_{elstat}$ ($\rho_A n_B$)	$\Delta\Delta V_{elstat}$ ($\rho_A \rho_B$)	Δf[b]
F	1.2	1,409.1	–1,430.2	–1,468.5	1,490.5	0.2
Cl	0.5	2,645.3	–2,667.2	–2,767.4	2,789.8	0.0
Br	0.1	5,484.4	–5,510.5	–5,743.0	5,768.9	0.3
I	–0.5	8,114.0	–8,135.8	–8,498.8	8,520.0	0.0

[a] Data from the rigid rotation in *syn* geometry but with C–C distance set to 1.51 Å, computed at ZORA-BP86-D3(BJ)/QZ4P. [b] Fitting for incompleteness.

6 PAPER 4 – LEWIS ACID–BASE PAIRS

Part of this chapter previously appeared as

Nature and Strength of Lewis Acid/Base Interaction in Boron and Nitrogen Trihalides
D. Rodrigues Silva, L. de Azevedo Santos, M. P. Freitas, C. Fonseca Guerra, T. A. Hamlin
Chem Asian J. **2020**, *15*, 4043–4054

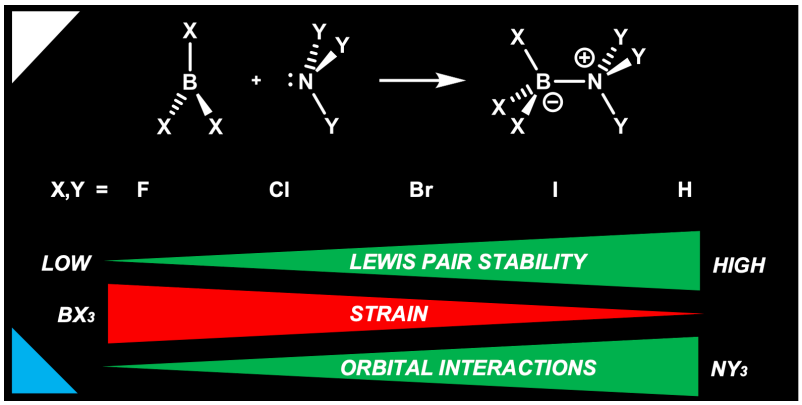

Abstract: We have quantum chemically investigated the bonding between archetypical Lewis acids and bases. Our state-of-the-art computations on the $X_3B–NY_3$ Lewis pairs have revealed the origin behind the systematic increase in B–N bond strength as X and Y are varied from F to Cl, Br, I, H. For $H_3B–NY_3$, the bonding trend is driven by the commonly accepted mechanism of donor–acceptor [HOMO(base)–LUMO(acid)] interaction. Interestingly, for $X_3B–NH_3$, the bonding mechanism is determined by the energy required to deform the BX_3 to the pyramidal geometry it adopts in the adduct. Thus, Lewis acids that can more easily pyramidalize form stronger bonds with Lewis bases. The decrease in the strain energy of pyramidalization on going from BF_3 to BI_3 is directly caused by the weakening of the B–X bond strength, which stems primarily from the bonding in the plane of the molecule (σ-like) and not in the π system, at variance with the currently accepted mechanism.

Keywords: Activation strain analysis, Bond energy, Density functional calculations, Energy decomposition analysis, Lewis acid-base pairs

6.1 Introduction

The chemistry of Lewis acids and bases is rich and can be found in any general chemistry textbook.[1] In his epochal work,[2] Gilbert N. Lewis introduced the concept of electron-pair donor–acceptor complexes, on which the current understanding of Lewis acid/base interactions is based. It defines Lewis acids as chemical species that accepts an electron-pair from a Lewis base to form a Lewis adduct. Thus, the Lewis acidity and basicity scales are associated with the stability of the adducts, that is, relative to a reference, a stronger Lewis acid or Lewis base forms a stronger bounded Lewis complex. The Lewis acid/base chemistry has experienced continuous development since then[3] and has found utility in a wide range of research areas, including catalysis[4] and the recent advent of frustrated Lewis pair chemistry,[5] to name a few.

Due to the ubiquity of Lewis acid/base in chemistry, attempts to rationalize the nature and strength of this interaction abound.[6] The theory of hard and soft acids and bases (HSAB) proposed by Pearson[7] is undoubtedly the most popular qualitative model used to understand this interaction. The HSAB principle uses the intrinsic properties of the interacting species to explain the stability of acid/base complexes, namely, the concept of hardness and softness, which is based on properties such as size, polarizability, and electronegativity. In this model, a hard base (the term "hard" stands for small sized atoms with low polarizability and high electronegativity) would preferentially bind to a hard acid, while a soft base (the term "soft" stands for large sized atoms with high polarizability and low electronegativity) prefers to associate with a soft acid. However, the validity of this model has been questioned, as it has been shown to fail in predicting reactivity of archetypal reactions.[8]

Interestingly, the relative Lewis acidity of boron trihalides with respect to strong bases (*e.g.*, NH_3, NMe_3) is known to increase along the series $BF_3 < BCl_3 < BBr_3$; however, the opposite trend is observed for the interaction with weak bases (*e.g.*, N_2, CH_3F).[6i,9] This indicates that Lewis acid/base is a rather complex interaction that depends on the entire system, not only on the characteristics of the isolated acids and bases. Over the years, various theories have been proposed to explain the trends in stability of Lewis pairs involving boron trihalides, such as those based on π-backdonation,[9c,10] the ability to engage in stabilizing orbital interactions[11] or electrostatics,[9a] ligand close packing (LCP) model,[12] or electrophilicity principle.[13] The decreased Lewis acidity of BF_3 towards strong bases, compared to heavier boron trihalides, is widely attributed to a more efficient π charge donation from the fluorine lone-pair into the empty p orbital of the boron (π-backdonation), which reduces the availability of the boron atom to accept an electron pair from the Lewis base.[9c,10] However, it has been

shown that the p(π)-p(π) overlap integral and the p(π) population at the boron is actually smaller for BF_3 than for BCl_3.[11c,14] Alternatively, an intuitive argument based on the strength of frontier molecular orbital interactions has been proposed by Bessac and Frenking,[11b] that is, the energy of the LUMO of BX_3 decreases from X = F to Cl and results in more stabilizing orbital interactions with the HOMO of the Lewis base for BCl_3 compared to BF_3. We note that these explanations are universal and neither can explain the reversal in Lewis acidities that is observed for the Lewis complexes between boron trihalides and weak bases.

We aim to illuminate the nature and strength of Lewis acid/base interaction within the conceptual framework provided by Kohn-Sham molecular orbital (KS-MO) theory and ultimately provide a unified framework to understand Lewis pairs. To this end, we investigate the underlying physical mechanism behind the formation of a systematic set of $X_3B–NY_3$ Lewis pairs (Scheme 6.1, where X,Y = H, F, Cl, Br, and I). We first explore the archetypical borane–ammonia adduct, $H_3B–NH_3$, and then separately evaluate the substituent effect on the Lewis acid and Lewis base by varying X,Y from H to F, Cl, Br, and I. To the best of our knowledge, this is the first thorough analysis on the formation of Lewis pairs involving the complete series of nitrogen and boron trihalides. Detailed analysis of the electronic structures and bonding mechanisms enable us to interpret our results in quantitative and chemically meaningful terms, which reveals the role of different components, namely, charge–transfer, electrostatic interaction and also strain energy, in the stability of the Lewis complexes. This demonstrates that, similar to hydrogen bonds,[15] Lewis acid/base interaction is a complex interplay of several energy components, whose importance depends on the molecular system and may not be easily captured in simple predictive models.

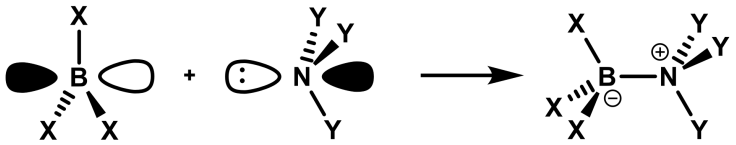

Scheme 6.1: Formation of the Lewis pairs analyzed in this work.

6.2 Methods

Computational Details

All calculations were performed using the Amsterdam Density Functional (ADF) software package.[16] Geometries and energies were calculated at the BLYP level of the generalized

gradient approximation (GGA); exchange functional developed by Becke (B), and the GGA correlation functional developed by Lee, Yang and Parr (LYP).[17] The DFT-D3(BJ) method developed by Grimme and coworkers,[18] which contains the damping function proposed by Becke and Johnson,[19] was used to describe non-local dispersion interactions. Scalar relativistic effects are accounted for using the zeroth-order regular approximation (ZORA).[20] Molecular orbitals (MO) were expanded in a large uncontracted set of Slater type orbitals (STOs) containing diffuse functions: TZ2P.[21] The basis set is of triple-ξ quality for all atoms and has been augmented with two sets of polarization functions. All electrons were included in the variational process, *i.e.*, no frozen core approximation was applied. An auxiliary set of s, p, d, f, and g STOs was used to fit the molecular density and to represent the Coulomb and exchange potentials accurately in each self-consistent field cycle. The accuracies of the fit scheme (ZLM fit)[22] and the integration grid (Becke grid)[23] were set to 'very good'. The Lewis acids were optimized with D_{3h} symmetry constraints, and the Lewis bases and Lewis adducts were optimized with C_{3v} symmetry constraints. All optimized structures were confirmed to be true minima through vibrational analyses[24] (no imaginary frequencies). The molecular structures were illustrated using CYLview.[25]

Activation Strain and Energy Decomposition Analyses

Insight into the nature of Lewis acid/base interactions is obtained by applying the activation strain model (ASM)[26] along the formation of the Lewis adducts. The formation of the Lewis pairs is computationally modelled by decreasing the distance between the boron atom of the Lewis acid and the nitrogen atom of the Lewis base, while other geometry parameters are included in the optimization. Thus, each analysis starts from an optimized Lewis acid and Lewis base at a relatively large distance, then, the B–N distance ($r_{B–N}$) is gradually decreased to a bond length smaller than the equilibrium distance of the Lewis adduct.

The activation strain model of chemical reactivity[26] is a fragment-based approach to understand the energy profile of a chemical process in terms of the original reactants (*i.e.*, the formation of the dimer from monomers). Thus, the overall bond energy $\Delta E(\xi)$ is decomposed into the respective total strain and interaction energy, $\Delta E_{strain}(\xi)$ and $\Delta E_{int}(\xi)$, and project these values onto the reaction coordinate ξ (in this case, $r_{B–N}$) [Eq. (6.1)].

$$\Delta E(\xi) = \Delta E_{strain}(\xi) + \Delta E_{int}(\xi) \quad (6.1)$$

The total strain energy can, in turn, be further decomposed into the strain energies corresponding to the deformation of the Lewis acid $\Delta E_{\text{strain,BX}_3}(\xi)$ as well as from the Lewis base $\Delta E_{\text{strain,NY}_3}(\xi)$ [Eq. (6.2)]. The interaction energy between the deformed fragments is further analyzed in terms of quantitative Kohn-Sham molecular orbital (KS-MO) theory in combination with a canonical energy decomposition analysis (EDA).[27] The EDA decomposes the $\Delta E_{\text{int}}(\xi)$ into four physically meaningful energy terms [Eq. (6.3)]: electrostatic interaction $\Delta V_{\text{elstat}}(\xi)$, Pauli repulsion $\Delta E_{\text{Pauli}}(\xi)$, orbital interactions $\Delta E_{\text{oi}}(\xi)$, and dispersion energy $\Delta E_{\text{disp}}(\xi)$. The $\Delta E_{\text{oi}}(\xi)$ term can be decomposed into the contributions from each irreducible representation Γ of the interacting system [Eq. (6.4)]. A detailed, step-by-step, guide on how to perform and interpret the ASM and EDA can be found in reference 26a and a theoretical overview is given in Chapter 2.5. The Pyfrag program was used to facilitate these analyses.[28]

$$\Delta E_{\text{strain}}(\xi) = \Delta E_{\text{strain,BX}_3}(\xi) + \Delta E_{\text{strain,NY}_3}(\xi) \tag{6.2}$$

$$\Delta E_{\text{int}}(\xi) = \Delta V_{\text{elstat}}(\xi) + \Delta E_{\text{Pauli}}(\xi) + \Delta E_{\text{oi}}(\xi) + \Delta E_{\text{disp}}(\xi) \tag{6.3}$$

$$\Delta E_{\text{oi}} = \sum_{\Gamma} \Delta E_{\Gamma} \tag{6.4}$$

Voronoi Deformation Density (VDD) charges

The atomic charge distribution was analyzed by using the Voronoi Deformation Density (VDD) method.[29] The VDD method partitions the space into so-called Voronoi cells, which are non-overlapping regions of space that are closer to nucleus A than to any other nucleus. The charge distribution is determined by taking a fictitious promolecule as reference point, in which the electron density is simply the superposition of the spherical atomic densities. The change in density in the Voronoi cell when going from this promolecule to the final molecular density of the interacting system is associated with the VDD atomic charge Q. Thus, the VDD atomic charge $Q_{\text{A}}^{\text{VDD}}$ of atom A is given by:

$$Q_{\text{A}}^{\text{VDD}} = -\int_{\text{Voronoi cell of A}} \left[\rho(\text{r}) - \rho_{\text{promolecule}}(\text{r})\right] \text{dr} \tag{6.5}$$

Instead of computing the amount of charge contained in an atomic volume, we compute the flow of charge from one atom to the other upon formation of the molecule. The physical interpretation is therefore straightforward. A positive atomic charge Q_{A} corresponds to the loss

of electrons, whereas a negative atomic charge Q_A is associated with the gain of electrons in the Voronoi cell of atom A.

Thermochemistry

Bond enthalpies at 298.15 K and 1 atm ($\Delta H_{298.15}$) were calculated from electronic bond energies (ΔE) and vibrational frequencies using standard thermochemistry relations for an ideal gas [Eq. (6.7)].[30]

$$\Delta H_{298.15} = \Delta E + \Delta E_{trans,298.15} + \Delta E_{rot,298.15} + \Delta E_{vib,0} + \Delta(\Delta E_{vib,0})_{298.15} + \Delta(pV) \qquad (6.6)$$

Here, $\Delta E_{trans,298.15}$, $\Delta E_{rot,298.15}$, and $\Delta E_{vib,0}$ are the differences between the Lewis pair minus the isolated Lewis acid and base, that results from forming the B–N bond, in translational, rotational, and zero-point vibrational energy, respectively. The last term, $\Delta(\Delta E_{vib,0})_{298.15}$, is the change in the vibrational energy difference when going from 0 K to 298.15 K. The vibrational energy corrections are based on our frequency calculations. The molar work term $\Delta(pV)$ is $(\Delta n)RT$; $\Delta n = -1$ for two fragments BX_3 and NY_3 combining to one molecule $X_3B–NY_3$. Thermal corrections for the electronic energy are neglected.

6.3 Results and Discussion

Structures and Bond Strengths

In this section, the geometries and bond energies of the $X_3B–NY_3$ Lewis pairs (X,Y = H, F, Cl, Br, and I) are discussed. The results are summarized in Figure 6.1. As BX_3 and NY_3 approach each other to form the Lewis adduct, the Lewis acid must pyramidalize from its trigonal planar equilibrium geometry, that is, the $\theta_{X–B–X}$ angle decreases and the $r_{B–X}$ bond length increases. This effect is much less pronounced in the Lewis base, as it already has a pyramidal equilibrium geometry and undergoes almost no deformation upon complexation. Our computed bond lengths and angles of borane–ammonia (*i.e.*, $H_3B–NH_3$) are in very good agreement with existing experimental data[31] (in parenthesis): $r_{B–N}$ bond length of 1.675 Å (1.657 Å), $r_{B–H}$ bond length of 1.211 Å (1.216 Å), $r_{N–H}$ bond length of 1.022 Å (1.014 Å), $\theta_{H–B–H}$ angle of 113.8° (113.8°), and $\theta_{H–N–H}$ angle of 107.8° (108.7°).

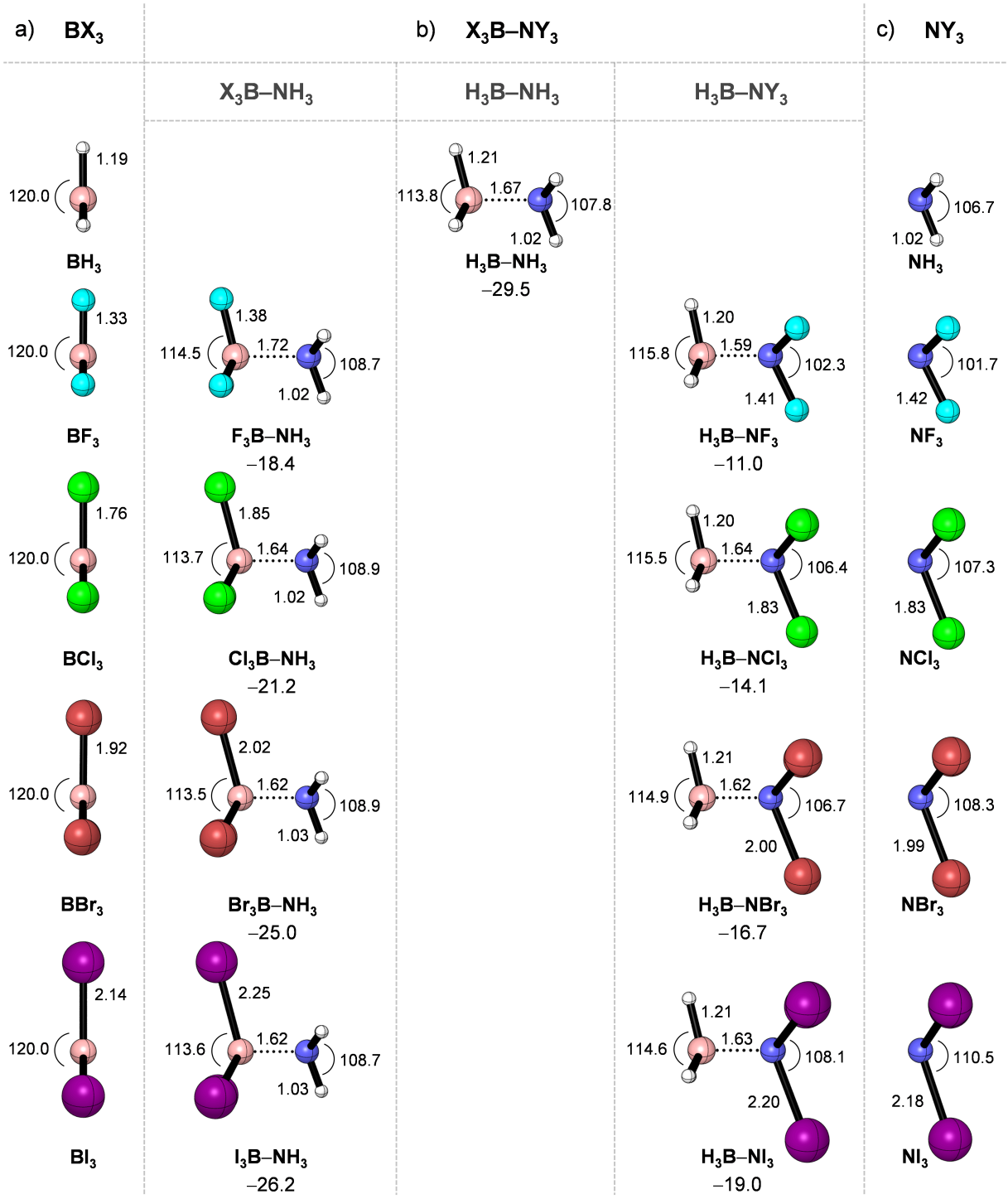

Figure 6.1: Equilibrium geometries (in Å, deg.) of the a) BX_3 Lewis acids, b) $X_3B–NY_3$ Lewis adducts, and c) NY_3 Lewis bases (X,Y = H, F, Cl, Br, and I), along with the electronic bond energies ΔE (in kcal mol^{-1}) computed at ZORA-BLYP-D3(BJ)/TZ2P.

The expected trends in Lewis adduct stabilities are nicely reproduced by our DFT computations at ZORA-BLYP-D3(BJ)/TZ2P. Borane–ammonia forms the strongest bond complex in our series of Lewis pairs (ΔE = –29.5 kcal mol^{-1}). Upon substitution of the hydrogen

atoms on the Lewis acid or Lewis base with halogen atoms, the energy of formation of the Lewis adduct ΔE decreases in strength, *i.e.*, becomes less stabilizing, along the series: H, I, Br, Cl, F. The bond enthalpies at 298 K ($\Delta H_{298.15}$) show the same trends as the electronic bond energies ΔE (Appendix 6.1). In the following sections, we partition the Lewis pairs into three sets: 1) $H_3B–NH_3$, 2) $X_3B–NH_3$, and 3) $H_3B–NY_3$ (where X,Y = F, Cl, Br, and I), and provide a unified model to rationalize the strength of the Lewis pair bond through detailed analyses of the electronic structure and bonding mechanism.

Borane–ammonia

The activation strain model and energy decomposition analysis diagrams of the borane–ammonia adduct are shown in Figure 6.2. From Figure 6.2a, it can be easily seen that the energy profile in ΔE curve along the newly forming B–N bond is determined by the interaction energy ΔE_{int}, which becomes destabilizing only at very short B–N bond distance (smaller than $r_{B–N} <$ 1.23 Å). The strain energy ΔE_{strain}, on the other hand, becomes increasingly destabilizing as the internuclear distance decreases. The destabilizing ΔE_{strain} stems mostly from the deformation of the Lewis acid, BH_3, from its planar equilibrium geometry to the pyramidal geometry it adopts in the complex. Note that the BH_3 strain energy curve $\Delta E_{strain,BH_3}$ coincides with the total strain energy curve ΔE_{strain}, whereas the NH_3 strain energy curve $\Delta E_{strain,NH_3}$ is flat all along the reaction coordinate.

Since the interaction energy plays a critical role on the formation of the $H_3B–NH_3$ Lewis pair, we further decomposed ΔE_{int} into four physically meaningful terms according to Eq. (6.3). The results of this energy decomposition analysis (EDA) are shown in Figure 6.2b. This graph shows us a quite straightforward picture. The ΔE_{int} is equally stabilized by orbital and electrostatic interactions, the ΔE_{oi} and ΔV_{elstat} curves nearly coincide at all B–N bond distances shown. Both terms become more stabilizing as the fragment separation decreases and the bond begins to form, because of the increase in both HOMO–LUMO orbital overlap and charge penetration of nuclei with electron clouds. The stabilizing effect of ΔE_{oi} and ΔV_{elstat} is, however, opposed by the Pauli repulsion ΔE_{Pauli} term. Note that at a B–N separation shorter than the equilibrium bond length, the upward slope of the ΔE_{Pauli} curve is larger than the downward slope of the ΔE_{oi} and ΔV_{elstat} curves, which is the reason behind the destabilization of ΔE_{int} at short internuclear distance.[32] The dispersion energy ΔE_{disp}, on the other hand, remains nearly constant at any point along $r_{B–N}$.

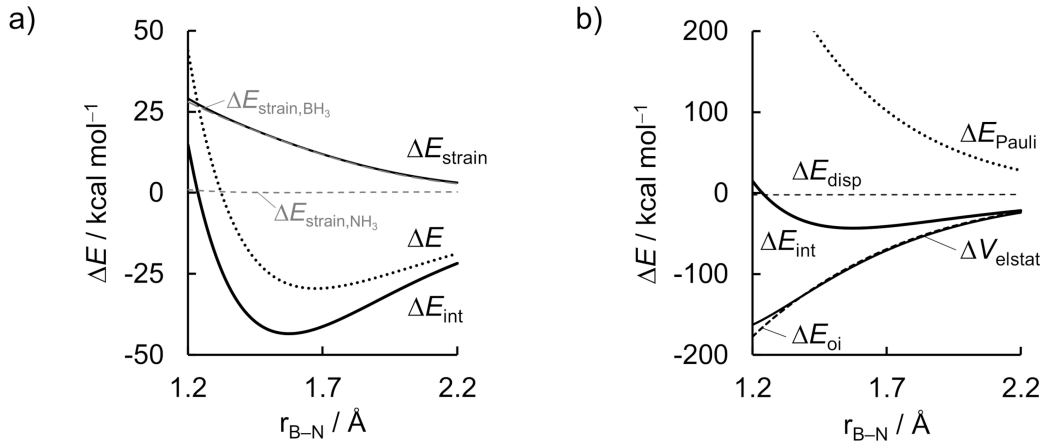

c)

ΔE	ΔE_{strain}	$\Delta E_{strain,BH_3}$	$\Delta E_{strain,NH_3}$	ΔE_{int}	ΔV_{elstat}	ΔE_{Pauli}	ΔE_{oi}	ΔE_{disp}
–29.5	12.2	12.1	0.1	–41.7	–73.0	104.8	–71.1	–2.4

Figure 6.2: a) Activation strain model and b) energy decomposition analysis of the $H_3B–NH_3$ Lewis pair projected onto the forming B–N bond distance, and c) data (in kcal mol^{-1}) at consistent geometry with a B–N distance of 1.687 Å. Computed at ZORA-BLYP-D3(BJ)/TZ2P.

Thus, electrostatic and orbital interactions are the main contributors to the formation of the $H_3B–NH_3$ Lewis pair. To understand the origin of the stabilizing ΔE_{oi} and ΔV_{elstat}, we have analyzed the molecular orbital (MO) diagram of the fragment molecular orbitals (FMOs) and the electrostatic potential surface of each fragment, respectively.[26a] To ensure that our results are not skewed by the fact that the Lewis adducts have different equilibrium bond lengths, analysis of all Lewis pairs will be performed at the same $r_{B–N}$ distance of 1.687 Å, near to the equilibrium bond distance of borane–ammonia. Energies at consistent geometry for the $H_3B–NH_3$ adduct are shown in Figure 6.2c.

Figure 6.3a shows that ΔE_{oi} can be rationalized in terms of the well-known [HOMO(base)–LUMO(acid)] interaction between the filled N $2p_z$ orbital of the Lewis base with the empty B $2p_z$ orbital of the Lewis acid (see Figure 6.3b). This interaction has favorable orbital energy gap ($\Delta\varepsilon$ = 2.5 eV) and overlap ($\langle$HOMO|LUMO$\rangle$ = 0.36).[33] Furthermore, inspection of the electrostatic potential surfaces illustrated in Figure 6.3c and atomic charges in Figure 6.3d reveals that accumulation of positive charge around the boron atom of the electron-deficient Lewis acid and negative charge around the nitrogen atom of the electron-rich Lewis base are responsible for the stabilizing ΔV_{elstat}.

In summary, the EDA along the forming $H_3B–NH_3$ Lewis pair demonstrates that the attractive interaction between the BH_3 Lewis acid and the NH_3 Lewis base has a stabilizing

covalent character that is the same magnitude as the electrostatic character, both can be easily understood in terms of simple chemical arguments. Our results, so far, conform to and agree with the current picture presented in the literature.[6d,e,i] In the coming next sections, we extend our analysis to study the stability of Lewis adducts of halogenated Lewis acids and Lewis bases.

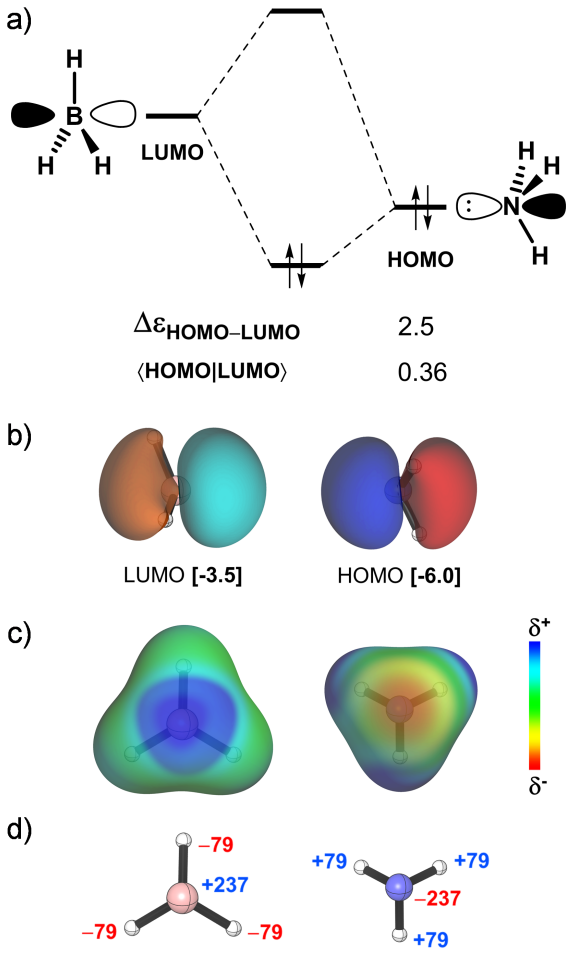

Figure 6.3: a) MO diagram along with the orbital energy gap (in eV) and overlap of the $HOMO_{(base)}$–$LUMO_{(acid)}$ interaction in the H_3B–NH_3 Lewis pair, b) isosurface (at 0.05 au) and energy (in eV) of the HOMO and LUMO orbitals of the a_1 irreducible representation of the C_{3v} symmetry, c) electrostatic potential surfaces (at 0.01 au) from –0.1 (red) to 0.1 (blue) au and d) VDD atomic charges (in milli-electrons). Computed at consistent geometry with a B–N bond distance of 1.687 Å at ZORA-BLYP-D3(BJ)/TZ2P.

Halogenated Lewis Acids

Next, we turn to the analysis of the formation of the Lewis pairs between boron trihalides and ammonia. The activation strain model and energy decomposition analysis diagrams for the X_3B–NH_3 Lewis pairs (where X = F, Cl, Br, and I) are shown in Figure 6.4. In line with the

expected Lewis acidities,[9c] BI_3 forms the strongest complex with ammonia and the energy of formation of the Lewis adduct ΔE decreases in strength, *i.e.*, becomes less stabilizing, along the series: BI_3, BBr_3, BCl_3, BF_3. However, in contrast with the commonly accepted view of Lewis acid/base interaction, the stronger bond energy does not originate from the more stabilizing interaction energy, but from the *less destabilizing strain energy*.[12a,34] In general, ΔE_{strain} is less destabilizing for the Lewis complex involving BI_3 and becomes increasingly destabilizing along the series $BI_3 < BBr_3 < BCl_3 < BF_3$. On the other hand, ΔE_{int} is nearly the same for all Lewis adducts and does not follow a systematic trend. If covalent interactions would be the decisive factor for the observed Lewis pair stabilities, one would expect that the trend in ΔE_{int} along the boron trihalides also holds for the trend in ΔE; but this is not the case. We discuss these findings in more details below.

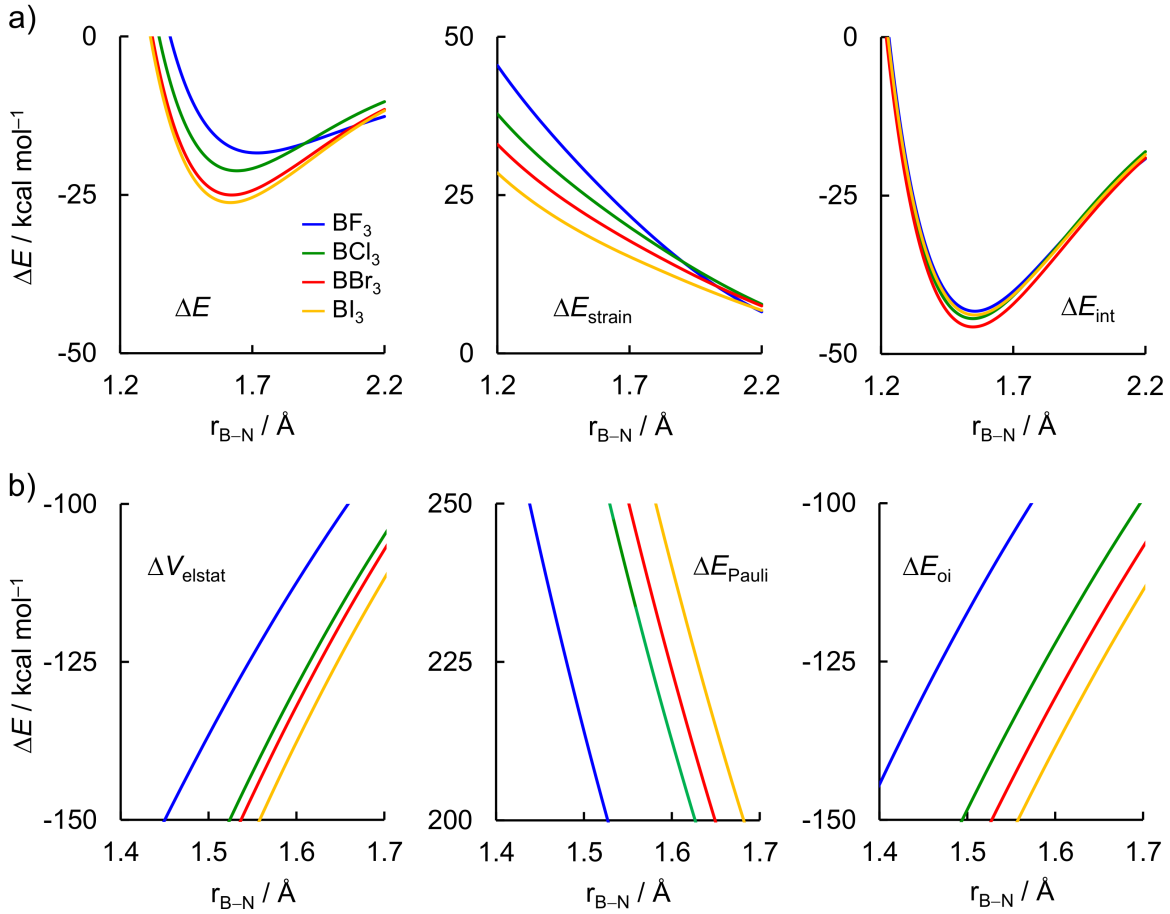

Figure 6.4: a) Activation strain model and b) energy decomposition analysis of the $X_3B–NH_3$ Lewis pairs projected onto the forming B–N bond distance (where X = F, Cl, Br, and I) computed at ZORA-BLYP-D3(BJ)/TZ2P. Dispersion energy ΔE_{disp} not shown, see Appendix 6.2 for data at consistent geometries.

The same conclusion can be drawn at consistent geometries ($r_{B–N}$ = 1.687 Å, see Table 6.1; the EDA data is given in Appendix 6.2). The values of ΔE_{int} are of the same order of magnitude as in borane–ammonia, *ca.* 41 kcal mol^{-1}, while the ΔE_{strain} is significantly larger for the boron trihalides and accounts for 12.2 and 22.3 kcal mol^{-1} for $H_3B–NH_3$ and $F_3B–NH_3$, respectively. The ΔE_{strain} results predominantly from the deformation of the Lewis acid $\Delta E_{strain,BX_3}$. Nevertheless, there is no clear correlation of $\Delta E_{strain,BX_3}$ with any geometrical change. The pyramidalization angle $\Delta\theta_{pyr,BX_3}$ is very similar for all Lewis acids and the B–X bond stretching $\Delta r_{B–X}$ has a reversed trend that from $\Delta E_{strain,BX_3}$, *i.e.*, the $\Delta r_{B–X}$ increases as X goes from F to I (see Table 6.1).

Table 6.1: Activation strain model terms (in kcal mol^{-1}), bond stretching (in Å) and pyramidalization angle (in degrees) computed at consistent geometries with a B–N distance of 1.687 Å of the $X_3B–NH_3$ Lewis pairs (where X = F, Cl, Br, and I).[a]

Lewis acid	$\Delta r_{B–X}$	$\Delta r_{N–H}$	$\Delta\theta_{pyr,BX_3}$ [b]	$\Delta\theta_{pyr,NH_3}$ [b]	ΔE	ΔE_{int}	ΔE_{strain}	$\Delta E_{strain,BX_3}$
BF_3	0.060	0.001	–17.2	5.7	–18.3	–40.6	22.3	22.2
BCl_3	0.089	0.002	–18.0	7.4	–21.0	–41.3	20.3	20.1
BBr_3	0.096	0.003	–18.0	7.7	–24.5	–42.6	18.1	17.8
BI_3	0.103	0.004	–17.6	7.5	–25.6	–41.2	15.5	15.3

[a] Computed at ZORA-BLYP-D3(BJ)/TZ2P, geometrical data relative to the separate reactants. [b] Pyramidalization angle defined as the sum of the three $\theta_{X–B–X}$ and $\theta_{H–N–H}$ angles for BX_3 and NH_3, respectively.

In order to pinpoint the origin of the observed strain energy of the boron trihalides, we have carried out a subsequent analysis on the BX_3 fragment. This time we decompose the $\Delta E_{strain,BX_3}$ term into the individual strain energies associated with the bending of the $\theta_{X–B–X}$ angle ($\Delta E_{strain,\theta}$) and the B–X bond stretch ($\Delta E_{strain,r}$), as schematically illustrated in Table 6.2. First, the BX_3 is pyramidalized with a fixed $r_{B–X}$, taken from the respective planar equilibrium geometry, and, next, the $r_{B–X}$ bond is allowed to relax to the one it has in the consistent geometry of the Lewis pair. The energy associated with each geometrical deformation is presented in Table 6.2. The majority of the strain energy originates from the bending of the $\theta_{X–B–X}$ angle and the trends in $\Delta E_{strain,\theta}$ follow exactly the trends of the total strain of the Lewis acid $\Delta E_{strain,BX_3}$, that is, it is larger for BF_3 and smaller for BI_3. The same trend can be observed if we analyze the other way around, first elongation of the $r_{B–X}$ bond and then bending of the $\theta_{X–B–X}$ angle.

Yet, the pyramidalization angle is similar for all boron trihalides. Why then does BX_3 become easier to bend to the same extent along the series X = F, Cl, Br, I?

To answer to this question, we must understand exactly how the electronic structure of the Lewis acid changes upon pyramidalization (that is, bending and elongation). The rise in energy associated with the deformation of BX_3 (*i.e.*, $\Delta E_{strain,BX_3}$) could stem from two distinct factors: i) the bonding between central boron and halogen ligands becomes less stabilizing in the pyramidal geometry; and ii) there is an increase in the repulsion among the halogens as BX_3 deforms.[35] Therefore, we have further decomposed the $\Delta E_{strain,BX_3}$ in terms of the interaction energy between B and X_3 ($\Delta E_{int,B–X_3}$) and among the three X ($\Delta E_{int,X–X–X}$), more specifically, in terms of the change in both energy terms as BX_3 deforms from the planar to the pyramidal geometry (see Table 6.3).

Table 6.2: The strain energy terms (in kcal mol^{-1}) associated with the step-by-step deformation of the Lewis acid from the planar to the pyramidal geometry.[a]

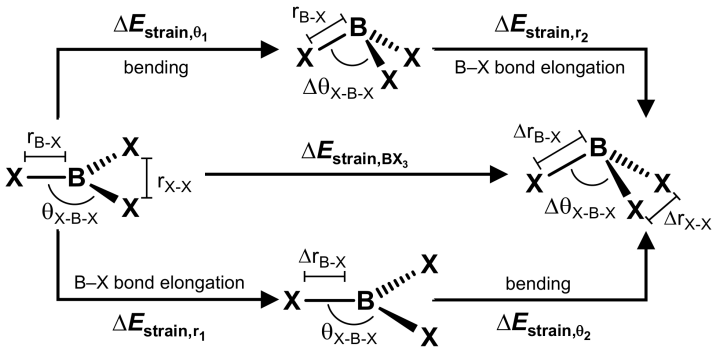

Lewis acid	$\Delta E_{strain,\theta_1}$	$\Delta E_{strain,r_2}$	$\Delta E_{strain,r_1}$	$\Delta E_{strain,\theta_2}$	$\Delta E_{strain,BX_3}$	$\Delta r_{X–X}$
BF_3	19.1	3.1	5.5	16.7	22.2	0.032
BCl_3	16.7	3.4	6.2	13.9	20.1	0.053
BBr_3	14.9	2.9	5.6	12.2	17.8	0.056
BI_3	12.8	2.5	4.9	10.4	15.3	0.057

[a] Geometry adopted in the complex with a B–N distance of 1.687 Å of the $X_3B–NH_3$ Lewis pairs (where X = F, Cl, Br, and I), computed at ZORA-BLYP-D3(BJ)/TZ2P.

Put simply, the interaction energy $\Delta E_{int,X–X–X}$ corresponds to the formation of the $(X^{\bullet})_3$ fragment in its quartet valence configuration and in the geometry which it acquires in the overall molecule, and the interaction energy $\Delta E_{int,B–X_3}$ corresponds to the actual energy change when the prepared B-sp^2 and $(X^{\bullet})_3$ fragments are combined to form the BX_3 (planar or pyramidal).

As BX_3 goes from one geometry to the other, the change in interaction energy is written as $\Delta\Delta E_{int}$. Thus, the $\Delta\Delta E_{int,X–X–X}$ and $\Delta\Delta E_{int,B–X_3}$ are, respectively, the change in both interaction energy terms when BX_3 goes from the planar to the pyramidal geometry and sum to $\Delta E_{strain,BX_3}$ (see Table 6.3). Here, positive values of $\Delta\Delta E_{int}$ indicate that the interaction energy opposes pyramidalization, while negative values indicate that it favors pyramidalization of the Lewis acid.

Table 6.3: Change in the energy decomposition analysis terms (in kcal mol^{-1}) associated with the deformation of the BX_3 Lewis acids from the planar to the pyramidal geometry[a] (where X = F, Cl, Br, and I).[b]

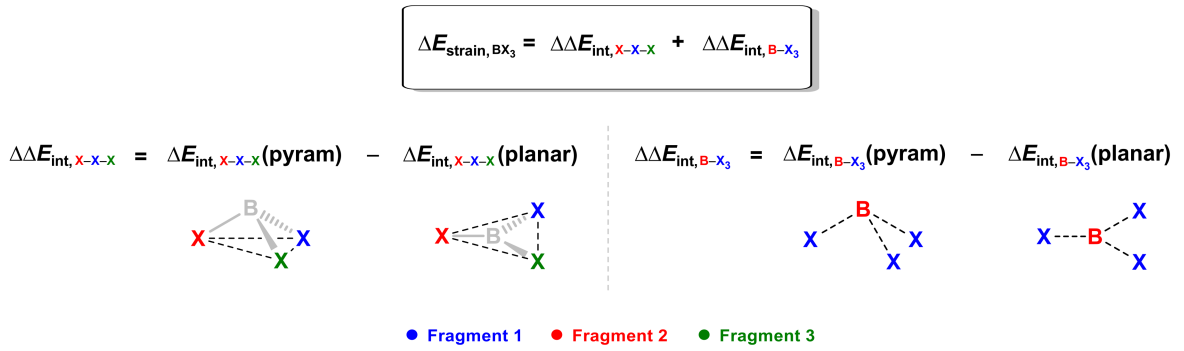

Lewis acid	$\Delta\Delta E_{int,X–X–X}$	$\Delta\Delta E_{int,B–X_3}$	$\Delta\Delta V_{elstat,B–X_3}$	$\Delta\Delta E_{Pauli,B–X_3}$	$\Delta\Delta E_{oi,B–X_3}$	$\Delta\Delta E_{oi,a_1}$	$\Delta\Delta E_{oi,e_1}$	$\Delta\Delta E_{oi,a_2}$
BF_3	–4.8	27.0	74.7	–142.5	94.7	27.1	67.1	0.5
BCl_3	–6.5	26.6	95.8	–126.0	56.8	13.5	43.0	0.3
BBr_3	–5.7	23.5	102.5	–122.0	43.1	8.5	34.4	0.2
BI_3	–5.1	20.4	99.3	–112.1	33.2	5.8	27.3	0.1

[a] Geometry adopted in the complex with a B–N distance of 1.687 Å of the $X_3B–NH_3$ Lewis pairs. [b] Computed at ZORA-BLYP-D3(BJ)/TZ2P.

The most striking result in Table 6.3 is that the interaction energy between the halogens, which is predominantly repulsive (see Appendix 6.3), becomes less destabilizing in the pyramidal geometry (*i.e.*, $\Delta\Delta E_{int,X–X–X}$ is negative) and, thus, favors the pyramidalization of the Lewis acid. This is because when the $r_{B–X}$ bond elongates, the halogens are actually farther removed from each other in the pyramidal than in the planar geometry (see $\Delta r_{X–X}$ in Table 6.2). This means that $\Delta\Delta E_{int,B–X_3}$ determines the trends in $\Delta E_{strain,BX_3}$, as clearly observed from Table 6.3. Along X = F to I, $\Delta E_{strain,BX_3}$ varies from 22.2 to 15.3 kcal mol^{-1} and $\Delta\Delta E_{int,B–X_3}$ varies from 27.0 to 20.4 kcal mol^{-1}. The interaction energy between the boron and the halogens is less

stabilizing in the pyramidal than in the planar geometry (*i.e.*, $\Delta\Delta E_{int,B-X_3}$ is positive) and, thus, opposes the pyramidalization of the Lewis acid. This loss in stabilization correlates to the difficulty to pyramidalize the Lewis acid, that is, a larger $\Delta\Delta E_{int,B-X_3}$ translates in to a larger $\Delta E_{strain,BX_3}$.

To obtain insight into the different contributors to the interaction energy we have again employed the EDA scheme[27] (see Table 6.3, full data is provided in Appendix 6.3). It can be seen that the trend in $\Delta\Delta E_{int,B-X_3}$ is dictated by the orbital interactions $\Delta\Delta E_{oi,B-X_3}$. Both $\Delta\Delta E_{int,B-X_3}$ and $\Delta\Delta E_{oi,B-X_3}$ oppose pyramidalization of the Lewis acid (*i.e.*, they are positive) and decrease in magnitude from BF_3 to BI_3. Along X = F to I, $\Delta\Delta E_{oi,B-X_3}$ varies from a value of 94.7 to 33.2 kcal mol^{-1}. Note that the electrostatic interaction also opposes pyramidalization (*i.e.*, positive values of $\Delta\Delta V_{elstat,B-X_3}$) but it increases from BF_3 to BI_3, therefore, not following the trend in $\Delta\Delta E_{int,B-X_3}$. Interestingly, the Pauli repulsion term favors pyramidalization (*i.e.*, negative values of $\Delta\Delta E_{Pauli,B-X_3}$) because it goes with an elongation of the r_{B-X} bond in the pyramidal geometry, which becomes longer from BF_3 to BI_3. Therefore, in a sense, $\Delta\Delta V_{elstat,B-X_3}$ and $\Delta\Delta E_{Pauli,B-X_3}$ work together against the observed trend in $\Delta\Delta E_{int,B-X_3}$. Finally, the dispersion term, $\Delta\Delta E_{disp,B-X_3}$, is the same at both geometries (*i.e.*, $\Delta\Delta E_{int,B-X_3}$ = 0.0 and is not provided in Table 6.3).

Figure 6.5 shows the MO diagram of the main orbital interactions between $(X^{\bullet})_3$ and B-sp^2 in the e_1 and a_1 representations (the complete MO diagram with all valence orbitals is provided in Appendix 6.4). We now address why the covalent component of the interaction between B and X_3 is less stabilizing in the pyramidal geometry, that is, $\Delta\Delta E_{oi,B-X_3}$ is positive, and how it determines the trend in $\Delta E_{strain,BX_3}$. Most of this effect originates from the orbital interactions in the e_1 irreducible representation (see Table 6.3), which corresponds to the bonding in the plane of the molecule (σ-like bonding). Interestingly, the total stabilizing orbital interactions $\Delta E_{oi,B-X_3}$ is provided by nearly 70% $\Delta E_{oi,e_1}$ and 30% $\Delta E_{oi,a_1}$ (the contribution from $\Delta E_{oi,a_2}$ is very small, see Appendix 6.3). This is in contrast to the common belief that the strength of the B–X bond arises from the overlap in the π system (*i.e.*, in the a_1 representation), between the filled np_z orbitals of the halogens and the empty p_z orbital of boron.[9c]

In planar BX_3 (Figure 6.5a left), two electron pair bonds are formed in the e_1 irreducible representation ($ne_1 \pm 2p_x$ and $ne_1 \pm 2p_y$), where ne_1 is a combination of the np orbitals in the xy plane of the halogen atoms. The degenerated singly occupied ne_1 orbitals show the well-known increase in energy on descending group 17 in the periodic table,[36] from –12.7 to –8.0 eV as X

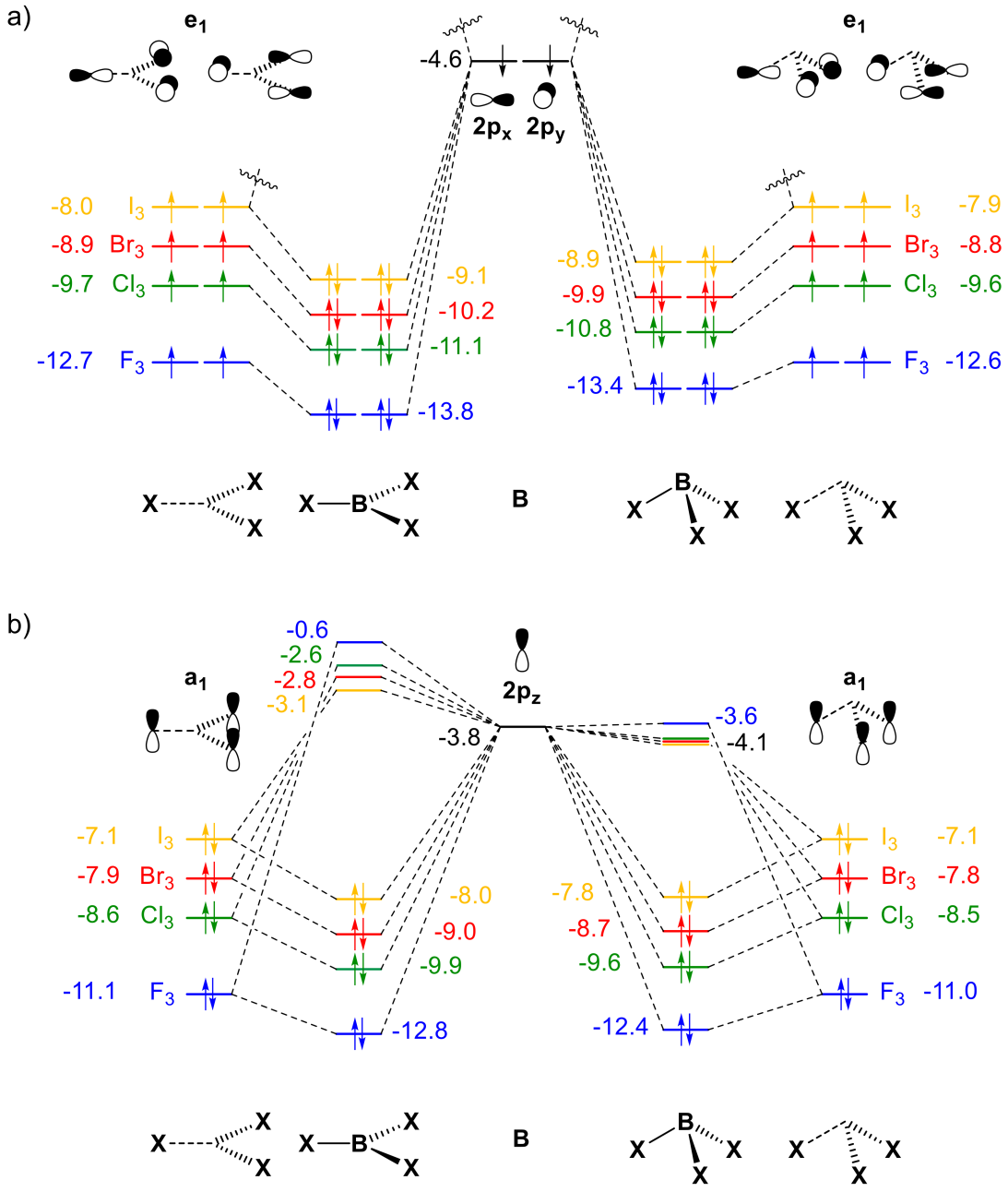

Figure 6.5: Orbital interaction scheme for planar and pyramidal BX_3 (where X = F, Cl, Br, and I) in the a) e_1 and b) a_1 irreducible representations of the C_{3v} symmetry computed at ZORA-BLYP-D3(BJ)/TZ2P.

goes from F to I, associated with the decreasing electronegativity of X.[37] As the fragments combine to form BX_3, the electrons are stabilized in the bonding molecular orbitals and this stabilization correlates well with the energy of the $(X^{\bullet})_3$ fragment orbitals, in line with the order of strength of the B–X bond.[38] Upon pyramidalization, there is a decrease in the orbital overlap between ne_1 and $2p_{x,y}$ for all BX_3 (see Appendix 6.3), resulting in the less stabilizing $\Delta\Delta E_{oi,B-X_3}$. Furthermore, pyramidalization also results in destabilization of the ne_1 orbitals of the $(X^{\bullet})_3$

fragment and, most important, in the bonding molecular orbitals of BX_3 (Figure 6.5a right). Interestingly, the destabilization of the bonding molecular orbitals shows the same trend as the $\Delta E_{\text{strain,BX}_3}$, that is, it decreases along the series X = F, Cl, Br, I ($\Delta\varepsilon$ = 0.4, 0.3, 0.3, and 0.2 eV for BF_3, BCl_3, BBr_3, and BI_3, respectively). Similar effect occurs for orbital interactions in the a_1 representation (see Figure 6.5b). Thus, as the boron trihalides deform to the same extent, the destabilization in the molecular orbitals of BF_3 is larger. The $(F^{\bullet})_3$ is more strongly bound to the central boron atom, therefore, the decrease in the strain energy from BF_3 to BI_3 can be ascribed to the amount of energy required to distort a weaker bond. In other words, it requires less energy to deform BI_3 than BF_3 because the B–I bond is weaker than the B–F bond.

At last, we comment on the role of the orbital interactions between the Lewis acid and the Lewis base to the stability of the $X_3B–NH_3$ Lewis pairs (where X = F, Cl, Br, and I), which is the widely accepted rationale to explain the Lewis acidity of boron trihalides.[11] Our EDA results (Figure 6.4b and Appendix 6.2), indeed, demonstrate that ΔE_{oi} follows the trend in ΔE, that is, it becomes more stabilizing from $F_3B–NH_3$ to $I_3B–NH_3$. The trends in ΔE_{oi} can be ascribed to the energy of the LUMO of BX_3 that decreases in energy from BF_3 to BI_3 (see Figure 6.5b), resulting in more stabilizing orbital interactions, in line with the results by Bessac and Frenking.[11b] However, the stabilizing effect of ΔE_{oi} (and also ΔV_{elstat}) is counteracted by a strong Pauli repulsion ΔE_{Pauli} that leads to a similar ΔE_{int} for all Lewis adducts (see Figure 6.4b). We again emphasize that it is crucial to compare the Lewis adducts at a consistent geometry, that is, the same $r_{\text{B–N}}$ bond length, because the energy components are highly dependent on the bond distance.[26a] Data at the equilibrium geometries (Appendix 6.1) shows that the strain energy of BF_3 is smaller than BCl_3, but this is just because of the longer $r_{\text{B–N}}$ bond distance in the Lewis pair with the former. Analysis at the consistent geometries (Table 6.1) shows that the trends in bond energy ΔE can solely be assigned to the strain energy of the Lewis acid $\Delta E_{\text{strain,BX}_3}$; not to the interaction energy ΔE_{int}.

We conclude that the more destabilizing strain energy along the series $BI_3 < BBr_3 < BCl_3 < BF_3$, leads to less stable $X_3B–NH_3$ Lewis pairs (where X = F, Cl, Br, and I), due to a loss in stabilization of the bonding interactions between the central boron and the halogen ligands as the BX_3 goes from the planar to the pyramidal geometry. This effect is most pronounced for BF_3 because the B–F bond is the strongest in our series of boron trihalides. These general observations also explain why a reversed trend is observed for the interaction of boron trihalides with weak bases:[9] weak bases induce small distortion of BX_3 from its planar equilibrium geometry that allows the interaction energy to dominate and govern the bonding of these Lewis pairs.

Halogenated Lewis Bases

Finally, we turn our attention to the formation of Lewis adducts between borane and nitrogen trihalides. The activation strain model and energy decomposition analysis diagrams for the $H_3B–NY_3$ Lewis pairs (where Y = F, Cl, Br, and I) are shown in Figure 6.6, whereas data at consistent geometries is summarized in Table 6.4. The NI_3 forms the strongest complex with borane and the energy of formation of the Lewis adduct ΔE decreases in strength, *i.e.*, becomes less stabilizing, along the series: NI_3, NBr_3, NCl_3, NF_3. Trends in ΔE curves originate solely from a more stabilizing interaction energy ΔE_{int}. Note that the strain energy ΔE_{strain} curves show a reversed trend, overruled by the trend in ΔE_{int}, namely, NF_3 has a less destabilizing ΔE_{strain} than NI_3. Therefore, similar to borane–ammonia, the relative stability of the $H_3B–NY_3$ Lewis pairs is determined by ΔE_{int}.

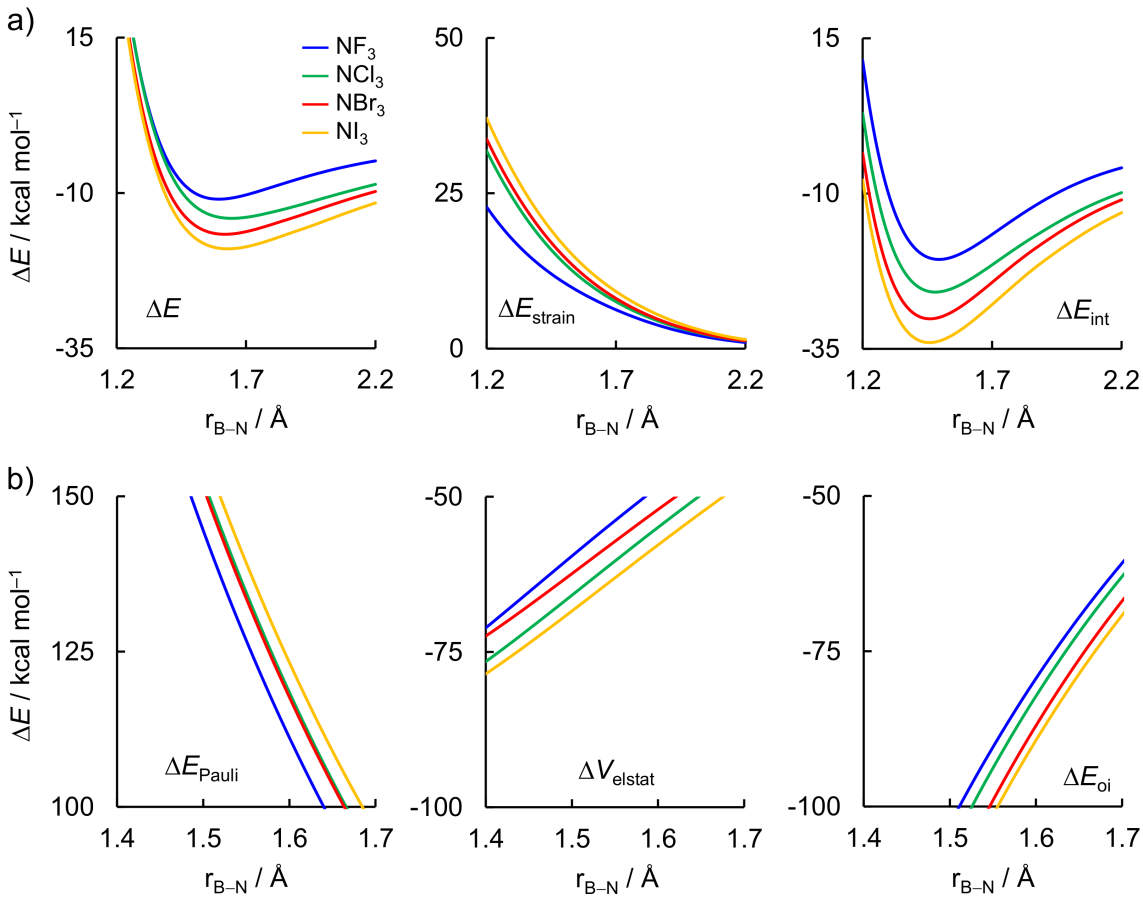

Figure 6.6: a) Activation strain model and b) energy decomposition analysis of the $H_3B–NY_3$ Lewis pairs projected onto the B–N bond distance (where Y = F, Cl, Br, and I) computed at ZORA-BLYP-D3(BJ)/TZ2P. Dispersion energy ΔE_{disp} not shown, see Table 6.4 for data at consistent geometries.

Table 6.4: Activation strain model and energy decomposition analysis terms (in kcal mol^{-1}) computed at consistent geometries with a forming B–N distance of 1.687 Å of the H_3B–NY_3 Lewis pairs (where Y = F, Cl, Br, and I).[a]

Lewis base	ΔE	ΔE_{strain}	ΔE_{int}	ΔV_{elstat}	ΔE_{Pauli}	ΔE_{oi}	ΔE_{disp}
NF_3	–10.5	6.5	–16.9	–39.6	88.2	–63.0	–2.5
NCl_3	–14.0	7.8	–21.8	–46.0	94.6	–65.2	–5.2
NBr_3	–16.3	8.4	–24.7	–43.6	94.2	–69.2	–6.1
NI_3	–18.8	9.6	–28.3	–48.9	99.4	–71.5	–7.3

[a] Computed at ZORA-BLYP-D3(BJ)/TZ2P.

The observed trend in ΔE_{int} curves is given by the orbital interaction ΔE_{oi} curves, that is most stabilizing for the Lewis complex with NI_3 and decreases in strength along the series NI_3, NBr_3, NCl_3, NF_3. From NI_3 to NF_3, at the consistent geometry (see Table 6.4), ΔE_{int} varies from a value of –28.3 to –16.9 kcal mol^{-1} and ΔE_{oi} varies from a value of –71.5 to –63.0 kcal mol^{-1}. This is paralleled by a decrease of Pauli repulsion, that varies from a value of 99.4 to 88.2 kcal mol^{-1} from NI_3 to NF_3, as reflected by the decreasing number of core electrons and diffuse orbitals as the halogen decreases in size. Trends in ΔV_{elstat}, on the other hand, are not exactly systematic along the Lewis bases. They are partially inverted and decreases in strength along the series NI_3, NCl_3, NBr_3, NF_3. Finally, the dispersion energy ΔE_{disp} has the smallest contribution to ΔE_{int} (not shown in Figure 6.6, see Table 6.4 for data at consistent geometries).

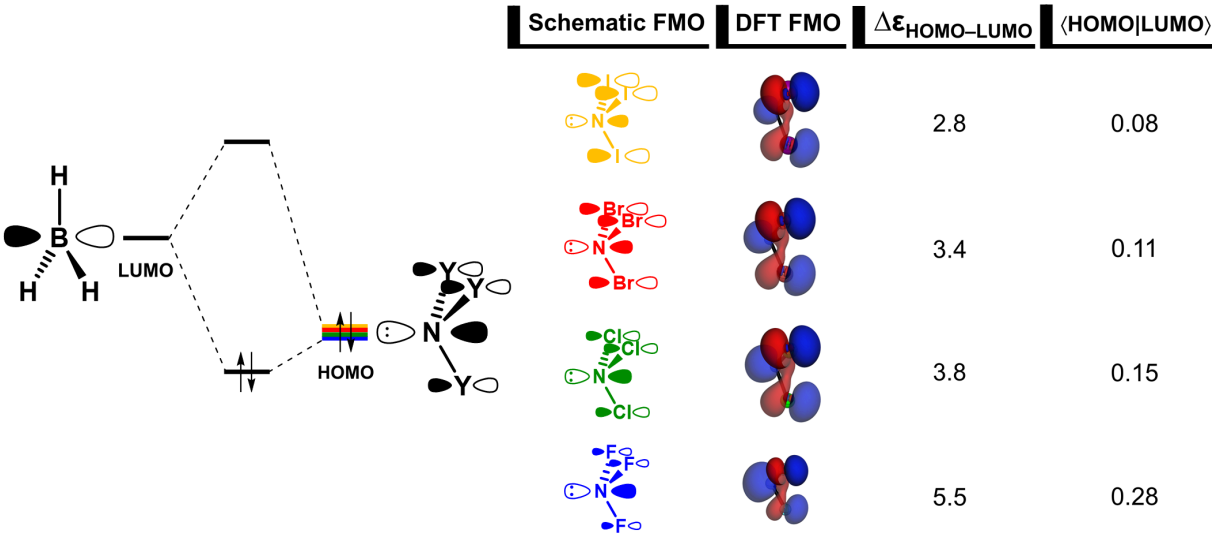

Figure 6.7: Schematic representation of the HOMO–LUMO orbital interaction in the H_3B–NY_3 Lewis pairs (where Y = F, Cl, Br, and I). Isosurface (at 0.03 au), energy gap (in eV) and orbital overlap of the interaction between HOMO and LUMO of the a_1 irreducible representation of the C_{3v} symmetry.

Formation of the $H_3B–NY_3$ Lewis pairs involves a key orbital interaction between the filled out-of-phase mixing of N $2p_z$ and halogens np_z orbitals of NY_3 with the empty B $2p_z$ orbital of BH_3, the HOMO(base)–LUMO(acid) interaction (see Figure 6.7; additional stabilizing contribution from the HOMO-2(base)–LUMO(acid) interaction is given in Appendix 6.5). However, this interaction is relatively less stabilizing compared to borane–ammonia. As the Y ligands vary from H to the increasingly more electronegative atoms I, Br, Cl, and F, the HOMO drops in energy, which leads to a larger HOMO–LUMO energy gap ($\Delta\varepsilon$ = 2.5, 2.8, 3.4, 3.8, and 5.5 eV along $NY_3 = NH_3$, NI_3, NBr_3, NCl_3, and NF_3, respectively). The corresponding orbital overlap ⟨HOMO|LUMO⟩, on the other hand, decreases on descending group 17, *i.e.*, it becomes less favorable. Because of the out-of-phase mixing of the np_z orbitals, the amplitude of HOMO is larger on the less electronegative atom (either N or Y). Thus, the amplitude on the nitrogen atom decreases along the series NF_3, NCl_3, NBr_3, and NI_3, which decreases the spatial overlap with the empty $2p_z$ orbital of BH_3. Therefore, the trend in $\Delta\varepsilon$ overrules the trend in ⟨HOMO|LUMO⟩, determining the trend in orbital interaction energies and, eventually, in the stability of the $H_3B–NY_3$ Lewis pairs.

6.4 Conclusion

At variance with the current view, the strength of archetypical $X_3B–NY_3$ Lewis pair bonds (where X,Y = H, F, Cl, Br, and I) is not solely attributed to the strength of the stabilizing frontier molecular orbital interactions. The bonding mechanism involving boron trihalides, for example, is determined by the amount of energy required to deform the fragments, especially the Lewis acid, upon complexation. This follows from our detailed bonding analyses based on relativistic dispersion-corrected density functional theory at ZORA-BLYP-D3(BJ)/TZ2P.

Our activation strain and quantitative Kohn-Sham MO analyses reveal that the bonding energy of the series $X_3B–NH_3$ is determined by the strain energy associated with the geometrical distortion of the Lewis acid on going from the planar to the pyramidal geometry acquired in the Lewis complex. We have, for the first time, quantitatively decomposed the strain energy of the Lewis acid in terms of the change in the interaction energy within one fragment upon its deformation. The decrease in the strain energy directly correlates with the weakening of the B–X bond as the electronegativity of X decreases along the series: F, Cl, Br, and I. Most of this effect arises from the bonding in the plane of the molecule, not in the π system as is widely believed. In other words, the less destabilizing energy required to deform a weak B–X

bond results in a smaller strain energy, which manifests in a more stable Lewis pair. This is the actual reason why the Lewis pairs becomes systematically stronger as BX_3 goes from BF_3 to BI_3, and not because of a more stabilizing interaction energy as is the currently accepted rationale. For the $H_3B–NY_3$ series, the bonding is driven by the charge-transfer stemming from the commonly accepted HOMO–LUMO interaction between the lone pair on the nitrogen of the Lewis base and the empty p orbital at the boron of the Lewis acid.

This work clearly demonstrates the role of the strain energy, besides the well-known donor-acceptor orbital and electrostatic interactions, in playing a leading role in determining the strength of Lewis acid/base interactions. Our findings are both chemically intuitive and grounded in quantum chemical findings based on state-of-the-art computations. Importantly, we have brought our understanding of these fundamental interactions into the 21st century and hope that this work will be useful for the development of novel Lewis pair chemistries.

6.5 References

[1] a) T. L. Brown, H. E. LeMay, B. E. Bursten, J. R. Burdge, *Chemistry: The Central Science*, Pearson Prentice Hall, **2005**; b) P. Atkins, L. Jones, L. Laverman, *Chemical Principles: The Quest for Insight*, W. H. Freeman and Company, New York, **2016**.

[2] a) G. N. Lewis, *Valence and the Structure of Atoms and Molecules*, The Chemical Catalog Company, New York, **1923**; b) G. N. Lewis, *J. Franklin Inst.* **1938**, *226*, 293.

[3] W. B. Jensen, *Chem. Rev.* **1978**, *78*, 1.

[4] See, for instance: a) P. Vermeeren, T. A. Hamlin, I. Fernández, F. M. Bickelhaupt, *Angew. Chem. Int. Ed.* **2020**, *59*, 6201; *Angew. Chem.* **2020**, *132*, 6260; b) P. H. Huy, *Eur. J. Org. Chem.* **2020**, *2020*, 10; c) T. A. Hamlin, I. Fernandez, F. M. Bickelhaupt, *Angew. Chem. Int. Ed.* **2019**, *58*, 8922; *Angew. Chem.* **2019**, *131*, 9015; d) Q. Shi, W. Wang, Y. Wang, Y. Lan, C. Yao, D. Wei, *Org. Chem. Front.* **2019**, *6*, 2692.

[5] For examples on the applicability of frustrated Lewis pair catalysts, see: a) J. Paradies, *Coord. Chem. Rev.* **2019**, *380*, 170; b) D. W. Stephan, *Science* **2016**, *354*, 1248; c) D. W. Stephan, *J. Am. Chem. Soc.* **2015**, *137*, 10018; d) D. W. Stephan, G. Erker, *Angew. Chem. Int. Ed.* **2015**, *54*, 6400; *Angew. Chem.* **2015**, *127*, 6498; e) C. Appelt, H. Westenberg, F. Bertini, A. W. Ehlers, J. C. Slootweg, K. Lammertsma, W. Uhl, *Angew. Chem. Int. Ed.* **2011**, *50*, 3925; *Angew. Chem.* **2011**, *123*, 4011; f) D. W. Stephan, G. Erker, *Angew. Chem. Int. Ed.* **2010**, *49*, 46; *Angew. Chem.* **2010**, *122*, 50; g) S. Grimme, H. Kruse, L. Goerigk, G. Erker, *Angew. Chem. Int. Ed.* **2010**, *49*, 1402; *Angew. Chem.* **2010**, *122*, 1444.

[6] a) M. Méndez, A. Cedillo, *Comput. Theor. Chem.* **2013**, *1011*, 44; b) H. Anane, S. El Houssame, A. El Guerraze, A. Guermoune, A. Boutalib, A. Jarid, I. Nebot-Gil, F. Tomás, *Cent. Eur. J. Chem.* **2008**, *6*, 400; c) H. Anane, S. El Houssame, A. El Guerraze, A. Jarid, A. Boutalib, I. Nebot-Gil, F. Tomás, *J. Mol. Struc. THEOCHEM* **2004**, *709*, 103; d) Y. Mo, L. Song, W. Wu, Q. Zhang, *J. Am. Chem. Soc.* **2004**, *126*, 3974; e) Y. Mo, J. Gao, *J. Phys. Chem. A* **2001**, *105*, 6530; f) H. Hirao, H. Fujimoto, *J. Phys. Chem. A* **2000**, *104*, 6649; g) S. Fau, G. Frenking, *Mol. Phys.* **1999**, *96*, 519; h) D. J. Hankinson, J. Almlöf, K. R. Leopold, *J. Phys. Chem.* **1996**, *100*, 6904; i) V. Jonas, G. Frenking, M. T. Reetz, *J. Am. Chem. Soc.* **1994**, *116*, 8141, and references cited therein; j) G. Frenking, K. Wichmann, N. Fröhlich, C. Loschen, M. Lein, J. Frunzke, V. M. Rayón, *Coord. Chem. Rev.* **2003**, *238–239*, 5.

[7] a) R. G. Pearson, *J. Chem. Educ.* **1968**, *45*, 643; b) R. G. Pearson, *Science* **1966**, *151*, 172; c) R. G. Pearson, *J. Am. Chem. Soc.* **1963**, *85*, 3533.

[8] a) T. Bettens, M. Alonso, F. De Proft, T. A. Hamlin, F. M. Bickelhaupt, *Chem. Eur. J.* **2020**, *26*, 3884; b) H. Mayr, M. Breugst, A. R. Ofial, *Angew. Chem. Int. Ed.* **2011**, *50*, 6470; *Angew. Chem.* **2011**, *123*, 6598; c) M. Breugst, H. Zipse, J. P. Guthrie, H. Mayr, *Angew. Chem. Int. Ed.* **2010**, *49*, 5165; *Angew. Chem.* **2010**, *122*, 5291.

[9] a) S. J. Grabowski, *J. Comput. Chem.* **2018**, *39*, 472; b) B. J. van der Veken, E. J. Sluyts, *J. Am. Chem. Soc.* **1997**, *119*, 11516; c) F. A. Cotton, G. Wilkinson, C. A. Murillo, M. Bochmann, *Advanced Inorganic Chemistry*, 6th ed., John Wiley and Sons, New York, **1999**.

[10] a) A. Skancke, P. N. Skancke, *J. Phys. Chem.* **1996**, *100*, 15079; b) V. Branchadell, A. Oliva, *J. Mol. Struct. THEOCHEM* **1991**, *236*, 75; c) J. F. Liebman, *Struct. Chem.* **1990**, *1*, 395.

[11] a) J. A. Plumley, J. D. Evanseck, *J. Phys. Chem. A* **2009**, *113*, 5985; b) F. Bessac, G. Frenking, *Inorg. Chem.* **2003**, *42*, 7990; c) H. Hirao, K. Omoto, H. Fujimoto, *J. Phys. Chem. A* **1999**, *103*, 5807; d) T. Brinck, J. S. Murray, P. Politzer, *Inorg. Chem.* **1993**, *32*, 2622.

[12] a) E. A. Robinson, G. L. Heard, R. J. Gillespie, *J. Mol. Struct.* **1999**, *485–486*, 305; b) B. D. Rowsell, R. J. Gillespie, G. L. Heard, *Inorg. Chem.* **1999**, *38*, 4659.

[13] a) A. R. Jupp, T. C. Johnstone, D. W. Stephan, *Inorg. Chem.* **2018**, *57*, 14764; b) S. Noorizadeh, E. Shakerzadeh, *J. Mol. Struct. THEOCHEM* **2008**, *868*, 22.

[14] G. Frenking, S. Fau, C. M. Marchand, H. Grützmacher, *J. Am. Chem. Soc.* **1997**, *119*, 6648.

[15] S. C. C. van der Lubbe, C. Fonseca Guerra, *Chem. Asian J.* **2019**, *14*, 2760.

[16] a) G. te Velde, F. M. Bickelhaupt, E. J. Baerends, C. Fonseca Guerra, S. J. A. van Gisbergen, J. G. Snijders, T. Ziegler, *J. Comput. Chem.* **2001**, *22*, 931; b) C. Fonseca Guerra, J. G. Snijders, G. te Velde, E. J. Baerends, *Theor. Chem. Acc.* **1998**, *99*, 391; c) ADF2017.103, SCM Theoretical Chemistry, Vrije Universiteit: Amsterdam (Netherlands).

[17] a) A. D. Becke, *Phys. Rev. A* **1988**, *38*, 3098; b) C. T. Lee, W. T. Yang, R. G. Parr, *Phys. Rev. B* **1988**, *37*, 785.

[18] a) S. Grimme, J. Antony, S. Ehrlich, H. Krieg, *J. Chem. Phys.* **2010**, *132*, 154104; b) S. Grimme, S. Ehrlich, L. Goerigk, *J. Comput. Chem.* **2011**, *32*, 1456.

[19] E. R. Johnson, A. D. Becke, *J. Chem. Phys.* **2005**, *123*, 024101.

[20] a) E. van Lenthe, R. van Leeuwen, E. J. Baerends, J. G. Snijders, *Int. J. Quantum Chem.* **1996**, *57*, 281; b) E. van Lenthe, E. J. Baerends, J. G. Snijders, *J. Chem. Phys.* **1994**, *101*, 9783.

[21] E. van Lenthe, E. J. Baerends, *J. Comput. Chem.* **2003**, *24*, 1142.

[22] M. Franchini, P. H. T. Philipsen, E. van Lenthe, L. Visscher, *J. Chem. Theory Comput.* **2014**, *10*, 1994.

[23] M. Franchini, P. H. T. Philipsen, L. Visscher, *J. Comput. Chem.* **2013**, *34*, 1819.

[24] a) A. Bérces, R. M. Dickson, L. Fan, H. Jacobsen, D. Swerhone, T. Ziegler, *Comput. Phys. Commun.* **1997**, *100*, 247; b) H. Jacobsen, A. Bérces, D. P. Swerhone, T. Ziegler, *Comput. Phys. Commun.* **1997**, *100*, 263; c) S. K. Wolff, *Int. J. Quantum Chem.* **2005**, *104*, 645.

[25] C. Y. Legault, CYLview 1.0b, Université de Sherbrooke: Sherbrooke, **2009**.

[26] a) P. Vermeeren, S. C. C. van der Lubbe, C. Fonseca Guerra, F. M. Bickelhaupt, T. A. Hamlin, *Nat. Protoc.* **2020**, *15*, 649; b) F. M. Bickelhaupt, K. N. Houk, *Angew. Chem. Int. Ed.* **2017**, *56*, 10070; *Angew. Chem.* **2017**, *129*, 10204; c) L. P. Wolters, F. M. Bickelhaupt, *WIRES Comput. Mol. Sci.* **2015**, *5*, 324; d) I. Fernández, F. M. Bickelhaupt, *Chem. Soc. Rev.* **2014**, *43*, 4953; e) W.-J. van Zeist, F. M. Bickelhaupt, *Org. Biomol. Chem.* **2010**, *8*, 3118; f) F. M. Bickelhaupt, *J. Comput. Chem.* **1999**, *20*, 114.

[27] a) R. van Meer, O. V. Gritsenko, E. J. Baerends, *J. Chem. Theory Comput.* **2014**, *10*, 4432; b) F. M. Bickelhaupt, E. J. Baerends, in *Reviews in Computational Chemistry*, ed. K. B. Lipkowitz, D. B. Boyd, Wiley, Hoboken, **2000**, pp. 1–86; c) L. Zhao, M. von Hopffgarten, D. M. Andrada, G. Frenking, *WIREs Comput. Mol. Sci.* **2018**, *8*, e1345.

[28] a) W.-J. van Zeist, C. Fonseca Guerra, F. M. Bickelhaupt, *J. Comp. Chem.* **2008**, *29*, 312; b) X. Sun, T. M. Soini, J. Poater, T. A. Hamlin, F. M. Bickelhaupt, *J. Comp. Chem.* **2019**, *40*, 2227.

[29] C. Fonseca Guerra, J.-W. Handgraaf, E. J. Baerends, F. M. Bickelhaupt, *J. Comput. Chem.* **2004**, *25*, 189.

[30] a) P. W. Atkins, J. de Pauli, *Physical Chemistry*, Edn. 9, Oxford University Press, Oxford, **2010**; b) F. Jensen, *Introduction to Computational Chemistry*, Edn. 2, Wiley, West Sussex, **2007**.

[31] L. R. Thorne, R. D. Suenram, F. J. Lovas, *J. Chem. Phys.* **1983**, *78*, 167.

[32] For a detailed discussion on the behavior of each EDA term along formation of a chemical bond, see: a) G. Frenking, F. M. Bickelhaupt, in *The Chemical Bond: Fundamental Aspects of Chemical*

Bonding, ed. G. Frenking, S. Shaik, Wiley-VCH, Weinheim, **2014**, 121-158; b) A. Krapp, F. M. Bickelhaupt, G. Frenking, *Chem. Eur. J.* **2006**, *12*, 9196.

[33] T. A. Albright, J. K. Burdett, W. H. Wangbo, *Orbital Interactions in Chemistry*, Wiley, New York, **2013**.

[34] V. Branchadell, A. Sbai, A. Oliva, *J. Phys. Chem.* **1995**, *99*, 6472.

[35] F. M. Bickelhaupt, T. Ziegler, P. von Ragué Schleyer, *Organometallics* **1996**, *15*, 1477.

[36] W.-J. van Zeist, R. Yi, F. M. Bickelhaupt, *Sci. China Chem.* **2010**, *53*, 210.

[37] (a) L. Pauling, *The Nature of the Chemical Bond*, Cornell University Press, Ithaca, NY, **1960**; (b) A. L. Allred, *J. Inorg. Nucl. Chem.* **1961**, *17*, 215.

[38] Y. R. Luo, *Comprehensive Handbook of Chemical Bond Energies*, CRC Press, Boca Raton, FL, **2007**.

6.6 Appendices

Appendix 6.1: Energies (in kcal mol^{-1}) of the $X_3B–NY_3$ Lewis pairs (where X,Y = H, F, Cl, Br, and I) in their equilibrium geometry relative to the separated Lewis acids and Lewis bases.[a]

$X_3B–NY_3$	$\Delta H_{298.15}$	ΔE	ΔE_{strain}	ΔE_{int}
$H_3B–NH_3$	–25.7	–29.5	12.5	–42.0
$F_3B–NH_3$	–16.1	–18.4	21.1	–39.5
$Cl_3B–NH_3$	–18.3	–21.2	21.7	–42.9
$Br_3B–NH_3$	–22.0	–25.0	19.7	–44.7
$I_3B–NH_3$	–23.2	–26.2	16.9	–43.2
$H_3B–NF_3$	–8.7	–11.0	8.3	–19.3
$H_3B–NCl_3$	–12.0	–14.1	8.9	–23.0
$H_3B–NBr_3$	–14.8	–16.7	10.4	–27.0
$H_3B–NI_3$	–17.2	–19.0	11.3	–30.4

[a] Computed at ZORA-BLYP-D3(BJ)/TZ2P.

Appendix 6.2: Energy decomposition analysis terms (in kcal mol^{-1}) computed at consistent geometries with a B–N distance of 1.687 Å of the $X_3B–NH_3$ Lewis pairs (where X = F, Cl, Br, and I).[a]

Lewis acid	ΔE_{int}	ΔV_{elstat}	ΔE_{Pauli}	ΔE_{oi}	ΔE_{disp}
BF_3	–40.6	–94.5	133.6	–77.1	–2.6
BCl_3	–41.3	–107.8	173.8	–102.1	–5.2
BBr_3	–42.6	–110.2	183.4	–109.7	–6.1
BI_3	–41.2	–114.9	197.6	–116.7	–7.2

[a] Computed at ZORA-BLYP-D3(BJ)/TZ2P.

Appendix 6.3: Energies (in kcal mol^{-1}), orbital energy gap (in eV) and orbital overlap of the analysis of the bonding mechanism in planar and pyramidal BX_3 (where X = F, Cl, Br, and I).[a]

	BF_3		**BCl_3**		**BBr_3**		**BI_3**	
	plan	pyr	plan	pyr	plan	pyr	plan	pyr
$\Delta E_{int,X–X–X}$	37.1	32.3	52.0	45.5	48.4	42.7	46.7	41.6
$\Delta E_{int,B–X_3}$	–640.1	–613.1	–475.3	–448.6	–420.6	–397.0	–367.2	–346.7
$\Delta V_{elstat,B–X_3}$	–494.0	–419.2	–454.3	–358.5	–450.7	–348.2	–415.4	–316.0
$\Delta E_{Pauli,B–X_3}$	922.6	780.2	635.9	509.9	570.7	448.7	495.9	383.8
$\Delta E_{oi,B–X_3}$	–1068.0	–973.3	–654.2	–597.3	–537.3	–494.2	–443.7	–410.4
$\Delta E_{oi,a_1}$	–305.3	–278.3	–180.8	–167.4	–147.7	–139.3	–126.8	–121.0
$\Delta E_{oi,e_1}$	–759.7	–692.6	–472.2	–429.2	–388.8	–354.5	–316.5	–289.2
$\Delta E_{oi,a_2}$	–2.9	–2.3	–1.1	–0.8	–0.7	–0.5	–0.4	–0.3
$\Delta E_{disp,B–X_3}$	–0.8	–0.8	–2.7	–2.7	–3.3	–3.3	–4.1	–4.1
$\langle 1a_1 \vert 2s \rangle$	0.41	0.39	0.53	0.49	0.56	0.52	0.57	0.52
$\langle 1e_1 \vert 2p_x \rangle$	0.34	0.32	0.40	0.36	0.40	0.36	0.40	0.36
$\langle 2a_1 \vert 2p_z \rangle$	0.45	0.38	0.47	0.37	0.46	0.36	0.44	0.34
$\vert \Delta\varepsilon_{1a_1–2s} \vert$	2.7	2.6	0.2	0.3	1.0	1.1	1.9	2.0
$\vert \Delta\varepsilon_{1e_1–2p_x} \vert$	8.1	8.0	5.1	5.0	4.3	4.2	3.4	3.3
$\vert \Delta\varepsilon_{2a_1–2p_z} \vert$	7.0	6.9	4.5	4.5	3.8	3.7	3.0	3.0

[a] Computed at ZORA-BLYP-D3(BJ)/TZ2P.

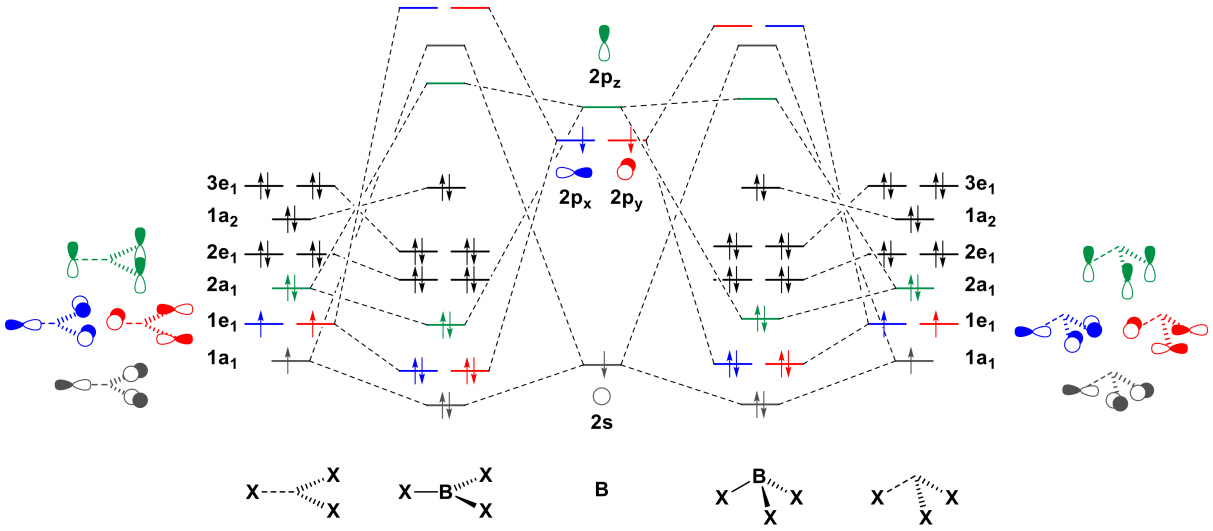

Appendix 6.4: Orbital interaction scheme for planar and pyramidal BX_3 (where X = F, Cl, Br, and I).

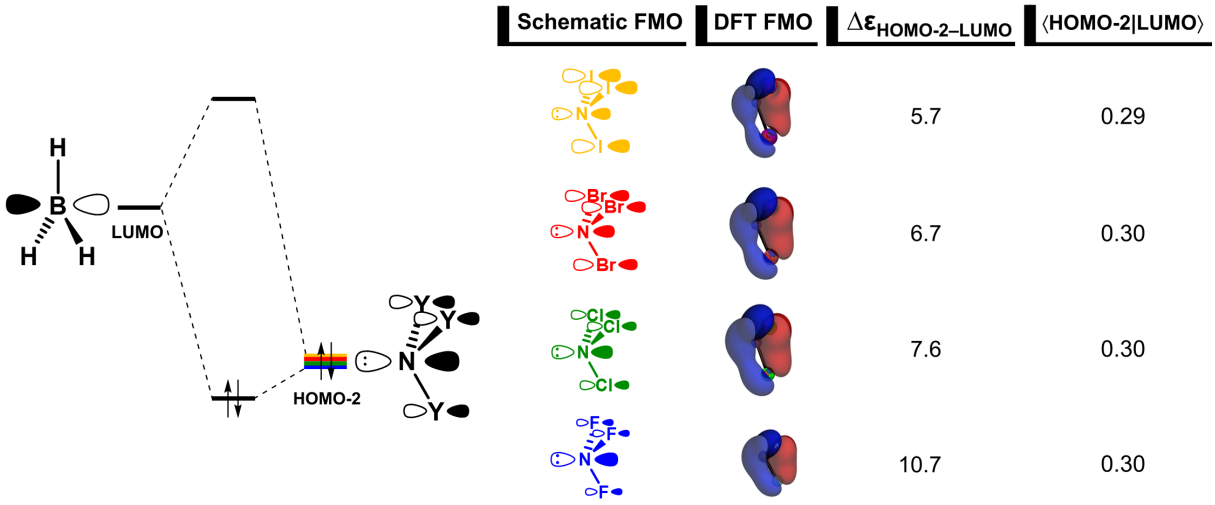

Appendix 6.5: Schematic representation of the HOMO-2(base)–LUMO(acid) orbital interaction in the H_3B–NY_3 Lewis pairs (where Y = F, Cl, Br, and I). Isosurface (at 0.03 au), energy gap (in eV) and orbital overlap of the interaction between HOMO-2 and LUMO of the a_1 irreducible representation of the C_{3v} symmetry.

7 SUMMARY

This thesis presents the results of density functional theory investigations on the structure and bonding of halogenated compounds. The main purpose of this work is to gain insights into archetypal model systems that can be used to unravel the physical forces underlying the bonding mechanism and conformational arrangement of (in)organic compounds. This summary highlights the main findings discussed in previous chapters.

In Chapter 3, we have explored whether rational modifications in the backbone of 2-halocyclohexanones would change their axial-equatorial conformational equilibrium. Our results revealed that an endocyclic nitrogen group, yielding the F–CH_2–CH_2–NR motif, known to induce the *gauche* effect in acyclic compounds, had little influence on the conformational preferences of the 2-fluorocyclohexanone. Similar behavior was observed for heavier 2-halocyclohexanones. We began by evaluating the large *N*-Boc group and then gradually reduced it to an amine group. In all cases, the short-range destabilizing interaction of the halogen atom with the carbonyl group was the dominant factor behind the observed conformational trends. Even with the removal of the carbonyl group, the energy difference between *gauche* and *anti*-conformers (axial and equatorial, respectively) was too small to observe an effective contribution from the hyperconjugative interactions featured in the *gauche* effect. Only groups that induced stronger electrostatic interactions, such as the ammonium group, could shift the preference to the axial conformer even in highly polar solvents. Additionally, we observed that our DFT computations nicely confirmed the conformational trends obtained from NMR experiments. These findings illustrate the remarkable complementarity of the theoretical-experimental approach in conformational analysis and provide important insights into the conformational design of alicyclic compounds.

To investigate the subtle conformational effects observed in 2-halocyclohexanones, we have carried out subsequent analyses on 1,2-disubstituted ethane fragments, namely 1,2-dihaloethanes (Chapter 4) and haloacetaldehydes (Chapter 5), to pinpoint the physical factors giving rise to the *gauche* effect and the nature of intramolecular interactions in α-halocarbonyl systems, respectively. We established a rigorous framework to analyze and interpret rotational

energy profiles that gives valuable insights into geometrical changes and the role of specific intramolecular interactions during internal rotation around the C–C bond.

Through comprehensive analyses of the rotational energy profiles of 1,2-dihaloethanes $XH_2C–CH_2X$ (where X = F, Cl, Br, and I) performed in Chapter 4 the causal role played by steric Pauli repulsion in the *gauche* effect was revealed: the small steric hindrance between compact fluorine atoms allows for subtle attractive hyperconjugative interactions to favor the *gauche* conformer for 1,2-difluoroethane. Stabilizing orbital interactions favored the *gauche* conformer for all 1,2-dihaloethanes, however, the increasing steric demand of the halogen atom on descending group 17 in the periodic table shifted the preference from *gauche* for X = F to *anti* for X = Cl to I, in a way to reduce the overlap between occupied orbitals. Hyperconjugation was more stabilizing for X = F because of a larger overlap between donor and acceptor orbitals, which contrasts with the current explanation based on the orbital energies alone. Therefore, the *gauche* effect observed in 1,2-difluoroethane arises from an interplay of small steric repulsion and more stabilizing hyperconjugation.

We also showed that to properly identify causalities between intramolecular interactions and conformational stability, it is crucial to take into consideration the effect of geometrical relaxation along conformational changes on the different energy components and associated physical factors. Analysis on final equilibrium geometries could lead to a misleading picture that obscures cause and effect. The insights obtained in this work provide a straightforward framework to investigate and interpret rotational energy profiles, which enabled us to uncover a set of unique causal relationships.

The same approach has been applied in Chapter 5 to assess the validity of the concept of dipolar repulsion to explain conformational preferences of α-halocarbonyl compounds. The idea that atoms behave as point charges and, therefore, electronegative atoms would electrostatically repel each other is widely employed to rationalize several phenomena in organic chemistry. However, our detailed analysis of the rotational energy profiles of haloacetaldehydes $OHC–CH_2X$ (where X = F, Cl, Br, and I) revealed that the *syn* conformer, the orientation where halogen and oxygen atoms are in closest proximity, is electrostatically favored for the iodoacetaldehyde because of the contribution from the attractive nuclear-electron component increases as the halogen increases in size. These results reinforce that atoms are characterized by a complex charge distribution of nuclei and electron charge density that quite often deviates from the ideal behavior of spherical point charges. The latter oversimplified

view was only valid for small and compact atoms, in our model systems, the second-row fluorine atom.

Yet, electrostatic interactions did not determine the overall trend in the energy profile for rotation around the C–C bond of haloacetaldehydes. Steric Pauli repulsion was the dominant factor giving rise to central rotational barriers, separating *syn* and *anti*-minima. While more stabilizing orbital interactions gradually shifted the global energy minimum from *anti* to *anticlinal* as X goes from F to I. Only for X = F did electrostatic interactions contribute to further stabilize and ultimately drive the preference to *anti*.

In Chapter 6, we showed that the stability of Lewis acid/base pairs also depends on the rigidity of the molecules to deform upon complexation. Our analyses on the formation of the $X_3B–NY_3$ Lewis pairs (where X, Y = H, F, Cl, Br, and I) showed an increase in the B–N bond strength as X and Y are varied along F, Cl, Br, I, and H. For $X_3B–NH_3$, the bonding mechanism was determined by the amount of energy required to deform the boron trihalides from their planar equilibrium geometry to the pyramidal geometry acquired in the Lewis complex. That is, the Lewis acid that more easily pyramidalizes can form a stronger bond with the Lewis base. Based on detailed analyses of the electronic structure of BX_3, we demonstrated that the decrease in strain energy from BF_3 to BI_3 directly correlates with the weakening of the B–X bond strength, which arises from the bonding in the plane of the molecule not in the π system as currently believed. For $H_3B–NY_3$, on the other hand, the bonding trends were driven by the widely accepted mechanism of HOMO(base)–LUMO(acid) interaction. As the hydrogen atoms of ammonia are replaced by increasingly electronegative halogens, the HOMO drops in energy, resulting in less stabilizing orbital interaction between the lone pair on the nitrogen atom of the Lewis base with the empty p orbital at the boron atom of the Lewis acid.

The introduction of halogen atoms can impart unique steric and electronic properties in a molecule, which can then be applied to rationally tune desirable molecular properties. We hope that the important findings described in this thesis contribute to an in-depth understanding of subtle conformational effects and bonding mechanism in halogenated systems, which are essential to more efficiently design new chemistries and to the further development of chemical sciences.

8 ACKNOWLEDGMENTS

The development of this PhD thesis was made possible due to the direct or indirect support of many wonderful people. Herein, I will do my best to express my gratitude to all of them. First of all, I am deeply grateful to my supervisors, Célia and Matheus, for believing in me and giving me the freedom and all the resources to work on my projects in the best way possible. Thank you for always being available to provide me with valuable insights, feedback, and advice. Matheus, your Organic Chemistry classes inspired me, and many other students I am sure, to pursue and find my way to the doctorate. Célia, you kindly welcomed me to Amsterdam and provided amazing opportunities for me to grow as a researcher ever since. I hope we can continue collaborating in the many years to come. I would like to also thank my co-supervisor, Trevor, for the daily supervision and for all the support and opportunities to improve my academic skills.

I am thankful to the Molecc group (aka 'Era do Gelo') and the DQI of UFLA for the warm and friendly working environment, you have been part of nearly all my academic life so far. Elaine and Teo for all the valuable lessons. Francisco and Joyce, my academic siblings, for their friendship along the way. And all my colleagues, especially, Adriana, Alexandre, Ander, Bruna, Camila, Daiana, Daniel, Fabiana, Fátima, Francisco, Giovanna, Ingrid, Ingrid, Jéssika, João, Josué, Joyce, Juliana, Laize, Letícia, Letícia, Lívia, Maíra, Mariana, Mariene, Marcus, Mateus, Stephen, Taináh, Tamiris, Telles, and Thaís, for their support, and all the fun times and coffee breaks, I already miss our daily office routine. A special thanks to Adelir, whose efforts made my travel to Amsterdam possible.

I am also grateful to the TheoCheM group for the inspiring, friendly, and highly skilled working environment. To Matthias for the insightful meetings and work discussions, each one of them was a unique opportunity to learn from your vast knowledge of chemistry and physics. I am looking forward to starting the projects we have planned and everything I will learn from them. A special thanks to room P-128, in chronological order: Eva, Tanja, Enrico, Maxime, and Marco, for all the work discussions and fun times in the office (including our multicultural board); to the museum & its consequences group for making me feel home in a strange country;

and to all TC group and SCM, especially to Arno, Ayush, Bas, Bryan, Celine, Chandan, Enrico, Eva, Eveline, Hans, Janani, Jelena, Johann, Marco, Nicolai, Pascal, Saad, Song, Souloke, Stan, Stephanie, Stephanie, Tanja, Thomas, and Xiaobo, for their kind support, lunch times and coffee breaks, and all the good memories.

I also want to express my deepest gratitude to my family, especially my parents, Luiz and Maria de Lourdes, and my sisters, Ana Luisa and Natália, for all their love and support along the way. A special thanks to Lucas for always being by my side and encouraging me to believe in myself; to Leila, Mariana, and Paulo for making me feel part of their family; and to all my friends, especially to Carolina, Ingrid, Joyce, Laene, Letícia, Leydiane, Stephanie, Suellen, and Vinícius, for the wonderful memories and for being part of my life, even most of the time from long distances.

9 LIST OF PUBLICATIONS

21. *Organic iodine induces unexpected conformational effects in 1-fluoro-2-iodoethane and 2-iodoethanol*
F. A. Martins, L. de Azevedo Santos, D. Rodrigues Silva, F. M. Bickelhaupt, C. Fonseca Guerra, M. P. Freitas
Manuscript in preparation

20. *Boron Tunneling in the "Weak" Bond-Stretch Isomerization of N–B Lewis Adducts*
A. Nandi, N. Tarannam, D. Rodrigues Silva, C. Fonseca Guerra, T. A. Hamlin, S. Kozuch
ChemPhysChem **2021**, *22*, 1857–1862
DOI: 10.1002/cphc.202100505

19. *Dipolar Repulsion in α-Halocarbonyl Compounds Revisited*
D. Rodrigues Silva, L. de Azevedo Santos, T. A. Hamlin, F. M. Bickelhaupt, M. P. Freitas, C. Fonseca Guerra
Phys. Chem. Chem. Phys. **2021**, *23*, 20883–20891 (Hot Paper)
DOI: 10.1039/D1CP02502C

18. *The Gauche Effect in XCH_2CH_2X Revisited*
D. Rodrigues Silva, L. de Azevedo Santos, T. A. Hamlin, C. Fonseca Guerra, M. P. Freitas, F. M. Bickelhaupt
ChemPhysChem **2021**, *22*, 641–648
DOI: 10.1002/cphc.202100090

17. *Nature and Strength of Lewis Acid/Base Interaction in Boron and Nitrogen Trihalides*
D. Rodrigues Silva, L. de Azevedo Santos, M. P. Freitas, C. Fonseca Guerra, T. A. Hamlin
Chem Asian J. **2020**, *15*, 4043–4054 (Very Important Paper and Front Cover)
DOI: 10.1002/asia.202001127

16. *S_N2 versus E2 Competition of F^- and PH_2^- Revisited*
P. Vermeeren, T. Hansen, M. Grasser, D. Rodrigues Silva, T. A. Hamlin, F. M. Bickelhaupt
J. Org. Chem. **2020**, *85*, 14087−14093
DOI: 10.1021/acs.joc.0c02112

15. *Conformational fingerprints in the modelling performance of MIA-QSAR: a case for SARS-CoV protease inhibitors*
J. K. Daré, D. Rodrigues Silva, T. C. Ramalho, M. P. Freitas
Molecular Simulation **2020**, *46*, 1055–1061
DOI: 10.1080/08927022.2020.1800691

14. *Conformational preferences of fluorine-containing agrochemicals and their implications for lipophilicity prediction*
D. Rodrigues Silva, J. K. Daré, M. P. Freitas
Beilstein J. Org. Chem. **2020**, *16*, 2469–2476
DOI: 10.3762/bjoc.16.200

13. *Evaluation of the Alicyclic Gauche Effect in 2-Fluorocyclohexanone Analogs: A Combined NMR and DFT Study*
D. Rodrigues Silva, L. A. Zeoly, R. A. Cormanich, C. Fonseca Guerra, M. P. Freitas
Eur. J. Org. Chem. **2020**, *2020*, 884–890
DOI: 10.1002/ejoc.201901815

12. *Asymmetric biodegradation of the nerve agents Sarin and VX by human dUTPase: chemometrics, molecular docking and hybrid QM/MM calculations*
A. A. de Castro, F. V. Soares, A. F. Pereira, T. C. Silva, D. Rodrigues Silva, D. T. Mancini, M. S. Caetano, E. F. F. da Cunha, T. C. Ramalho
J. Biomol. Struct. Dyn. **2019**, *37*, 2154–2164
DOI: 10.1080/07391102.2018.1478751

11. *Molecular Modelling of Potential Candidates for the Treatment of Depression*
D. Rodrigues Silva, S. J. Barigye, L. Santos-Garcia, E. F. F. da Cunha
Molecular Informatics **2019**, *38*, 1900024
DOI: 10.1002/minf.201900024

10. *The Role of Intramolecular Interactions on the Bioactive Conformation of Epinephrine*
D. Rodrigues Silva, J. M. Silla, L. de Azevedo Santos, E. F. F. da Cunha, M. P. Freitas
Molecular Informatics **2019**, *38*, 1800167
DOI: 10.1002/minf.201800167

9. *Design of novel N-myristoyltransferase inhibitors of leishmania donovani using four-dimensional quantitative structure-activity relationship analysis*
L. Santos-Garcia, D. Rodrigues Silva, L. C. Assis, T. M. de Assis, G. C. Gajo, I. A. Fernandes, T. C. Ramalho, E. F. F. da Cunha
J. Braz. Chem. Soc. **2018**, *29*, 1440–1454 (Cover)
DOI: 10.21577/0103-5053.20180007

8. *Insights into the pharmaceuticals and mechanisms of neurological orphan diseases: Current Status and future expectations*
T. C. Ramalho, A. A. de Castro, T. S. Tavares, M. C. Silva, D. Rodrigues Silva, P. H. Cesar, L. de Azevedo Santos, E. F. F. da Cunha, E. Nepovimova, K. Kuca
Progress in Neurobiology **2018**, *169*, 135–157
DOI: 10.1016/j.pneurobio.2018.06.011

7. *Multi-objective Optimization of Benzamide Derivatives as Rho Kinase Inhibitors*
G. C. Gajo, D. Rodrigues Silva, S. J. Barigye, E. F. F. da Cunha
Molecular Informatics **2018**, *37*, 1700080
DOI: 10.1002/minf.201700080

6. *Theoretical Study on the Conformational Bioeffect of the Fluorination of Acetylcholine*
J. M. Silla, D. Rodrigues Silva, M. P. Freitas
Molecular Informatics **2017**, *36*, 1700084
DOI: 10.1002/minf.201700084

5. *Computational Enzymology and Organophosphorus Degrading Enzymes: Promising Approaches Toward Remediation Technologies of Warfare Agents and Pesticides*
T. C. Ramalho, A. A. de Castro, D. Rodrigues Silva, M. C. Silva, T. C. C. Franca, B. J. Bennion, K. Kuca
Curr. Med. Chem. **2016**, *23*, 1041–1061
DOI: 10.2174/0929867323666160222113504

4. *QSAR analysis of nicotinamidic compounds and design of potential Bruton's tyrosine kinase (Btk) inhibitors*
L. Santos-Garcia, L. C. Assis, D. Rodrigues Silva, T. C. Ramalho, E. F. F. da Cunha
J. Biomol. Struct. Dyn. **2016**, *34*, 1421-1440
DOI: 10.1080/07391102.2015.1070750

3. *QSAR Models Guided by Molecular Dynamics Applied to Human Glucokinase Activators*
T. M. de Assis, G. C. Gajo, L. C. Assis, L. Santos-Garcia, D. Rodrigues Silva, T. C. Ramalho, E. F. F. da Cunha
Chem. Biol. Drug. Des. **2016**, *87*, 455-466
DOI: 10.1111/cbdd.12683

2. *Structure-based drugs design studies on spleen tyrosine kinase inhibitors*
L. C. Assis, L. Santos-Garcia, D. T. Mancini, T. M. de Assis, D. Rodrigues Silva, G. C. Gajo, A. A. de Castro, T. C. Ramalho, E. F. F. da Cunha
Letters in Drug Design & Discovery **2016**, *13*, 845–858
DOI: 10.2174/1570180813666160725095118

1. *4D-QSAR Model for Compounds with Binding Affinity Towards Dopamine D_2 Receptors*
D. Rodrigues Silva, T. C. Ramalho, E. F. F. da Cunha
Letters in Drug Design & Discovery **2014**, *11*, 649–664
DOI: 10.2174/15701808106661311132134448


CHEMISTRY
AN ASIAN JOURNAL
www.chemasianj.org
B
N
H
I
Br
Cl
F
H
I
Br
Cl
F
15/23
2020
A Journal of
ACES
Asian Chemical Editorial Society
Front Cover:
Nature and Strength of Lewis Acid/Base Interactions in Boron and Nitrogen Trihalides
WILEY-VCH